Registration No.
22601

-Technical Report-

Final Report: Theory of a spintronic nano-scale microwave diode for applications in microwave energy harvesting

by

Prof. Andrei Slavin, Oakland Univ.

COR's: Elena Bankowski, Thomas Meitzler

U.S. Army Tank Automotive Research, Development, and Engineering Center
Detroit Arsenal
Warren, Michigan 48397-5000

Report Documentation Page

Form Approved
OMB No. 0704-0188

1. REPORT DATE	2. REPORT TYPE	3. DATES COVERED
23 FEB 2012	**Technical Report**	**01-10-2010 to 28-02-2012**

4. TITLE AND SUBTITLE
THEORY OF A SPINTRONIC NANO-SCALE MICROWAVE DIODE FOR APPLICATIONS IN MICROWAVE ENERGY HARVESTING

5a. CONTRACT NUMBER
w56hzv-11-p-a565

5b. GRANT NUMBER

5c. PROGRAM ELEMENT NUMBER

6. AUTHOR(S)
Andrei Slavin; Thomas Meitzler; Elena Bankowski

5d. PROJECT NUMBER

5e. TASK NUMBER

5f. WORK UNIT NUMBER

7. PERFORMING ORGANIZATION NAME(S) AND ADDRESS(ES)
Oakland University,Department of Physics,Andrei Slavin,Rochester ,MI,48309

8. PERFORMING ORGANIZATION REPORT NUMBER
; #22601

9. SPONSORING/MONITORING AGENCY NAME(S) AND ADDRESS(ES)
U.S. Army TARDEC, 6501 E.11 Mile Rd, Warren, MI, 48397-5000

10. SPONSOR/MONITOR'S ACRONYM(S)
TARDEC

11. SPONSOR/MONITOR'S REPORT NUMBER(S)
#22601

12. DISTRIBUTION/AVAILABILITY STATEMENT
Approved for public release; distribution unlimited

13. SUPPLEMENTARY NOTES
Final Report on the ILIR-PILOT project "Theory of a spintronic nano-scale microwave diode for applications in the microwave detection and microwave energy harvesting."

14. ABSTRACT
N/A

15. SUBJECT TERMS

16. SECURITY CLASSIFICATION OF:			17. LIMITATION OF ABSTRACT	18. NUMBER OF PAGES	19a. NAME OF RESPONSIBLE PERSON
a. REPORT	b. ABSTRACT	c. THIS PAGE			
unclassified	**unclassified**	**unclassified**	**Same as Report (SAR)**	**80**	

“Applications of spintronic diodes for microwave detection and microwave energy harvesting”

Chapter 1.
Identification and selection rules of the spin-wave eigen-modes in a normally magnetized nano-pillar

We report on a spectroscopic study of the spin-wave eigen-modes inside an individual normally magnetized two layers circular nano-pillar (Permalloy|Copper|Permalloy) by means of a Magnetic Resonance Force Microscope (MRFM). We demonstrate that the observed spin-wave spectrum critically depends on the method of excitation. While the spatially uniform radio-frequency (RF) magnetic field excites only the axially symmetric modes having azimuthal index $\ell = 0$, the RF current flowing through the nano-pillar, creating a circular RF Oersted field, excites only the modes having azimuthal index $\ell = +1$. Breaking the axial symmetry of the nano-pillar, either by tilting the bias magnetic field or by making the pillar shape elliptical, mixes different ℓ-index symmetries, which can be excited simultaneously by the RF current. Experimental spectra are compared to theoretical prediction using both analytical and numerical calculations. An analysis of the influence of the static and dynamic dipolar coupling between the nano-pillar magnetic layers on the mode spectrum is performed.

I. INTRODUCTION

Technological progress in the fabrication of hybrid nanostructures using magnetic metals has allowed the emergence of a new science aimed at utilizing spin dependent effects in the electronic transport properties [1]. An elementary device of spintronics consists of two magnetic layers separated by a normal layer. It exhibits the well-known giant magneto-resistance (GMR) effect [2, 3], that is, its resistance depends on the relative angle between the magnetic layers. Nowadays, this useful property is extensively used in magnetic sensors [4, 5]. The converse effect is that a direct current can transfer spin angular momentum between two magnetic layers separated by either a normal metal or a thin insulating layer [6, 7]. As a result, a spin polarized current leads to a very efficient destabilization of the orientation of a magnetic moment [8]. Practical applications are the possibility to control the digital information in magnetic random access memories (MRAMs) [9, 10] or to produce high frequency signals in spin transfer nano-oscillators (STNOs) [11, 12].

From an experimental point of view, the precise identification of the spin-wave (SW)

eigen-modes in hybrid magnetic nanostructures remains to be done [13–18]. Of particular interest is the exact nature of the modes excited by a current perpendicular-to-plane in STNOs. Here, the identification of the associated symmetry behind each mode is essential. It gives a fundamental insight about their selection rules and about the mutual coupling mechanisms that might exist intra or inter STNOs. It also determines the optimum strategy to couple to the auto-oscillating mode observed when the spin transfer torque compensates the damping, a vital knowledge to achieve phase synchronization in arrays of nano-pillars [19]. These SW modes also have a fundamental influence on the high frequency properties of these devices and in particular on the noise of magneto-resistive sensors [20, 21].

A natural mean to probe SW modes in hybrid nanostructures is to use their magneto-resistance properties. For instance, thermal SW can be directly detected in the noise spectrum of tunneling magneto-resistance (TMR) devices owing to their large TMR ratio [22, 23]. It is also possible to use spin torque driven ferromagnetic resonance (ST-FMR) [24–30]. In this approach, an RF current flowing through the magneto-resistive device is used to excite the precession of magnetization and to detect it through a rectification effect. Direct excitation of SW modes by the RF field generated by micro-antennas and their detection through dc rectification [31] or high-frequency GMR measurements [32] has also been reported in spin-valve sensors. In all these experiments, the static magnetizations in the spin-valve have to be misaligned in order for the magnetization precession to produce a finite voltage. Because highly symmetric magnetization trajectories do not produce any variation of resistance with time in some cases, a third magnetic layer playing the role of an analyzer can be introduced [33]. In ST-FMR, the non-collinearity of the magnetizations is also required for the RF spin transfer excitation not to vanish [25, 26]. Moreover, the latter was never directly compared to standard FMR, where a uniform RF magnetic field is used to excite SW modes. Thus, although the voltage detection of SW eigen-modes in hybrid nanostructures is elegant, one should keep in mind that some of them might be hidden due to symmetry reasons.

Here, we propose an independent method of detecting the magnetic resonance inside a spin-valve nanostructure. We shall use a Magnetic Resonance Force Microscope (MRFM) [34–38]. A first decisive advantage of the MRFM technique is that the detection scheme does not rely on the SW spatial symmetry because it measures the change in the longitudinal component of the magnetization. Like a bolometric detection, mechanical based FMR

detects *all* the excited SW modes, independently of their phase [39, 40]. A second decisive advantage is that MRFM is a very sensitive technique that can measure the magnetization dynamics in nanostructures buried under metallic electrodes [41–43]. Indeed, the probe is a magnetic particle attached at the end of a soft cantilever and is coupled to the sample through the dipolar interaction.

In our roadmap to characterize the nature of the auto-oscillation modes in STNOs, we report in this chapter on a comprehensive identification of the SW eigen-modes in the simplest possible geometry: the normally magnetized circular spin-valve nano-pillar. This configuration is obtained by saturating the device with a large external magnetic field oriented perpendicular to the layers. Thanks to the preserved axial symmetry, a simplified spectroscopic signature of the different SW eigen-modes is expected. This identification is achieved experimentally from a comparative spectroscopic study of the SW eigen-modes excited either by an RF current flowing perpendicularly through the nano-pillar, as used in ST-FMR, or by a homogeneous RF in-plane magnetic field, as used in conventional FMR. It shall be developed as follows. In section II, we present the MRFM setup and the experimental protocol used to perform SW spectroscopy in a spin-valve. We show that the SW spectrum excited by a homogeneous RF magnetic field is distinct from the SW spectrum excited by an RF current flowing through the nano-pillar. In section III, we perform unambiguous assignment of the resonance peaks to the different layers by experimental means. We determine which layer contributes mostly to the observed resonant signals by adding a direct current through the nano-pillar, that produces opposite spin transfer torques on each magnetic layer. In section IV, we analyze the spectra by theoretical means using both a two-dimensional analytical formalism and a three-dimensional micromagnetic simulation package, SpinFlow 3D. By careful comparison of the measured spectra to the calculations, the nature of the SW dynamics in the system is identified and the selection rules for SW spectroscopy in perpendicularly magnetized spin-valve nanostructures are established. This result is completed in section V by a study of the influence of symmetry breaking on the selection rules. This is obtained experimentally by introducing a tilt angle of the applied magnetic field, and in simulations by changing the shape of the nano-pillar. In the conclusion, we emphasize the importance of this work for phase synchronization of STNOs. The chapter is arranged in such a fashion so as to present the main results in the body of the text. A comprehensive appendix has been put at the end of the chapter, where the details of the introduced material

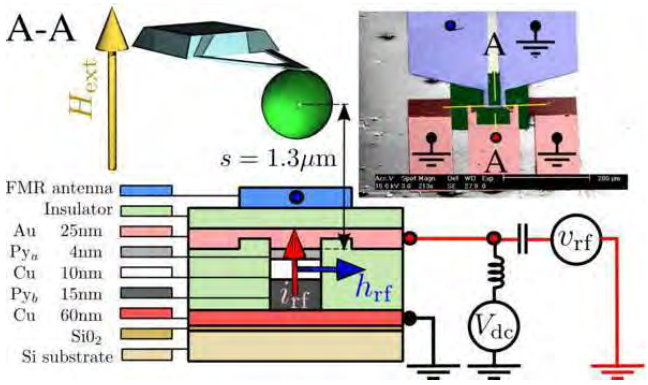

FIG. 1. Schematic representation of the experimental setup used for this comparative spin-wave spectroscopic study. The magnetic sample is a circular nano-pillar comprising a thin Py_a and a thick Py_b magnetic layers separated by a Cu spacer. It is saturated by a large magnetic field $\boldsymbol{H}_{\text{ext}}$ applied along its normal axis. A cantilever with a magnetic sphere attached at its tip monitors the magnetization dynamics inside the buried structure. The inset is a microscopy image (top view) of the two independent excitation circuits: in red the circuit allowing the injection of an RF current perpendicular-to-plane through the nano-pillar (i_{rf}, red arrow); in blue the circuit allowing the generation of an RF in-plane magnetic field (h_{rf}, blue arrow). The nano-pillar is at the center of the yellow cross-hair. The main figure is a section along the $A-A$ direction.

are developed.

II. FERROMAGNETIC RESONANCE FORCE SPECTROSCOPY

This section starts with a description of the nano-pillar sample, followed by a description of the MRFM instrument used for this spectroscopic study. Then, we compare the experimental SW spectra excited by an RF current flowing perpendicularly through the nano-pillar, as used in ST-FMR, and by a uniform RF magnetic field applied parallel to the layers, as used in standard FMR.

A. The lithographically patterned nanostructure

The spin-valve structure used in this study is a standard Permalloy ($Ni_{80}Fe_{20}$=Py) bi-layer structure sandwiching a 10 nm copper (Cu) spacer: the thicknesses of the thin Py_a and the thick Py_b layers are respectively t_a = 4 nm and t_b = 15 nm. Special care has been

put in the design of the microwave circuit around the nano-pillar. The inset of FIG. 1 shows a scanning electron microscopy top view of this circuit. The nano-pillar is located at the center of the cross-hair, in the middle of a highly symmetric pattern designed to minimize cross-talk effects between both RF circuits shown in blue and red, which provide two independent excitation means.

The nano-pillar is patterned by standard e-beam lithography and ion-milling techniques from the extended film, (Cu60 | Py_b15 | Cu10 | Py_a4 | Au25) with thicknesses expressed in nm, to a nano-pillar of nominal radius 100 nm. A precise control allows to stop the etching process exactly at the bottom Cu layer, which is subsequently used as the bottom contact electrode. A planarization process of a polymerized resist by reactive ion etching enables to uncover the top of the nano-pillar and to establish the top contact electrode. The top and bottom contact electrodes are shown in red tone in FIG. 1. These pads are impedance matched to allow for high frequency characterization by injecting an RF current i_{rf} through the device. The bottom Cu electrode is grounded and the top Au electrode is wire bounded to the central pin of a microwave cable. Hereafter, spectra associated to SW excitations by this part of the microwave circuit will be displayed in red tone. The nano-pillar is also connected through a bias-T to a dc current source and to a voltmeter through the same contact electrodes, which can be used for standard current perpendicular to the plane (CPP-GMR) transport measurements [44]. In our circuit, a positive current corresponds to a flow of electrons from the Py_b thick layer to the Py_a thin layer and stabilizes the parallel configuration due to the spin transfer effect [6, 7]. The studies presented below will be limited to a dc current up to the threshold current for auto-oscillations in the thin layer.

The originality of our design is the addition of an independent top microwave antenna, whose purpose is to produce an in-plane RF magnetic field h_{rf} at the nano-pillar location. In FIG. 1 this part of the microwave circuit is shown in blue tone. The broadband stripline antenna consists of a 300 nm thick Au layer evaporated on top of a polymer layer that provides electrical isolation from the rest of the structure. The width of the antenna constriction situated above the nano-pillar is 10 μm. Injecting a microwave current from a synthesizer inside the top antenna produces a homogeneous in-plane linearly polarized microwave magnetic field, oriented perpendicular to the stripe direction. Hereafter, spectra associated to SW excitations by this part of the microwave circuit will be displayed in blue

tone.

B. Mechanical-FMR

The nano-fabricated sample is then mounted inside a Magnetic Resonance Force Microscope (MRFM), hereafter named mechanical-FMR [38]. The whole apparatus is placed inside a vacuum chamber (10^{-6} mbar) operated at room temperature. The external magnetic field produced by an electromagnet is oriented out-of-plane, *i.e.*, along the nano-pillar axis $\hat{\boldsymbol{z}}$. The mechanical-FMR setup allows for a precise control, within 0.2°, of the polar angle between the applied field and $\hat{\boldsymbol{z}}$. In our study, the strength of the applied magnetic field shall exceed the saturation field ($\approx$ 8 kOe), so that the nano-pillar is studied in the saturated regime.

The mechanical detector is an ultra-soft cantilever, an Olympus Bio-Lever having a spring constant $k \approx 5$ mN/m, with a 800 nm diameter sphere of soft amorphous Fe (with 3% Si) glued to its apex. Standard piezo displacement techniques allow for positioning the magnetic spherical probe precisely above the center of the nano-pillar, so as to retain the axial symmetry. This is obtained when the dipolar interaction between the sample and the probe is maximal, by minimizing the cantilever resonance frequency, which is continuously monitored [41].

The mechanical sensor is insensitive to the rapid oscillations of the transverse component in the sample, which occur at the Larmor precession frequency, *i.e.*, several orders of magnitude faster than its mechanical resonances. The dipolar force on the cantilever probe is thus proportional to the static component of the magnetization inside the sample. For our normally magnetized sample, this longitudinal component reduces to M_z. We emphasize that for a bi-layer system, the force signal integrates the contribution of both layers. Moreover, the local $M_z(\boldsymbol{r})$ in the two magnetic layers is weighted by the distance dependence of the dipolar coupling to the center of the sphere. In our case though, where the separation between the sphere and the sample is much larger than the sample dimensions, one can neglect this weighting and the measured quantity simplifies to the spatial average:

$$\langle M_z \rangle \equiv \frac{1}{V} \int_V M_z(\boldsymbol{r}) d^3\boldsymbol{r} \,, \tag{1}$$

where the chevron brackets stand for the spatial average over the volume of the magnetic

body.

The mechanical-FMR spectroscopy presented below consists in recording by optical means the vibration amplitude of the cantilever either as a function of the out-of-plane magnetic field H_{ext} at a fixed microwave excitation frequency f_{fix}, or as a function of the excitation frequency f at a fixed magnetic field H_{fix}. This type of spectroscopy is called cw, for continuous wave, as it is monitoring the magnetization dynamics in the sample under a forced regime. A source modulation is applied on the cw excitation. It consists in a cyclic absorption sequence, where the microwave power is switched on and off at the cantilever resonance frequency, $f_c \approx 11.85$ kHz. The signal is thus proportional to $\langle \Delta M_z \rangle$, where Δ represents the difference from the thermal equilibrium state. The source modulation enhances the signal, recorded by a lock-in detection, by the quality factor $Q \approx 2000$ of the mechanical oscillator. The force sensitivity of our mechanical-FMR setup is better than 1 fN, corresponding to less than 10^3 Bohr magnetons in a bandwidth of one second [38]. We note that this modulation technique does not affect the line shape in the linear regime, because the period of modulation $1/f_c$ is very large compared to the relaxation times of the studied ferromagnetic system [45, 46]. Moreover, we emphasize that since the mechanical-FMR signal originates from the cyclic diminution of the spatially averaged magnetization inside the whole nano-pillar synchronous with the absorption of the microwave power, it detects all possible SW modes without discrimination [39, 40].

Finally, we mention that the stray field produced by the magnetic sphere attached on the cantilever does affect the detected SW spectra. In our setup, the separation between the center of the spherical probe and the nano-pillar is set to 1.3 μm (see FIG. 1), which is a large distance considering the lateral size of the sample. At such distance, the coupling between the sample and the probe is weak [38] as it does not affect the profiles of the intrinsic SW modes in the sample. This is in contrast with the strong coupling regime, where the stray field of the magnetic probe can be used to localize SW modes below the MRFM tip [47]. For our mechanical SW spectrometer, the perturbation of the magnetic sphere reduces to a uniform translation of all the peak positions [48] by −190 Oe (see section III B). In the following, all the SW spectra are recorded with the magnetic sphere at the same exact position above the nano-pillar.

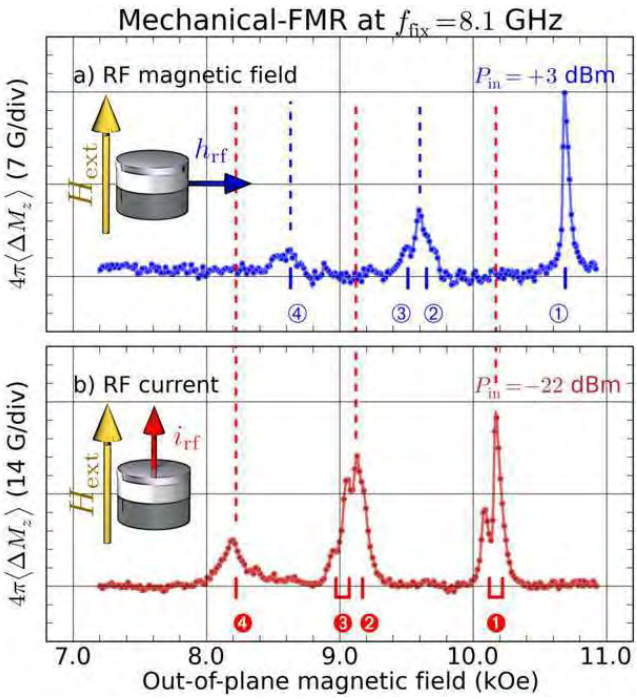

FIG. 2. Comparative spectroscopic study performed by mechanical-FMR at f_{fix} = 8.1 GHz, demonstrating that distinct SW spectra are excited by a uniform in-plane RF magnetic field (a) and by an RF current flowing perpendicularly through the layers (b). The positions of the peaks are reported in Table II.

C. RF magnetic field vs. RF current excitations

The comparative spectroscopic study performed by mechanical-FMR at f_{fix} = 8.1 GHz on the normally magnetized spin-valve nano-pillar is presented in FIG. 2. In these experiments, there is no dc current flowing through the device, and the spectra are obtained in the small excitation regime (precession angles less than 5°, see Sec. VIII A). The upper panel (a) shows the SW spectrum excited by a uniform RF magnetic field applied in the plane of the layers, while the lower panel (b) displays the SW spectrum excited by an RF current flowing perpendicularly through the magnetic layers. The striking result is that these two spectra are different: none of the SW modes excited by the homogeneous RF field is present in the spectrum excited by the RF current flowing through the nano-pillar, and vice versa.

Let us first focus on FIG. 2a, where the obtained absorption spectrum corresponds to the so-called standard FMR spectrum. Here, the output power of the microwave synthesizer at 8.1 GHz is set to +3 dBm, which corresponds to an amplitude of the uniform linearly

polarized RF magnetic field $h_{\rm rf} \simeq 2.1$ Oe produced by the antenna (see Sec. VIII A). In this standard FMR spectrum, only SW modes with non-vanishing spatial average can couple to the homogeneous RF field excitation. In field-sweep spectroscopy, the lowest energy mode occurs at the largest magnetic field. So, the highest field peak at $H_{①} = 10.69$ kOe should be ascribed to the uniform mode. Since this peak is also the largest of the spectrum, it corresponds to the precession of a large volume in the nano-pillar, *i.e.*, the thick layer must dominate in the dynamics. In mechanical-FMR, a quantitative measurement of the longitudinal magnetization is obtained [39, 49] (see Sec. VIII A). The amplitude of the peak at $H_{①}$ corresponds to $4\pi\langle\Delta M_z\rangle \simeq 14$ G, which represents a precession angle $\langle\theta\rangle \simeq 3.1°$. This sharp peak is followed by a broader peak with at least two maxima at $H_{②} = 9.65$ kOe and $H_{③} = 9.51$ kOe, and at lower field, by a smaller resonance around $H_{④} = 8.64$ kOe. Among these other peaks, there is the uniform mode dominated by the thin layer, which has to be identified and distinguished from higher radial index SW modes.

Let us now turn to FIG. 2b, corresponding to the spectroscopic response to an RF current of same frequency 8.1 GHz flowing perpendicularly through the nano-pillar. Here, the output power of the microwave synthesizer is −22 dBm, which corresponds to an rms amplitude of the RF current $i_{\rm rf} \simeq 170$ μA (see Sec. VIII B). The SW spectrum is acquired under the *exact same conditions* as for standard FMR, *i.e.*, the spherical magnetic probe of the mechanical-FMR detection is kept at the same location above the sample. The striking result is that the position of the peaks in FIGS. 2a and 2b do not coincide. More precisely there seems to be a translational correspondence between the two spectra, which are shifted in field by about 0.5 kOe from each other. The lowest energy mode in the RF current spectrum occurs at $H_{❶} = 10.22$ kOe. This is again the most intense peak, suggesting that the thick layer contributes to it, and $4\pi\langle\Delta M_z\rangle \simeq 26$ G, which represents a precession angle $\langle\theta\rangle \simeq 4.2°$. This main resonance line is also split in two peaks, with a smaller resonance in the low field wing of the main peak, about 100 Oe away. At lower field, two distinct peaks appear at $H_{❷} = 9.17$ kOe and $H_{❸} = 9.07$ kOe and another peak is visible at $H_{❹} = 8.22$ kOe.

The fact that the two spectra of FIGS. 2a and 2b are distinct implies that they have a different origin. It will be shown in the theoretical section IV A 3 that the RF field and the RF current excitations probe two different azimuthal symmetries ℓ. Namely, only $\ell = 0$ modes are excited by the uniform RF magnetic field, whereas only $\ell = +1$ modes are excited by the orthoradial RF Oersted field associated to the RF current [50]. The mutually exclusive

nature of the responses to the uniform and orthoradial symmetry excitations is a property of the preserved axial symmetry, where the azimuthal index ℓ is a good quantum number, *i.e.*, different ℓ-index modes are not mixed and can be excited separately (see section IV A 2).

III. EXPERIMENTAL ANALYSIS

In this section, we first look at the effect of a continuous current flowing through the nano-pillar on the SW spectra in order to determine which layer contributes mostly to the resonant signals observed in FIG. 2. Due to the asymmetry of the spin transfer torque in each magnetic layer, the different SW modes are influenced differently depending on the layer in which the precession is the largest. Then, we briefly mention experiments, where spectroscopy is performed by monitoring the dc voltage produced by the magnetization precession in the hybrid nanostructure, and compared to mechanical-FMR. Finally, the analysis of the frequency-field dispersion relation and of the linewidth of the resonance peaks enables to extract the gyromagnetic ratio and the damping parameters in the thick and thin layers.

A. Direct bias current

To gain further insight about the peak indexation, we have measured the spectral evolution produced on the SW spectra of FIG. 2 when a finite dc current $I_{\rm dc} \neq 0$ is injected in the nano-pillar. We recall that for our sign convention, a positive dc current stabilizes the thin layer and destabilizes the thick one due to the spin transfer torque, and vice versa [6, 7]. The results obtained by mechanical-FMR are reported in FIG. 3.

Let us first concentrate on FIG. 3a, in which the excitation that probes the different SW modes is the same as in FIG. 2a, *i.e.*, a uniform RF magnetic field. Two main features can be observed in the evolution of the SW spectra as $I_{\rm dc}$ is varied. First, the amplitude of the peak at $H_{①}$ smoothly increases with the positive current and smoothly decreases with the negative current. At the same time, the peak at $H_{③}$, which is about five times smaller than the peak at $H_{①}$ when $I_{\rm dc} = 0$ mA, almost disappears for positive current and strongly increases at negative current, until it becomes larger than the other peaks when $I_{\rm dc} = -4$ mA. These two features are consistent with the effect of spin transfer if we ascribe the peak at

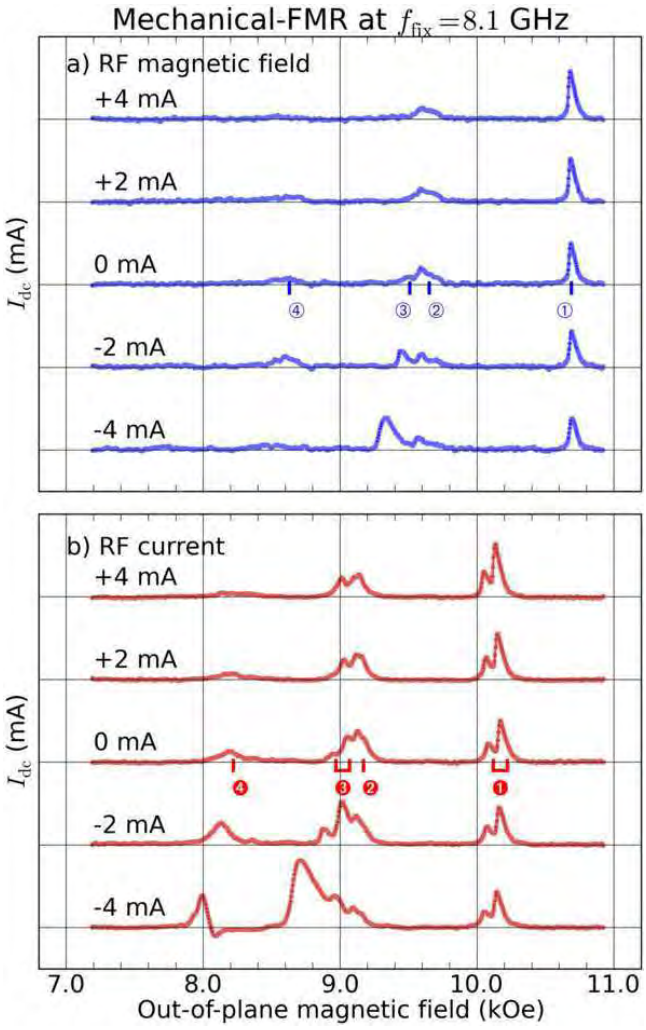

FIG. 3. Evolution of the SW spectra measured at f_{fix} = 8.1 GHz by mechanical-FMR for different values of the continuous current I_{dc} flowing through the nano-pillar. The panel (a) corresponds to excitation by a uniform RF magnetic field and the panel (b) to excitation by an RF current through the sample.

$H_①$ to the uniform mode of mostly the thick layer and the peak at $H_③$ to the one of mostly the thin layer. More precisely, it is expected that in the sub-critical regime ($|I_{dc}| < I_{th}$, where I_{th} is the threshold current for auto-oscillations, $I_{th} < 0$ for the thin layer and $I_{th} > 0$ for the thick layer), the damping scales as $\alpha(1 - I_{dc}/I_{th})$ [25, 26] (see Sec. VII A), where α is the Gilbert damping parameter. It means that the linewidth of a resonance peak that is favored by spin transfer should decrease as the current gets closer to I_{th}, and that its amplitude, which scales as the inverse linewidth, should increase.

Although the effect on the peak amplitude noted above is clear in FIG. 3a, it is not on the

linewidth. The reason is that in this experiment, the strength of the driving RF magnetic field is kept constant to $h_{\mathrm{rf}} = 2.1$ Oe. As a result, the shape of the growing peaks in FIG. 3a becomes more asymmetric, which is a signature that the precession amplitude driven by the RF field is strong enough to change the internal field by an amount of the order of the linewidth. This leads to some foldover of the resonance line [51, 52], a non-linear effect for which details are given in the Sec. VIII A. In other words, the distortion of the line shape as the peak amplitude increases prevents to see the diminution of its linewidth [53]. It would be necessary to decrease the excitation amplitude as the threshold current is approached [26] so as to maintain the peak amplitude in the linear regime in order to reveal it.

The opposite signs of the spin transfer torques which influence the dynamics in the thin and thick layers are thus clearly seen in FIG. 3a. Their relative strengths can also be determined, as the amplitude of the peak at $H_{③}$ grows much faster with negative current than the one of the peak at $H_{①}$ with positive current. This is because the efficiency of the spin transfer torque is inversely proportional to the thickness of the layer [6, 7]. Whereas the precession angle in the thick layer does not vary much with I_{dc} (from $\approx 2.5°$ at -4 mA to $\approx 3.5°$ at $+4$ mA), the precession angle that can be deduced from $\langle \Delta M_z \rangle$ in the thin layer grows from almost zero at $I_{\mathrm{dc}} = +4$ mA to more than $6°$ at $I_{\mathrm{dc}} = -4$ mA. Moreover, the peak position $H_{③}$ shifts clearly towards lower field as the negative current is increased. This is due to the onset of spin transfer driven auto-oscillations in the thin layer, which occurs at a threshold current $I_{\mathrm{th}} \lesssim -4$ mA and produces this non-linear shift [19]. We note, that such a value for the threshold current in the thin layer can be found from Slonczewski's model (see Sec. VII A).

Let us now briefly discuss FIG. 3b, which shows the dependence on I_{dc} of the mechanical-FMR spectra excited by an RF current excitation. A similar dependence on I_{dc} of the resonance peaks in translational correspondence with FIG. 3a is observed. Again, a clear asymmetry is revealed depending on the polarity of I_{dc} and on the SW modes. The double peak at $H_{❶}$ is favored by positive currents, hence it should be ascribed to mostly the thick layer precessing, while the double peak at $H_{❸}$ is strongly favored by negative currents, hence it should be ascribed to mostly the thin layer precessing. Moreover, a careful inspection shows that the peak $H_{❷}$, which looks single at $I_{\mathrm{dc}} = 0$ mA, is actually at least double. We will explain this splitting of higher harmonics modes in section V B.

To summarize, the passage of a dc current through the nano-pillar enables to determine

which layer mostly contributes to the observed SW modes, owing to the asymmetry of the spin transfer effect.

B. Voltage-FMR

Our experimental setup also allows to monitor the dc voltage produced across the nano-pillar by the precession of the magnetization in the bi-layer structure. A lock-in detection is used to measure the difference of voltage across the nano-pillar when the RF is on and off: $V_{\rm dc} = V_{\rm on} - V_{\rm off}$. This can be done *simultaneously* to the acquisition of the mechanical-FMR signal, in the exact same conditions (see FIG. 1). Since the presentation of the experimental results requires a specific discussion, the details as well as the graphs will be published elsewhere. Here, we shall only reveal the three main features that can be noticed in the voltage-FMR spectra.

First, even at $I_{\rm dc} = 0$, dc voltage peaks are produced across the nano-pillar at the same positions as the mechanical-FMR peaks observed in FIG. 2, with a difference of potential that lies in the 10 nV range for the precession angles excited here. It is ascribed to spin pumping and accumulation in the spin-valve hybrid structure [54, 55]. Second, these voltage resonance peaks are signed, namely, the SW modes favored at $I_{\rm dc} < 0$ in FIG. 3a (for which the thin layer is dominating) produce a positive voltage peak, whereas those favored at $I_{\rm dc} > 0$ (thick layer dominating) produce a negative voltage peak. This difference between the thick and thin layer contributions is ascribed to the asymmetry of the spin accumulation in the multi-layer stack [56]. Third, the relative amplitudes of the voltage-FMR peaks are different from the mechanical-FMR ones. For instance, the voltage-FMR peak of the thin layer at $H_③$ is slightly *larger* than the peak at $H_①$ of the thick layer (and it has an opposite sign). This illustrates an important difference between the two detection schemes. While mechanical-FMR measures a quantity proportional to the precessing volume, $\langle \Delta M_z \rangle$, the voltage-FMR measures an interfacial effect. Therefore, when the same precession angle is excited in both layers, the voltage-FMR signal associated to each layer is approximately the same, whereas the mechanical-FMR signal from the thin layer is roughly four times smaller than the one from the thick layer, due to their relative thicknesses.

Finally, we mention that voltage-FMR spectroscopy can also record the intrinsic FMR spectrum of the nano-pillar, *i.e.*, in the absence of the spherical MRFM probe above it.

This enables to check that the only effect introduced by the probe in mechanical-FMR is an overall shift of the SW modes spectra to lower field without any other distortion, and to quantify this shift, found to be −190 Oe [57].

C. Gyromagnetic ratio

A precise orientation of the applied magnetic field $\boldsymbol{H}_{\text{ext}}$ along the normal $\hat{\boldsymbol{z}}$ of the sample (polar angle $\theta_H = (\hat{\boldsymbol{z}}, \boldsymbol{H}_{\text{ext}}) = 0$) enables a direct determination of the modulus γ of the gyromagnetic ratio [38]. By following the frequency-field dispersion relation of the resonance peaks at $H_①$ and at $H_③$ (from 4.5 GHz to 8.1 GHz and from 6.2 GHz to 11 GHz, respectively) in our nano-pillar, it is found that $\gamma = 1.87 \times 10^7$ rad.s^{-1}.G^{-1} is identical in the thick and thin layers. Moreover, the value of γ measured in the nano-pillar is the same as in the extended reference film (see Sec. VIII C and Table I), confirming that the applied field is sufficient to saturate the two magnetic layers and is precisely oriented along $\hat{\boldsymbol{z}}$.

The same result is obtained by following the evolution of the frequency-field dispersion relation presented in FIG. 4. Here, we take advantage of the broadband design of the electrodes which connect the nano-pillar to measure the FMR spectrum at fixed bias magnetic field, $H_{\text{fix}} = 10$ kOe, by sweeping the frequency of the RF current through it. The data are plotted according to the frequency scale above FIG. 4a. At constant magnetic configuration (above the saturation field, *i.e.*, $\gtrsim 8$ kOe), this frequency scale is in correspondence with field-sweep experiments performed at fixed RF frequency $f_{\text{fix}} = 8.1$ GHz through the affine transformation $H_{\text{ext}} - H_{\text{fix}} = 2\pi(f - f_{\text{fix}})/\gamma$, as seen from the field scale below FIG. 4b. This is a direct experimental check of the equivalence between frequency and field sweep experiments in the normally saturated state.

D. Damping parameters

From the FMR data presented above, we can also directly extract the damping parameters in each Permalloy layer. Indeed, in field-sweep spectroscopy in the normal orientation ($\theta_H = 0$), the full width at half-maximum (FWHM) ΔH of a resonance line is proportional to the excitation frequency $\omega/(2\pi)$ through the Gilbert constant α: $\Delta H = 2\alpha(\omega/\gamma)$ (see Sec. VII A).

The linewidth of the peak at $H_①$ associated to mainly the thick layer in FIG. 2a is equal to

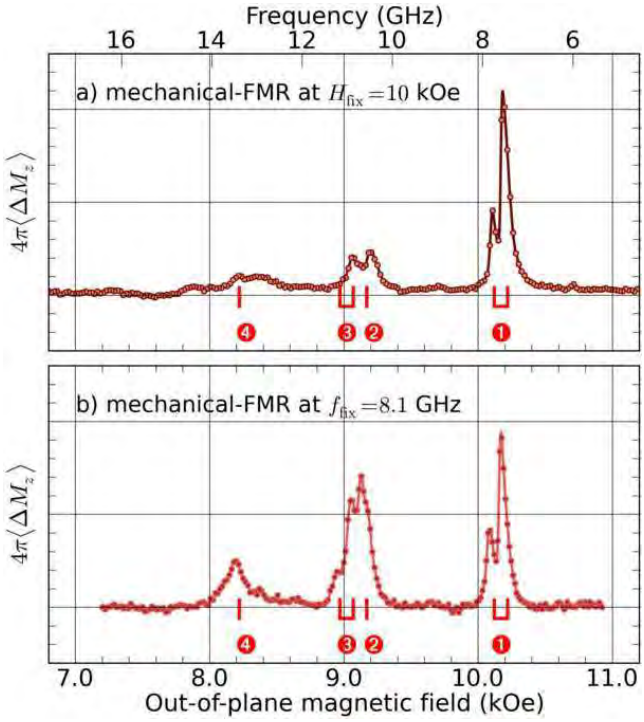

FIG. 4. Frequency-field dispersion relation: the top spectrum (a) is measured at fixed bias field $H_{\rm fix}$ = 10 kOe by sweeping the frequency of the RF current $i_{\rm rf}$ through the nano-pillar. The bottom spectrum (b) is the same as in FIG. 2b, and is obtained by sweeping the magnetic field at fixed frequency $f_{\rm fix}$ = 8.1 GHz of $i_{\rm rf}$. The top and bottom scales are in correspondence through the affine transformation $H_{\rm ext} - H_{\rm fix} = 2\pi(f - f_{\rm fix})/\gamma$.

$\Delta H_{①}$ = 48 Oe, which corresponds to a damping $\alpha_{①} = 0.88\times10^{-2}$. From the same mechanical-FMR spectrum, the linewidth of the peak at $H_{③}$, associated to mainly the thin layer, cannot be easily extracted due to the proximity of the peak at $H_{②}$. Owing to the interfacial origin of the voltage-FMR signal, the peak at $H_{③}$ is more distinguishable in the spectrum of the voltage-FMR (not shown), and its linewidth, $\Delta H_{③}$ = 70 Oe, can be fitted. It corresponds to a damping $\alpha_{③} = 1.29\times10^{-2}$.

The linewidths of the modes at $H_{❶}$ and $H_{❸}$ can also be fitted and give similar results for the damping associated to each layer. In the case of the RF current excitation, a frequency-sweep spectrum can be acquired at a fixed bias magnetic field $H_{\rm fix}$ (see FIG. 4). In that case, the damping constant is simply obtained by $\alpha = \Delta f/(2f)$, where Δf is the width of the line centered at f. At $H_{\rm fix}$ = 10 kOe, $f_{❶}$ = 7.37 GHz and $\Delta f_{❶}$ = 0.12 GHz, which yield $\alpha_{❶} = 0.81\times10^{-2}$, and $f_{❸}$ = 10.92 GHz and $\Delta f_{❸}$ = 0.33 GHz, which yield $\alpha_{❸} = 1.5\times10^{-2}$.

TABLE I. Magnetic parameters of the thin Py_a and thick Py_b layers measured by cavity-FMR on the reference film (top row) and by mechanical-FMR in the nano-pillar (bottom row).

$4\pi M_a$ (G)	α_a	$4\pi M_b$ (G)	α_b	γ (rad $\cdot$ s^{-1} $\cdot$ G^{-1})
8.2×10^3	1.5×10^{-2}	9.6×10^3	0.9×10^{-2}	1.87×10^7
8.0×10^3	1.4×10^{-2}	9.6×10^3	0.85×10^{-2}	1.87×10^7

In summary, we retain the following values for the damping parameters in respectively the thin and the thick layers: $\alpha_a = (1.4 \pm 0.2) \times 10^{-2}$ and $\alpha_b = (0.85 \pm 0.1) \times 10^{-2}$. We have reported them, together with γ, in Table I.

These two values are in line with the ones obtained on the reference film, which have also been reported in Table I. Still, we observe that the linewidths in the nanostructure are systematically lower than the ones measured on the reference film. This is a constant characteristic that we associate to the confined geometry, which lifts most of the degeneracy (well separated SW modes) and thus strongly reduces the inhomogeneous part of the linewidth observed in the infinite layer [15, 26]. Rather, the inhomogeneities associated to the magnetic layers [15] or to the confinement geometry will lead to some mode splitting in the nanostructure (see section V B). We have checked that the inhomogeneous contribution to the linewidth in the nano-pillar is weak, by following the dependence of the measured ΔH as a function of frequency. In fact, the increase of $\Delta H_③$ from 70 Oe at 8.1 GHz to 105 Oe at 11 GHz is purely homogeneous.

Finally, the finding that the damping is larger in the thin layer than in the thick layer is ascribed to the adjacent metallic layers [58]. In fact, non-local effects such as the spin pumping effect [54, 59] and the spin diffusion in the adjacent normal layers by the conduction electrons yield an interfacial increase of the magnetic damping [60], stronger in the case of thin layers.

IV. THEORETICAL ANALYSIS

In this section, we first review a general formalism allowing the calculation of the discrete spectrum associated with SW propagation inside a confined body of arbitrary magnetic configuration. It is shown that in the two-dimensional (2D) axially symmetric case, different ℓ-index modes can be excited separately, as found experimentally in section II C. The classification of the SW modes in this case is also used to extract the parameters of each magnetic layer from the experimental FMR spectra. In a second part, we discuss the influence of the dynamic coupling between the magnetic disks, where the collective dynamics splits into binding and anti-binding modes. It is shown that in our experimental case, the dynamic dipolar coupling introduces a weak spectral shift, although its influence on the character of the SW modes is real. In the last part, a comparison to full three-dimensional (3D) micromagnetic simulations is performed in order to study in details the collective dynamics in the nano-pillar.

A. Analytical model

1. *General theory*

Below, we briefly review the general theory of linear SW excitations (see Sec. VII A for more details). We consider an arbitrary equilibrium magnetic configuration, where the local magnetization writes $M_s\hat{\boldsymbol{u}}$, with M_s the saturation magnetization and $\hat{\boldsymbol{u}}$ the unit vector along the local equilibrium direction (implicitly dependent on the spatial coordinates). The linearization of the *local* equation of motion is obtained by decomposing the instantaneous magnetization vector $\boldsymbol{M}(t)$ into a static and dynamic component [61] (see FIG. 5). We shall use the following ansatz:

$$\frac{\boldsymbol{M}(t)}{M_s} = \hat{\boldsymbol{u}} + \boldsymbol{m}(t) + \mathcal{O}(\boldsymbol{m}^2)\,, \tag{2}$$

where the transverse component $\boldsymbol{m}(t)$ is the small dimensionless deviation ($|\boldsymbol{m}| \ll 1$) of the magnetization from the equilibrium direction. In ferromagnets, $|\boldsymbol{M}| = M_s$ is a constant of the motion, so that the local orthogonality condition $\hat{\boldsymbol{u}} \cdot \boldsymbol{m} = 0$ is required.

Substituting Eq. (2) in the lossless Landau-Lifshitz equation Eq. (21) (see Sec. VII A) and keeping only the terms linear in $\boldsymbol{m}$, one obtains the following dynamical equation for

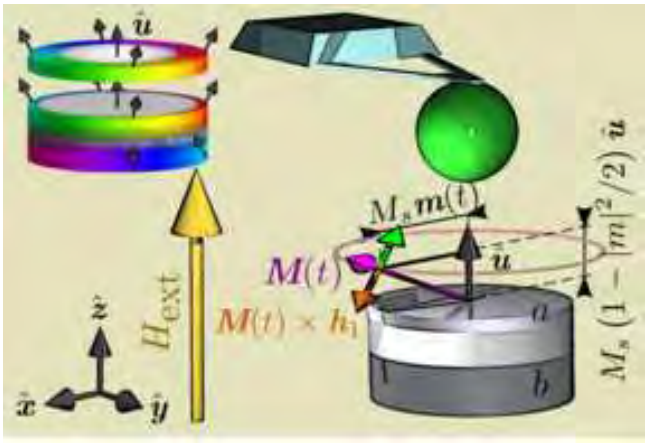

FIG. 5. Schematic representation of the magnetization dynamics under continuous RF excitation. In the steady state, the torque exerted by the RF perturbation field $\boldsymbol{h}_1$ (orange arrow) compensates the torque exerted by the damping (green), and the local magnetization vector $\boldsymbol{M}(t)$ (purple) precesses at the Larmor frequency on a circular orbit around the local equilibrium direction (unit vector $\hat{\boldsymbol{u}}$). $\boldsymbol{M}(t)$ is the vector sum of a small oscillating component $M_s\boldsymbol{m}$ and a large static component $M_s\left(1-|\boldsymbol{m}|^2/2\right)$, respectively transverse and parallel to $\hat{\boldsymbol{u}}$. The inset shows the simulated spatial distribution of $\hat{\boldsymbol{u}}$ inside the nano-pillar at $\boldsymbol{H}_{\rm ext}$ = 10 kOe (see section IV C). In the white regions, the magnetization is aligned along the normal $\hat{\boldsymbol{z}}$ within 0.05°. In the colored regions, $\hat{\boldsymbol{u}}$ is flaring (< 5°) in the radial direction (the hue indicates the direction of $\hat{\boldsymbol{u}}-\hat{\boldsymbol{z}}$ according to the color code defined in FIG. 6).

$\boldsymbol{m}$:

$$\frac{\partial \boldsymbol{m}}{\partial t} = \hat{\boldsymbol{u}} \times \widehat{\boldsymbol{\Omega}} * \boldsymbol{m}\,, \tag{3}$$

where here and henceforth, tensor operators are indicated by wide hat, the cross product is denoted by $\times$ and the convolution product is denoted by $*$. The self-adjoint tensor operator $\widehat{\boldsymbol{\Omega}}$ represents the Larmor frequency:

$$\widehat{\boldsymbol{\Omega}} = \gamma H \widehat{\boldsymbol{I}} + 4\pi\gamma M_s \widehat{\boldsymbol{G}}\,, \tag{4}$$

where γ is the modulus of the gyromagnetic ratio, H is the scalar effective magnetic field, $\widehat{\boldsymbol{I}}$ is the identity matrix, and $\widehat{\boldsymbol{G}}$ is the linear tensor operator describing the magnetic self-interactions. The later is the addition of several contributions $\widehat{\boldsymbol{G}}^{(d)} + \widehat{\boldsymbol{G}}^{(e)} + ...$, respectively the magneto-dipolar interactions, the inhomogeneous exchange, etc... (see Sec. VII B). The

effective magnetic field $\boldsymbol{H}$ is a vector aligned along $\hat{\boldsymbol{u}}$, whose norm is

$$H = \hat{\boldsymbol{u}} \cdot \boldsymbol{H}_0 - 4\pi M_s \hat{\boldsymbol{u}} \cdot \widehat{\boldsymbol{G}} * \hat{\boldsymbol{u}}\,, \tag{5}$$

the sum of the $\hat{\boldsymbol{u}}$–component of $\boldsymbol{H}_0$, the total applied magnetic field including the stray field of any nearby magnetic object (in our case, the adjacent magnetic layer in the nano-pillar and the spherical probe), reduced by the static self-interactions, which include the depolarization magnetic field along $\hat{\boldsymbol{u}}$ created by the static component of the magnetization.

SW modes $\boldsymbol{m}_\nu$ are by definition eigen-solutions of Eq. (3):

$$-i\omega_\nu \boldsymbol{m}_\nu = \hat{\boldsymbol{u}} \times \widehat{\boldsymbol{\Omega}} * \boldsymbol{m}_\nu\,. \tag{6}$$

Here ω_ν is the SW eigen-frequency and ν is a set of indices to enumerate the different modes.

The main properties of SW excitations follow from the eigen problem Eq. (6) and the fact that the operator $\widehat{\boldsymbol{\Omega}}$ is self-adjoint and real. One can show that the eigen solutions obey the closure relation

$$i\left\langle \overline{\boldsymbol{m}}_\nu \cdot (\hat{\boldsymbol{u}} \times \boldsymbol{m}_{\nu'}) \right\rangle = \mathcal{N}_\nu \delta_{\nu,\nu'}\,, \tag{7}$$

where δ is the Kronecker delta function and $\overline{\boldsymbol{m}}$ stands for the complex conjugate of $\boldsymbol{m}$. Here we have used the chevron bracket notation introduced in Eq. (1) to denote the spatial average. The quantities $\mathcal{N}_\nu$ are real normalization constants, which depend on the choice of eigen-functions $\boldsymbol{m}_\nu$. If the equilibrium magnetization $\hat{\boldsymbol{u}}$ corresponds to a (local) minimum of the energy, then the operator $\widehat{\boldsymbol{\Omega}}$ is positive-definite. It follows that the "physical" modes with $\omega_\nu > 0$ have positive norm $\mathcal{N}_\nu > 0$. In this formalism, the eigen-frequencies ω_ν can be calculated as

$$\omega_\nu = \frac{\left\langle \overline{\boldsymbol{m}}_\nu \cdot \widehat{\boldsymbol{\Omega}} * \boldsymbol{m}_\nu \right\rangle}{\mathcal{N}_\nu}. \tag{8}$$

The importance of this relation is that the frequencies ω_ν calculated using Eq. (8) are variationally stable with respect to perturbations of the mode profile $\boldsymbol{m}_\nu$. Thus, injecting some trial vectors inside Eq. (8) allows one to get approximate values of ω_ν with high accuracy [62]. The trial vectors should obey some simple properties: i) they should form a complete basis in the space of vector functions $\boldsymbol{m}$, ii) be locally orthogonal to $\hat{\boldsymbol{u}}$ and iii) satisfy appropriate boundary conditions at the edges of the magnetic body [63].

2. Normally magnetized disks

In this part, we shall establish a SW modes basis $\boldsymbol{m}_\nu$ for a normally magnetized disk. A specific feature of the considered geometry is its azimuthal symmetry. Mathematically, this means that the operator $\hat{\boldsymbol{u}}\times\widehat{\boldsymbol{\Omega}}$ commutes with the operator $\widehat{\boldsymbol{R}}_z$ that describes an infinitesimal rotation about the $\hat{\boldsymbol{z}}$ axis, assuming that the boundary conditions are invariant under such a rotation.

This particular configuration allows us to classify the SW modes according to their behavior under the rotations in the (x, y) plane. Namely, SW eigen-modes are also eigen-functions of the operator $\widehat{\boldsymbol{R}}_z$ corresponding to a certain integer azimuthal number ℓ:

$$\frac{\partial \boldsymbol{m}}{\partial \phi} - \hat{\boldsymbol{z}} \times \boldsymbol{m} = -i(\ell - 1)\boldsymbol{m}. \tag{9}$$

Here, ϕ is the azimuthal angle of the polar coordinate system.

As one can see, Eq. (9) determines the vector structure of SW modes and their dependence on the angle ϕ. Namely, Eq. (9) for a fixed ℓ has two classes of solutions:

$$\boldsymbol{m}_\ell^{(1)} = \frac{1}{2}(\hat{\boldsymbol{x}} + i\hat{\boldsymbol{y}})e^{-i\ell\phi}\psi_\ell^{(1)}(\rho)\,, \tag{10a}$$

and

$$\boldsymbol{m}_\ell^{(2)} = \frac{1}{2}(\hat{\boldsymbol{x}} - i\hat{\boldsymbol{y}})e^{-i(\ell-2)\phi}\psi_\ell^{(2)}(\rho)\,, \tag{10b}$$

where the functions $\psi_\ell^{(1,2)}(\rho)$ describe the dependence of the SW mode on the radial coordinate ρ and have to be determined from the dynamical equations of motion. So, the azimuthal symmetry allows one to reduce the 2D (ρ and ϕ) vector equations to a one-dimensional (ρ) scalar problem.

Generally speaking, SW eigen-modes are certain linear combinations of both possible ℓ-forms Eqs. (10). The coupling of these two forms is due solely to the inhomogeneous dipolar interaction. In our experimental case (lowest energy modes of a relatively thin disk) one can completely neglect this coupling [64] and consider only the right-polarized form Eq. (10a). In the following we will drop the superscript (1) in $\boldsymbol{m}_\ell^{(1)}$ and $\psi_\ell^{(1)}$.

We shall now find an appropriate set of radial functions $\psi_\ell(\rho)$ to calculate the SW spectrum using Eq. (8). Here, we can take advantage of the variational stability of Eq. (8) and, instead of the exact radial profiles $\psi_\ell(\rho)$ (to find them one has to solve integro-differential equations), use some reasonable set of functions. Namely, it is known that the dipolar interaction in thin disks or prisms does not change qualitatively the profile of SW modes,

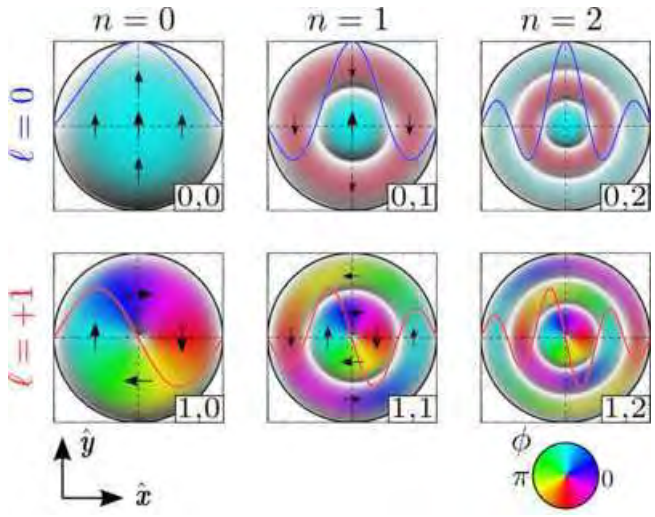

FIG. 6. Color representation of the Bessel spatial patterns for different values of the azimuthal mode index ℓ (by row) and radial mode index n (by column). The arrows are a snapshot of the transverse magnetization $\boldsymbol{m}_\nu$, labeled by the index $\nu = \ell, n$. All arrows are rotating synchronously in-plane at the SW eigen-frequency. In our coding scheme, the hue indicates the phase $\phi = \arg(\boldsymbol{m}_\nu)$ (or direction) of $\boldsymbol{m}_\nu$, and the brightness the amplitude of $|\boldsymbol{m}_\nu|^2$. The nodal positions ($|\boldsymbol{m}_\nu| = 0$) are marked in white.

but introduces effective pinning at the lateral boundaries [63]. Therefore, we will use radial profiles of the form $\psi_\ell(\rho) = J_\ell(k_{\ell,n}\rho)$, where $J_\ell(x)$ is the Bessel function and $k_{\ell,n}$ are SW wave-numbers determined from the pinning conditions at the disk boundary $\rho = R$. For our experimental conditions ($t_a, t_b \ll R$), the pinning is almost complete, and we shall use $k_{\ell,n} = \kappa_{\ell,n}/R$, where $\kappa_{\ell,n}$ is the n-th root of the Bessel function of the ℓ-th order.

FIG. 6 shows a color representation of the Bessel spatial patterns for different values of the index $\nu = \ell, n$. We restrict the number of panels to two values of the azimuthal mode index, $\ell = 0, +1$, with the radial index varying between $n = 0, 1, 2$. In our color code, the hue indicates the phase (or direction) of the transverse component $\boldsymbol{m}_\nu$, while the brightness indicates the amplitude of $|\boldsymbol{m}_\nu|^2$. The nodal positions are marked in white. A node is a location where the transverse component vanishes, *i.e.*, the magnetization vector is aligned along the equilibrium axis. This coding scheme provides a distinct visualization of the phase and amplitude of the precession profiles. The black arrows are a snapshot of the $\boldsymbol{m}_\nu$ vectors in the disk and are all rotating synchronously in-plane at the SW eigen-frequency.

The top left panel shows the $\nu = 0, 0$ ($\ell = 0$, $n = 0$) mode, also called the uniform mode.

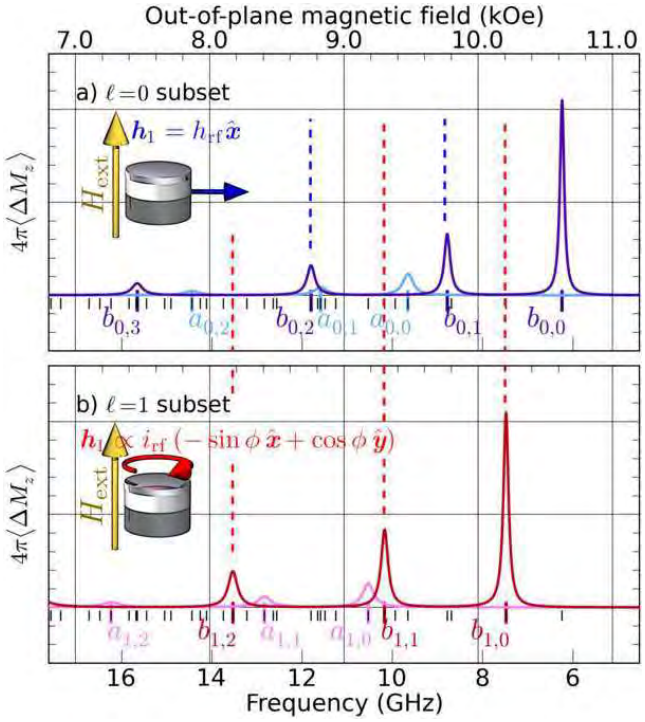

FIG. 7. Analytically calculated spectra at $H_{\rm fix}$ = 10 kOe using the set of Bessel functions (see FIG. 6) as the trial eigen-vectors. The panel (a) shows the linear response to a uniform excitation field $\hat{\boldsymbol{h}}_1 = \hat{\boldsymbol{x}}$ and the panel (b) to an orthoradial excitation field $\hat{\boldsymbol{h}}_1 = -\sin\phi\,\hat{\boldsymbol{x}} + \cos\phi\,\hat{\boldsymbol{y}}$. A light (dark) color is used to indicate the energy stored Eq. (12) in the thin Py_a and thick Py_b layers.

It usually corresponds to the lowest energy mode since all the vectors are pointing in the same direction at all time. Below is the $\ell = +1$, $n = 0$ mode. It corresponds to SWs that are rotating around the disk in the same direction as the Larmor precession. The corresponding phase is in quadrature between two orthogonal positions and this mode has a node at the center of the disk. The variation upon the $n = 0, 1, 2$ index (ℓ being fixed) shows higher order modes with an increasing number of nodal rings. Each ring separates regions of opposite phase along the radial direction. All these spatial patterns preserve the rotation invariance symmetry.

3. Selection rules

Using the complete set of Bessel functions in Eq. (8), one can obtain analytically the discrete spectrum of eigen-values for both the thin and thick layers. The details of the

numerical application can be found in Sec. VII B. The spectral values are displayed in FIG. 7 using vertical ticks labeled $\nu = j_{\ell n}$, where $j = a, b$ indicates the precessing layer, and ℓ, n the azimuthal and radial mode indices. They are calculated at fixed applied field $H_{\text{fix}} = 10$ kOe and placed on the graphs according to the frequency scale below FIG. 7b, which is in correspondence with the field scale above FIG. 7a (see III C for the equivalence between field- and frequency-sweep experiments).

The comparison with the experimental data in FIGS. 2a and 2b shows that the coupling to an external coherent source depends primarily on the ℓ-index. Indeed, this index carries the discriminating symmetry in SW spectroscopy [65]. This is because the excitation efficiency is proportional to the overlap integral

$$h_\nu = \frac{\langle \overline{\boldsymbol{m}}_\nu \cdot \boldsymbol{h}_1 \rangle}{\mathcal{N}_\nu}\,, \tag{11}$$

where $\boldsymbol{h}_1(\boldsymbol{r})$ is the spatial profile of the external excitation field. It can be easily shown that a uniform RF magnetic field, $\boldsymbol{h}_1 = h_{\text{rf}}\boldsymbol{x}$, can only excite $\ell = 0$ SW modes. We have shown in FIG. 7a the predicted position of these modes with blue tone ticks. Obviously the largest overlap is obtained with the so-called uniform mode ($n = 0$). Higher radial index modes ($n \neq 0$) still couple to the uniform excitation but with a strength that decreases as n increases [37, 66]. The $\ell \neq 0$ normal modes, however, are hidden because they have strictly no overlap with the excitation. The comparison with the experimental spectrum in FIG. 2a confirms that conventional FMR [67] probes only partially the possible SW eigen-modes, along the $\ell = 0$-index value. In contrast, the RF current-created Oersted field, $\boldsymbol{h}_1 = h_{\text{Oe}}(\rho)(-\sin\phi\,\hat{\boldsymbol{x}} + \cos\phi\,\hat{\boldsymbol{y}})$ has an orthoradial symmetry and can only excite $\ell = +1$ SW modes. We have shown in FIG. 7b the predicted position of these modes with red tone ticks. They are in good agreement with the resonance positions observed in FIG. 2b. We also note that the $\ell = 0$ and $\ell = +1$ spectra calculated analytically bear similar a/b and n index series as a function of energy. This explains why the two spectra in FIGS. 2a and 2b look in translational correspondence with each other. We emphasize that the same translational correspondence would have been observed for any higher azimuthal order $\ell > 1$ index spectra.

From the coupling to the excitation field expressed by Eq. (11), one can also calculate the mechanical-FMR signal $\propto \langle \Delta M_z \rangle$, proportional to the energy stored in the magnetic

system [39, 45]. For an arbitrary pulsation frequency ω,

$$4\pi \langle \Delta \boldsymbol{M} \cdot \hat{\boldsymbol{u}} \rangle \simeq 4\pi M_s \sum_\nu \frac{\gamma^2 |h_\nu|^2}{(\omega - \omega_\nu)^2 + \Gamma_\nu^2} \mathcal{N}_\nu \,, \tag{12}$$

where the SW damping rate Γ_ν is given by Eq. (28) in Sec. VII A. Eq. (12) is derived under the approximation that the only relevant coefficients in the damping matrix are the diagonal terms. It has been used to compute the relative peak amplitudes in the analytically calculated spectra of FIG. 7.

4. Comparison with experiments

The analytical model outlined in sections IV A 1 and IV A 2 can be used to analyze the experimental spectra of FIG. 2, and to extract some useful parameters of the nano-pillar. More details can be found in the Sec. VII B along with an approximate expression for the SW frequencies in the form of Kittel's traditional formula (with renormalized values of the effective self-demagnetization fields). This Kittel's formula, derived for the $\ell = 0$ spectrum, should be used to analyze the SW spectrum excited by a uniform RF field to yield the correct values of the magnetization in our nano-pillar. Identifying the experimental peaks at $H_③$ and $H_①$ as the lowest energy modes of the thin Py_a and thick Py_b layers yields their respective magnetizations $4\pi M_a = 8.0 \times 10^3$ G and $4\pi M_b = 9.6 \times 10^3$ G, see Eq. (52). These values have been reported in Table I, together with those measured in the reference film (see Sec. VIII C). The magnetizations extracted in the nano-pillar are the same as in the extended film. The only small difference concerns the magnetization of the thin layer, which is 200 G lower in the nanostructure than in the reference film (where $4\pi M_a = 8.2 \times 10^3$ G). We attribute this to some interdiffusion between Py and Cu or Au at the interfaces of the thin layer, which can happen during the etching process of the nano-pillar.

Second, the separation between SW modes crucially depends on the lateral confinement in the nano-pillar and thus on the precise value of its radius. Experimentally, the measured field separation between the two first peaks in FIG. 2a (FIG. 2b), which differ by an additional node in the radial direction, is $H_① - H_②$ = 1.04 kOe ($H_❶ - H_❷$ = 1.05 kOe). Using the nominal radius 100 nm in the analytical model predicts that consecutive n-index mode ($n = 0$ and $n = 1$ modes) should be separated by 1.33 kOe, which is larger than the observed value. This separation drops to 1.05 kOe for a larger disk radius R = 125 nm, which we thus refer to

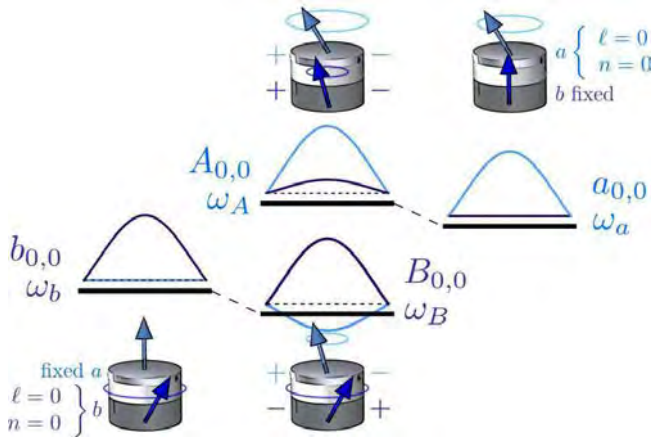

FIG. 8. Schematic representation of the coupled dynamics between two different magnetic disks. Here, ω_b, the eigen-frequency of the lowest energy precession mode in the thick layer (the thin layer being fixed at equilibrium) is smaller than ω_a, the one in the thin layer (the thick layer being fixed at equilibrium). When the two disks are dynamically coupled through the dipolar interaction, the binding state B corresponds to the two layers oscillating in anti-phase at ω_B, with the precession occurring mostly in the thick layer, whereas the anti-binding state A corresponds to the layers oscillating in phase at ω_A, with the precession mostly in the thin layer. This is shown by displaying the dipolar charges and the precession profile $\boldsymbol{m}(\rho)$ in each layer using a light (dark) color to represent the contribution of the thin (thick) layer.

as the radius of our nano-pillar. This value of R also allows to estimate the shift between the $\ell = 0$ and $\ell = +1$ spectra, found to be 530 Oe, in good agreement with the experimental value $H_{①} - H_{❶} = 470$ Oe observed in FIG. 2.

B. Influence of dipolar coupling between different layers

In the treatment above we have neglected the dynamic coupling between the two magnetic disks in dipolar interaction. In general, the interaction between two identical magnetic layers will lead to the hybridization of the same ν-index mode of each layer into two collective modes: the acoustic mode, where the layers are precessing in phase, and the optical mode, where they are precessing in anti-phase. This has been observed in interlayer-exchange-coupled thin films [68] and in trilayered wires where the two magnetic stripes are dipolarly coupled [69]. In the case where the two magnetic layers are not identical (different ge-

ometry or magnetic parameters), this general picture continues to subsist. Although both isolated layers have eigen-modes with different eigen-frequencies, the collective magnetization dynamics still splits in a binding and anti-binding state. But here, the precession of magnetization can be more intense in one of the two layers and the spectral shift of the coupled SW modes with respect to the isolated SW modes is reduced, as it was observed in both the dipolarly-[69] and exchange-coupled cases [70].

Here, we assume that the dominant coupling mechanism between the Py layers is the magnetic dipolar interaction. We neglect any exchange coupling between the magnetic layers mediated through the normal spacer or any coupling associated to pure spin currents [14] in our all-metallic spin-valve structure. To analyze the influence of the dipolar coupling between the two magnetic layers, one can complement the perturbation theory derived in the previous section IV A and in the Sec. VII A. Denoting c_j, the SW amplitudes in j-th disk , one can get from Eq. (26):

$$\frac{dc_a}{dt} = -i\omega_a c_a + i\gamma h_{a,b} c_b \,, \tag{13a}$$

$$\frac{dc_b}{dt} = -i\omega_b c_b + i\gamma h_{b,a} c_a \,, \tag{13b}$$

where ω_j is the frequency of the j-th disk ($j = a, b$) with account of only the static field of the j'-th disk ($j' = b, a$) (*i.e.*, with $\boldsymbol{M}'_j$ fixed at equilibrium, see FIG. 8). The cross term $h_{j,j'}$ is given by

$$h_{j,j'} = -\frac{4\pi M_{j'}}{\mathcal{N}_j} \left\langle \overline{\boldsymbol{m}}_j \cdot \widehat{\boldsymbol{G}}^{(d)} * \boldsymbol{m}_{j'} \right\rangle_j \,. \tag{14}$$

Here, $\widehat{\boldsymbol{G}}^{(d)}$ represents the magneto-dipolar interaction, $M_{j'}$ is the saturation magnetization of the j'-th disk and the averaging goes over the volume of j-th disk. Thus, $h_{j,j'}$ is the average over the j-th mode of the magnetic field created by the magnetization of the j'-th disk. It can be shown that the overlap defined in Eq. (14) is maximum between mode pairs bearing similar wave-numbers in each layer (*i.e.*, the same set of indices ν) [69]. This is the reason why dropping the index ν in Eqs. (13) and (14) is a reasonable approximation.

The anti-binding (A) and binding (B) eigen-frequencies of Eqs. (13) have the form

$$\omega_{A,B} = \frac{\omega_a + \omega_b}{2} \pm \sqrt{\left(\frac{\omega_a - \omega_b}{2}\right)^2 + \Omega^2} \,, \tag{15}$$

where

$$\Omega^2 = \gamma^2 h_{a,b} h_{b,a} \,. \tag{16}$$

In the case when the dipolar coupling is small ($\Omega \ll |\omega_a - \omega_b|$), the eigen-frequencies can be written as (we assume $\omega_a > \omega_b$)

$$\omega_A = \omega_a + \frac{\Omega^2}{\omega_a - \omega_b}\,, \tag{17}$$

$$\omega_B = \omega_b - \frac{\Omega^2}{\omega_a - \omega_b}\,. \tag{18}$$

These equations can be used for quantitative purposes when $\Omega/|\omega_a - \omega_b| < 0.3$ in which case they describe frequency shift with accuracy better than 10%. Thus, the larger of the frequencies (ω_a) shifts up by

$$\Delta\omega = \frac{\Omega^2}{\omega_a - \omega_b}\,, \tag{19}$$

while the smaller one (ω_b) shifts down by the same amount. This effect is summarized in FIG. 8.

A numerical estimate of the coupling strengths $h_{a,b}$ and $h_{b,a}$ between the lowest energy SW modes in each disk can be found in Sec. VII B. The obtained result is very close to the approximate estimation used in Ref.[71], where the spatial structure of the interacting SW modes is ignored to calculate the dipolar coupling between uniformly precessing disks. For the experimental parameters, $\Omega/2\pi \simeq 0.5$ GHz. This coupling is almost an order of magnitude smaller than the frequency splitting $\omega_a - \omega_b$, caused, mainly, by the difference of effective magnetizations of two disks: $\gamma 4\pi(M_b - M_a) \simeq 2\pi \cdot 4.5$ GHz. As a result, the shift of the resonance frequencies due to the dipolar coupling is negligible, $\Delta\omega/2\pi \simeq 0.06$ GHz.

Using Eqs. (13), one can also estimate the level of mode hybridization due to the dipolar coupling. For instance, at the frequency $\omega_A \approx \omega_a$, the ratio between the precession amplitudes in the two layers is given by

$$|c_b/c_a|_{\omega_A} = \Delta\omega/(\gamma h_{a,b}) \simeq \frac{\Omega}{\omega_a - \omega_b}\,. \tag{20}$$

For the experimental parameters, $\Omega/(\omega_a - \omega_b) \approx 0.1$, *i.e.*, the precession amplitude in the disk b is about 10 % of that in the disk a. Thus, although the dipolar coupling induces a small spectral shift (second order in the coupling parameter, Eq. (19)), its influence in the relative precession amplitude is significant (first order in the coupling parameter, Eq. (20)). Finally, we point that here the dipolar coupling is anti-ferromagnetic, and that the binding (lower energy) mode B always corresponds to the thick layer mainly precessing, with the thin layer vibrating in anti-phase, and vice-versa for the anti-binding (in-phase) mode A (see dipolar charges in FIG. 8).

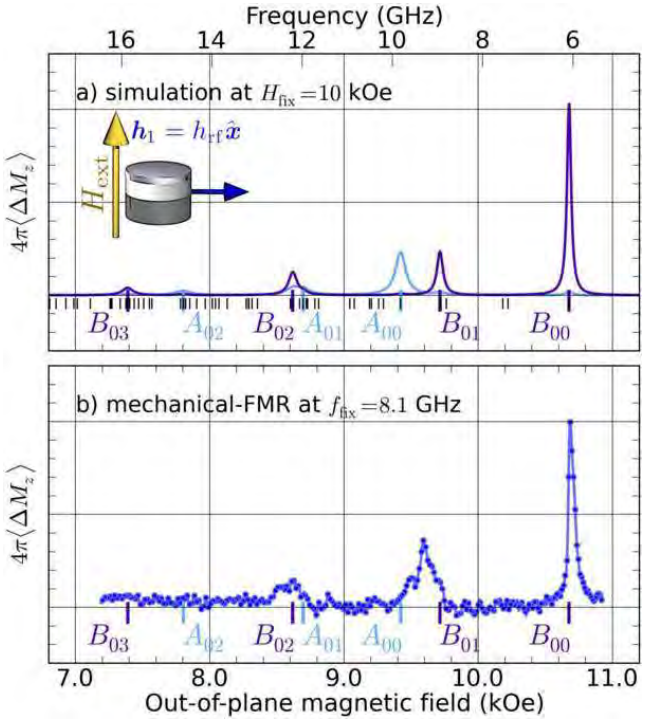

FIG. 9. Panel (a) is the numerically calculated spectral response to a uniform excitation field $\boldsymbol{h}_1 \propto \hat{\boldsymbol{x}}$, from a 3D micromagnetic simulation performed at $H_{\rm fix}$ = 10 kOe. The peaks are labeled according to their precession profiles shown in FIG. 11. A light (dark) color is used to indicate the energy stored in the thin (thick) layer. Panel (b) recalls the experimental spectrum measured by mechanical-FMR when exciting the nano-pillar by a homogeneous RF magnetic field at $f_{\rm fix}$ = 8.1 GHz.

C. Micromagnetic simulations

In the analytical formalism presented above, several approximations have been made. For instance, we have assumed total pinning at the disks boundary for the SW modes and no variation of the precession profile along the disks thicknesses (2D model), and we have neglected the dependence on ν of the dynamic dipolar coupling. Still, it allows to extract important parameters in our nano-pillar, such as its radius and the magnetization in both layers. It also describes the influence of the dynamic dipolar coupling on the position and collective character of the SW modes.

Instead of developing a more complex analytical formalism, we have performed innovative 3D micromagnetic simulations in order to go beyond the approximations mentioned above,

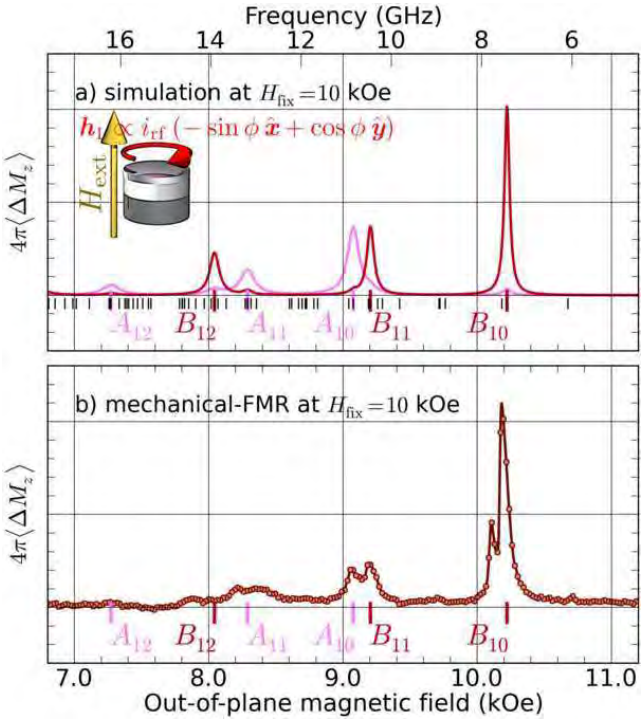

FIG. 10. Panel (a) is the simulated spectral response to an orthoradial excitation field $\boldsymbol{h}_1 \propto -\sin\phi\,\hat{\boldsymbol{x}} + \cos\phi\,\hat{\boldsymbol{y}}$. Panel (b) recalls the experimental spectrum measured by mechanical-FMR for an RF current excitation.

and to unambiguously identify the SW modes observed in our nano-pillar sample. For that purpose, we have used a combination of micromagnetic simulation solvers available as part of SpinFlow 3D, a finite element based simulation platform for spintronics developed by In Silicio [72]. The steady state micromagnetic solver used to obtain numerical approximations of micromagnetic equilibrium states is based on a weak formulation and Galerkin type finite element implementation of the very efficient projection scheme introduced in Ref.[73]. A second numerical solver, a micromagnetic Eigen solver, has been used for fast calculations of lossless 3D SW eigen-modes. It is based on a finite element discretization of the generalized eigen-value problem defined by the linearized lossless magnetization dynamics in the vicinity of an arbitrary pre-computed equilibrium state, following an approach very similar to the one introduced in Ref.[74]. The discrete generalized eigen-value problem is solved with an iterative Arnoldi method using the ARPACK library [75]. In this calculation the full complexity of the 3D micromagnetic dynamics of the presently considered bilayer system is preserved. The solver outputs both the eigen-values by increasing energy order and the

associated eigen-vectors. Several tens of SW eigen-modes can be accurately computed in a matter of few minutes of CPU time with a standard desktop PC, for magnetic thin film nano-structures with typical lateral sizes in the 100 nm range. This is two to three orders of magnitude faster compared to the required computation time when using more traditional approaches for micromagnetic computation of SW eigen-modes, which are typically based on the Fourier component analysis of time series generated by the solution of the full non-linear Landau-Lifshitz-Gilbert equation [76]. Finally, a quite generic linear response solver, implementing among other things the spectral decomposition of the MRFM signal as expressed in Eqs. (11), (12) and (28), has been used to compute the MRFM spectra shown here.

To proceed, the nano-pillar is first discretized using unstructured meshing algorithms resulting in an average mesh size of 3.5 nm. This corresponds to a total number of vertices in the vicinity of 5×10^4. The magnetization vector is interpolated linearly inside each cell (tetrahedra) – a valid approximation taking into account that the cell sizes are smaller than the exchange length $\Lambda_{\text{ex}} \simeq 5$ nm in Permalloy. The magnetic parameters introduced in the code are the ones reported in Table I, and the simulation incorporates the perturbing presence of the magnetic sphere attached on the cantilever. Moreover, the 10 nm thick Cu spacer is replaced by vacuum, so that the layers are only coupled through the dipolar interaction (spin diffusion effects are absent).

The next step is to calculate the equilibrium configuration in the nano-pillar at $H_{\text{ext}} = H_{\text{fix}} = 10$ kOe. The external magnetic field is applied exactly along $\hat{\boldsymbol{z}}$ and the spherical probe with a magnetic moment $m = 2 \times 10^{-10}$ emu is placed on the axial symmetry axis at a distance $s = 1.3$ μm above the upper surface of the nano-pillar. The convergence criterion introduced in the code is $|dM_z/M_j| < 2 \cdot 10^{-9}$ between iterations. The result shown in the inset of FIG. 5 reveals that the equilibrium configuration is almost uniformly saturated along $\hat{\boldsymbol{z}}$. Still, a small tilt ($< 5^\circ$) of the magnetization, away from $\hat{\boldsymbol{z}}$ and along the radial direction, is observed at the periphery of the thick and thin layers.

The micromagnetic eigen solver is then used to compute the lowest eigen-values of the problem as well as the associated eigen-vectors. The discrete list of eigen-values under 18 GHz is shown as black vertical ticks at the bottom of FIGS. 9a and 10a. The precession patterns of the six eigen-vectors corresponding to the six lowest eigen-frequencies are shown in FIG. 11. The middle and right columns show the dynamics $\boldsymbol{m}$ in the thin Py_a and thick Py_b layers, while the precession profiles along the median direction are shown on the left

TABLE II. Comparative table of the resonance values for the SW modes, arranged in order of increasing energy. On the left are the consecutive peak locations measured experimentally. Experiments are performed at f_{fix} = 8.1 GHz (FIG. 2) or H_{fix} = 10 kOe (FIG. 4a). On the right are the simulated eigen-frequencies f at H_{fix} = 10 kOe. The conversion to field value H_{ext} is obtained through $H_{\text{ext}} - H_{\text{fix}} = 2\pi(f - f_{\text{fix}})/\gamma$.

Exp.	f (GHz)	H_{ext} (kOe)	Simu.	f (GHz)	H_{ext} (kOe)
①		10.69	B_{00}	6.08	10.68
❶	7.37	10.22	B_{10}	7.44	10.22
②		9.65	B_{01}	8.95	9.71
③		9.51	A_{00}	9.82	9.42
❷	10.48	9.17	B_{11}	10.47	9.20
❸	10.92	9.07	A_{10}	10.85	9.08
④		8.64	A_{01}	11.98	8.69
❹	13.41	8.22	A_{11}	13.19	8.29

in light and dark colors, respectively. The resonance peaks are labeled according to the SW modes precession profiles and the eigen-values of the simulated peaks are reported in Table II.

From the eigen-vectors spatial patterns, one can compute their coupling (Eq. (11)) to a uniform RF field $\boldsymbol{h}_1 = h_{\text{rf}}\hat{\boldsymbol{x}}$ and, with Eq. (12), the mechanical-FMR spectrum (FIG. 9a). The same procedure is repeated for the RF current-induced Oersted field $\boldsymbol{h}_1 \propto i_{\text{rf}}(-\sin\phi\,\hat{\boldsymbol{x}} + \cos\phi\,\hat{\boldsymbol{y}})$ excitation (FIG. 10a). Since the code gives access to the contribution of each layer, a light (dark) tone is used to indicate the vibration amplitude in the thin (thick) layer in the two figures. For comparison, the mechanical-FMR spectra of FIGS. 2a and 4a have been reported in FIGS. 9b and 10b, respectively. We have applied the same conversion between the frequency (top) and field (bottom) scales as discussed in section III C.

In FIG. 9a, the largest peak in the simulation occurs at the same field as the experimental peak at $H_{①}$. This lowest energy mode corresponds to the most uniform mode with the largest wave-vector and no node along the radial direction, thus it has the index $n = 0$. It has uniform phase along the azimuthal direction, which is the character of the $\ell = 0$ index. For this mode, the thick layer is mainly precessing, with the thin layer oscillating in anti-phase (binding

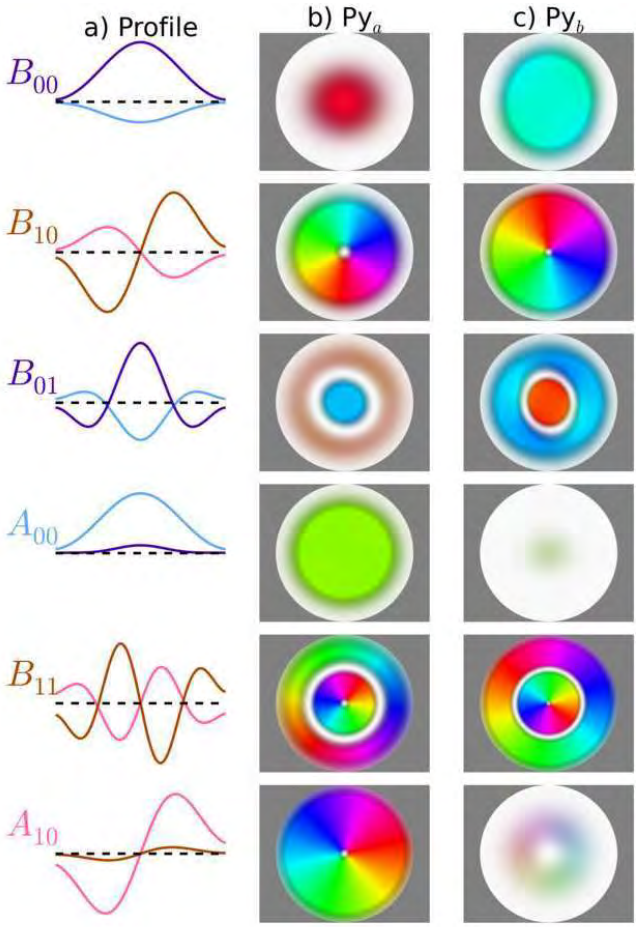

FIG. 11. Simulated precession patterns of the eigen-vectors. Column (a) shows the precession profiles across the thin (light color) and thick (dark color) layers. Columns (b) and (c) show the dynamics in the thin Py$_a$ and thick Py$_b$ layers, respectively, with the color code defined in FIG. 6.

index B), as can be seen from its spatial profile in FIG. 11. The same analysis can be made for the second peak, labeled B_{01}, which occurs close to the peak at $H_②$. It also corresponds to a resonance mainly of the thick layer, and its color representation shows that this is the first radial harmonic ($n = 1$), with one line of nodes in the radial direction. Again, the thin layer is oscillating in anti-phase, with the same radial index $n = 1$, as clearly shown by the mode profile along the median direction. The third peak is labeled A_{00} and is located close to the experimental peak at $H_③$. It corresponds this time to a uniform ($n = 0$) precession mainly located in the thin layer, in agreement with the experimental analysis presented in section III A. In this mode, the thick layer is also vibrating in phase with the thin layer (anti-binding index A).

We can also look at the relative amplitudes of precession in the two disks to quantify the dynamic coupling between the disks. From the profiles shown in FIG. 11, one can infer that for the fundamental mode B_{00}, the amplitude of precession is distributed with a ratio of about 3:1 between the thick (75%) and the thin layer (25%). For the mode A_{00}, the ratio is 8:1 in favor of the thin layer, which contributes to 89% of the precession amplitude (11% for the thick layer). These relative precession amplitudes were expected from the relative weight of the thick and thin layers and from the approximate analytical model presented in section IV B. The simulated field separation between the two coupled uniform modes $(\omega_{B_{00}} - \omega_{A_{00}})/\gamma$ = 1.28 kOe compares also well with the 1.30 kOe estimate from the 2D model, with the dynamic dipolar coupling taken into account. Finally, one can check from the simulations the independence of the precession profiles on the thickness. This confirms the validity of the 2D approximation and explains the performances of the analytical model.

We now briefly comment on the simulated spectrum of FIG. 10, which enables to identify the SW modes excited by the orthoradial Oersted field produced by the RF current flowing through the nano-pillar. From FIGS. 10 and 11, it is clear that the modes which couple to this excitation symmetry have a rotating phase in the azimuthal direction, characteristic of the ℓ = +1 modes [77]. We find that the SW modes of FIG. 10 show the same series of A/B and n indices as those in FIG. 9 (but their ℓ-index is different). This sustains the translational correspondence between the SW spectra of FIGS. 2a and 2b. Finally, we point out that, for all the modes displayed in FIG. 11, the pinning conditions at the boundaries of each disk are not trivial, which we attribute to the collective nature of the motion driven by the dipolar coupling [78]. The general trend observed here is that the thin layer is less pinned than the thick layer for in-phase modes, and vice versa.

To summarize, the 3D micromagnetic simulations enable the identification (with three indices, A/B, ℓ and n) of the SW modes probed experimentally by both a uniform RF magnetic field and an RF current flowing through the nano-pillar, *i.e.*, of their respective selection rules. They confirm the experimental analysis performed in section III and give a deeper insight on the collective nature of the magnetization dynamics in the nano-pillar discussed in section IV B.

V. SYMMETRY BREAKING

In the following, we review some characteristic spectral features associated with the breaking of the axial symmetry in our experiment. First, we experimentally report on the appearance of $\ell = 0$ modes in the SW spectrum excited by an RF current flowing through the nano-pillar, when a small tilt angle is introduced between the applied field and the normal of the layers. This bridges the gap between our mechanical-FMR experiments and usual ST-FMR measurements [25, 26]. Second, we have simulated the spectral distortions introduced by breaking the cylindrical symmetry of the SW confinement potential. This enables to explain the lift of degeneracy in the SW spectrum, which leads to the splitting of modes.

A. Polar angle dependence

The dependence on the polar angle $\theta_H = (\hat{\boldsymbol{z}}, \boldsymbol{H}_{\text{ext}})$ of the mechanical-FMR spectra excited by a uniform RF magnetic field and by an RF current flowing through the nano-pillar is presented in FIG. 12. Let us first focus on the conventional FMR spectra shown in FIG. 12a, acquired at three different polar angles from the exact perpendicularity, increasing by steps of 1°. The main effect here is the shift of the $\ell = 0$ SW modes spectrum towards lower field as θ_H increases, which has been explained in details in Ref.[38] for a single magnetic disk. It is due to the decrease of the demagnetizing field produced by the tilt of the equilibrium magnetization away from the normal. In fact, in each magnetic layer $j = a, b$, the uniform magnetization creates a non-uniform dipolar field $4\pi M_j \widehat{\boldsymbol{G}}^{(d_j)} * \hat{\boldsymbol{u}}_j$, which is maximum in the exact normal configuration. The equilibrium direction $\hat{\boldsymbol{u}}_j$ is in the plane $(\hat{\boldsymbol{z}}, \boldsymbol{H}_{\text{ext}})$ and makes a polar angle $\theta_j > \theta_H$ with the normal determined by Eq. (54). It can be estimated that when $H_{\text{ext}} \approx 10$ kOe and θ_H increases from 0° to 2°, the equilibrium angles θ_a and θ_b of the static magnetization in the thin and thick layers linearly increases from 0° to $\approx 9^\circ$ and from 0° to $\approx 13^\circ$, respectively. This leads to a shift to lower field of the FMR spectrum by about 420 Oe (see Sec. VII B), in agreement with the data. We also emphasize that, in fact, the profiles of the SW eigen-modes are affected by the breaking of axial symmetry, and that the pure $\ell = 0$ eigen-modes when $\theta_H = 0$ become mixed with $\ell \neq 0$ modes [38] when $\theta_H \neq 0$.

We now turn to the influence of the polar angle θ_H on the FMR spectra excited by an RF current ($i_{\text{rf}} = 170$ μA). The same global shift towards lower field as discussed above is

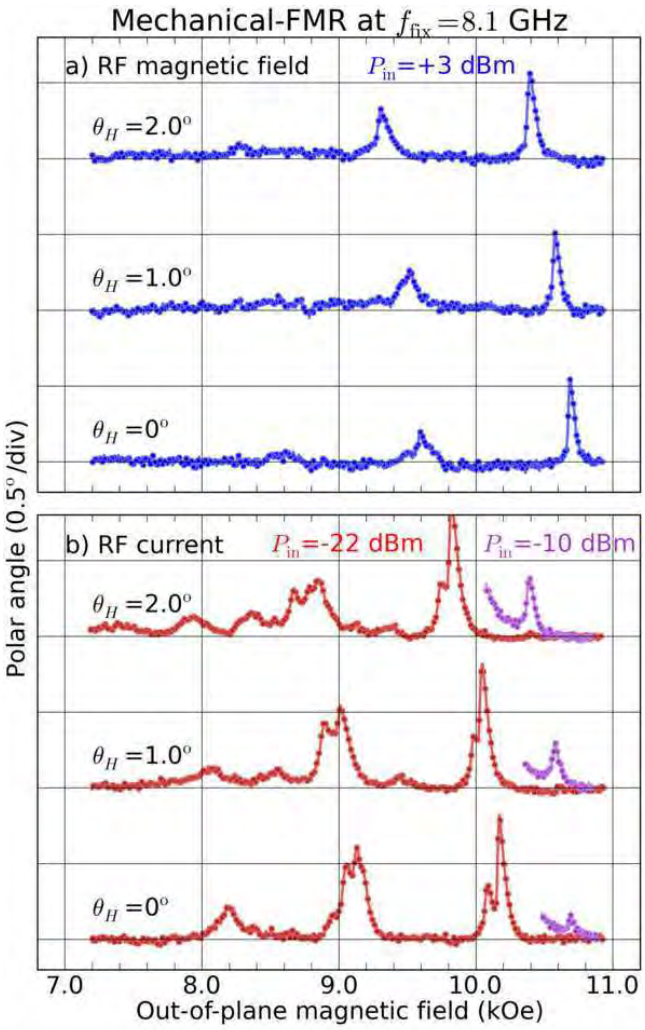

FIG. 12. Dependence of the mechanical-FMR spectra excited by a uniform RF magnetic field (a) and by an RF current flowing through the nano-pillar (b) on the polar angle θ_H between the applied field and the normal to the layers. Superposed (in purple) is the behavior of the high field tail at larger power.

observed in FIG. 12b by looking at the red spectra acquired with an increasing θ_H. But there is an important additional effect here. Whereas only ℓ = +1 SW modes are excited by the RF current flowing through the nano-pillar in the exact perpendicular geometry, resonance peaks can also be detected at the positions of ℓ = 0 SW modes when $\theta_H \neq 0$. Although the amplitudes of the ℓ = 0 modes are not large in FIG. 12b, it is quite clear that they all grow as θ_H increases. In order to reveal this effect better, we have reported in purple on the same figure the resonance peak of the mode B_{00} excited with a +12 dB larger power

($i_{\rm rf} \simeq 680$ μA), as a function of θ_H. Despite the large RF current excitation, its amplitude almost vanishes at $\theta_H = 0$. Then, it increases linearly with θ_H, until it becomes almost as large as when it is excited by the uniform RF field $h_{\rm rf} \simeq 2.1$ Oe used in FIG. 12a.

The experimental data and their analysis presented in the previous sections II to IV demonstrate that in the exact perpendicular configuration, only $\ell = +1$ modes are excited by the RF current flowing through the nano-pillar, due to the orthoradial symmetry of the induced RF Oersted field, Eq. (34). Because there is no overlap between this particular excitation symmetry and the uniform azimuthal symmetry of the $\ell = 0$ modes, the latter do not couple to the RF current excitation. The fact that these hidden modes in the exact perpendicular configuration can be excited by introducing a small misalignment angle between the applied field and the normal to the nano-pillar $\hat{\boldsymbol{z}}$ is a striking result. It means that the selection rules associated to the RF current excitation change if the applied field is tilted away from $\hat{\boldsymbol{z}}$, what we shall now explain.

Due to the smaller demagnetizing field in the thin magnetic disk than in the thick one (due to $M_a < M_b$), the equilibrium angle of the thin layer is smaller than in the thick layer, $\theta_a < \theta_b$, as obtained from Eq. (54). For the parameters of our nano-pillar, $\beta = \theta_b - \theta_a \approx 2\theta_H$, at $H_{\rm ext} \approx 10$ kOe and for a small angle θ_H. It means that if $\theta_H \neq 0$, the magnetization vectors in both layers are misaligned from each other by an angle $\beta = (\boldsymbol{M}_a, \boldsymbol{M}_b)$, so that the cross product $\hat{\boldsymbol{u}}_a \times \hat{\boldsymbol{u}}_b$ is finite and lies in the plane parallel to the layers, say along $\hat{\boldsymbol{x}}$. Thus, the spin transfer excitation $(2\pi\lambda)^{-1} i_{\rm rf} \sin\beta \hat{\boldsymbol{x}}$ associated to the RF current flowing through the spin-valve nano-pillar [25, 26], which is vanishing in the exact perpendicular configuration where $\beta = 0$, becomes finite if there is a small misalignment angle $\theta_H \neq 0$ (see Eqs. (35) and (36) in Sec. VII A, $(2\pi\lambda)^{-1}$ is the spin transfer efficiency). Because this so-called ST-FMR excitation has the same symmetry as an in-plane uniform RF magnetic field, it is expected to excite SW modes having the $\ell = 0$-index symmetry. Still, this excitation has to compete with the RF Oersted field excitation, which is independent of θ_H and is much larger in our configuration due to the small value of β ($< 5°$). Therefore the amplitudes of the $\ell = +1$ modes are much larger than those of the $\ell = 0$ modes in FIG. 12b.

It is also clear that the amplitude of the mode B_{00} excited by the RF current (purple peaks in FIG. 12b) grows linearly with θ_H, as expected from the above discussion. We emphasize that a quantitative understanding of the amplitude of the peaks excited by ST-FMR would require to consider the collective nature of the dynamics in the nano-pillar and

the asymmetry of spin transfer in the thick and thin magnetic layers. Finally, we note that the small signal observed at $\theta_H = 0$ should in principle vanish with the ST-FMR excitation. This reminiscent signal can be ascribed to a small misalignment of the applied field with respect to the normal to the nano-pillar (the precision on the orientation is 0.2°) or to a slight asymmetry of the RF current lines through the nano-pillar, which would induce a small asymmetry of the RF Oersted field, thereof adding a small in-plane uniform component to the orthoradial magnetic field.

To summarize, this study enables to derive the selection rules of the RF current excitation. In the exact perpendicular configuration, the magnetizations of both layers are aligned, and only $\ell = +1$ modes can be excited due to the orthoradial symmetry of the current-created Oersted field ($\ell = 0$ modes are hidden). But when a finite angle is introduced between the magnetizations in each layer by slightly tilting the applied field away from the normal, $\ell = 0$ modes can be excited by ST-FMR, which has the same symmetry as a uniform RF field excitation polarized in-plane.

B. Confinement asymmetries

As seen in section IV C, the 3D micromagnetic simulations enable to identify the SW modes observed in the experimental spectra. Still, the latter are more rich than the simulated power spectra, due to the splitting of some resonance peaks, which was noted in sections II C and III A. In particular, the experimental peak at $H_{❶}$, identified as the mode B_{10}, is clearly split in two, with a smaller resonance about 100 Oe away in the low field wing of the main peak, which is not the case in the simulation (see FIG. 10). The peaks at $H_{❷}$ (identified as B_{11}) and at $H_{❸}$ (A_{10}) are also split, contrary to the simulations, where all these peaks are single. In contrast to these observations, the peak at $H_{①}$, which is the uniform mode B_{00}, is single both in the experimental and simulated spectra.

So, it seems that experimentally, the occurrence of the mode splitting depends on the mode index, whereas in 3D simulations, in which the nano-pillar has a perfect cylindrical shape, none of the resonance peaks is split. This suggests that the observed splittings are related to asymmetries in the confinement of the disks, and that the various SW modes are affected differently because they probe different regions. The fact that the double peak at $H_{❶}$ depends on the tilt angle (see FIG. 12b) and is more or less pronounced depending on

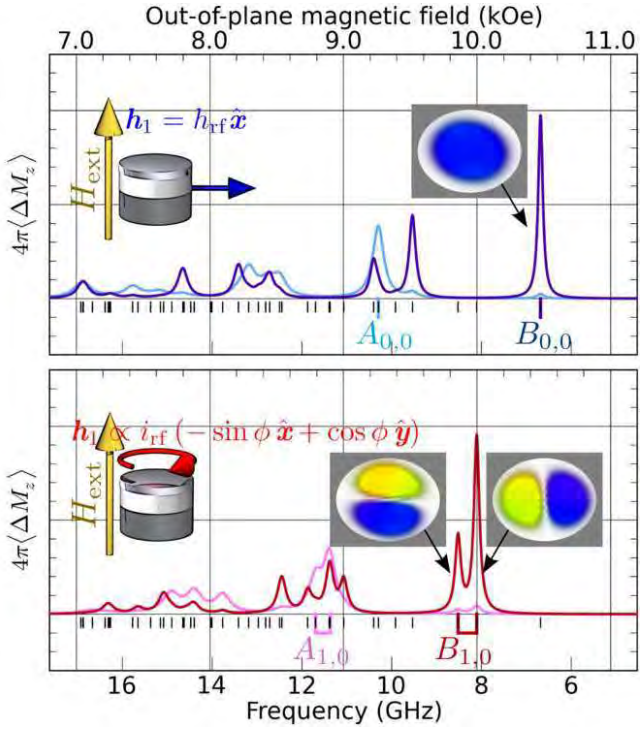

FIG. 13. Simulated SW spectra for a nano-pillar with an elliptical section (see text). Linear response to a homogeneous RF magnetic field excitation (a) and to an orthoradial RF Oersted field excitation (b). The precession patterns of the lowest energy modes are shown in the insets.

the direction in which the applied field is tilted from the normal (not shown) is another strong indication that some symmetry breaking in the lateral confinement is at the origin of this effect [79].

To support this idea, we have carried out new 3D micromagnetic simulations with the SpinFlow 3D package on a structure that break the perfect cylindrical symmetry of the nano-pillar. We have kept a perfectly flat structure, but we have used an elliptical cross-section. The long axis of the ellipse is 250 nm, while the short axis is 200 nm. The influence of this breaking of symmetry on respectively the ℓ = 0 spectrum (RF field excitation) and the ℓ = +1 spectrum (RF current excitation) is presented in FIG. 13.

Concentrating first on the standard FMR SW spectrum of FIG. 13a, one can see that the lowest energy mode B_{00} remains a single peak. This illustrates the intuitive idea that the uniform SW mode, where the oscillation power is mostly concentrated at the center, is rather not sensitive to change of the confinement at the periphery. The same behavior applies for the lowest energy mode of the thin layer, A_{00}.

The simulated SW spectrum of FIG. 13b shows a different sensitivity to the shape asymmetry. It is observed that the lowest energy mode with the $\ell = +1$-index splits in two peaks, in contrast with the lowest energy $\ell = 0$ mode which remains a single peak. We also note that the satellite peak, induced by the elliptical confinement, is located in the low field wing of the main resonance, as in the experiments of FIG. 2b. The precession patterns shown in the two insets FIG. 13b reveal that the elliptical shape introduces some mixing between the $\ell = +1$ and $\ell = -1$ SW modes (the $\ell = -1$ mode corresponds to SWs that are rotating around the disk in the opposite direction as the Larmor precession). In a circular disk, these two modes are degenerate, and only the $\ell = +1$ mode couple to the orthoradial Oersted field excitation. But in the ellipse, the two eigen-modes split and become mixed, as shown by the two eigen-vectors displayed in FIG. 13b, which correspond to the linear combinations $J_1(\rho) + J_{-1}(\rho)$ and $J_1(\rho) - J_{-1}(\rho)$. The simulated spectrum of FIG. 13b reproduces well the main features of the mechanical-FMR spectrum of FIG. 2b, including the splittings observed for the $\ell = +1$ SW modes (revealed even better by injecting a dc current through the nano-pillar, see FIG. 3b). Thus, a small elliptical shape produced during the nanostructuration of the nano-pillar is most likely responsible for the double peak observed at $H_{\bullet}$ in FIG. 2b.

To summarize, the comparison between 3D simulations and experiments demonstrate that the observed mode splittings originates from a small asymmetry in the lateral confinement of the nano-pillar.

VI. CONCLUSION

In summary, we used the MRFM technique [38] to study the SW eigen-modes in the prototype of a STNO - a normally magnetized nano-pillar composed of two magnetic layers coupled by dipolar interaction.

In contrast to transport spectroscopy techniques [22, 25], MRFM is sensitive to all SW modes excited in the sample [39] and is completely independent of the transport properties of the studied spin-valve sample. Therefore, MRFM provides an alternative and complementary view on the magnetization dynamics in hybrid magnetic nano-structures. The additional advantages of the MRFM technique are its high sensitivity (in this study, it was able to detect angles of precession as low as 1° in the thin magnetic layer) and its ability to operate on standard STNO devices buried under contact electrodes without a specific probe

access to the studied sample [43].

Using MRFM, we were able to compare the SW spectra of a passive perpendicularly magnetized STNO-like sample excited by a uniform in-plane RF magnetic field and by an RF current flowing perpendicularly through the layers. We found that distinctly different SW modes (having azimuthal indices ℓ = 0 and ℓ = +1, respectively) are excited by the two above mentioned excitation methods. By studying the influence of a spin polarized dc current on the observed SW spectra we were able to determine which of the magnetic layers of the studied nanopillar plays the dominant role in the magnetization dynamics resulting in the appearance of each particular SW mode.

We also developed a simple analytic theory allowing to perform a comprehensive labeling of all the SW eigen-modes of a magnetic nanopillar in the studied axially symmetric case. This labeling requires three independent indices: the usual azimuthal and radial indices ℓ and n used for the SW modes of a single magnetic disk and an additional index referring to the binding or anti-binding (B or A) coupling between the two magnetic disks forming a nanopillar. The obtained experimental and analytic results were also compared to the results of 3D micromagnetic simulations obtained with the SpinFlow 3D package [72], which confirmed the mode labeling obtained from the analytic theory.

Thus, we learned that in the axially symmetric case of a perpendicularly magnetized nano-pillar, the excitations by the RF field the RF current lead to two mutually orthogonal (and mutually exclusive) sets of excited SW modes: only the ℓ = 0 modes are excited by the uniform RF magnetic field, while only the ℓ = +1 modes are excited by the RF current. Therefore, the ℓ-index, related to the azimuthal symmetry of the SW modes, is the discriminating parameter for the selection rules of the SW mode excitation.

Moreover, we have demonstrated experimentally and numerically that the mode selection rules are affected by the breaking of the axial symmetry of the studied nano-pillar, either by tilting the bias magnetic field or by making the sample cross-section elliptical. In particular, if the axial symmetry is broken by tilting the bias magnetic field, the ℓ = 0 modes can also be excited by an RF current. This excitation is caused by the ST-FMR mechanism working when the magnetization vectors in the two magnetic layers of the nano-pillar are not collinear. Also, the importance of the dynamic dipolar interaction between the magnetic layers of the nano-pillar have been clearly demonstrated by our results.

We believe that our results are important for the optimization of the characteristics of

nano-spintronic devices, and in particular STNOs, and for the experimental determination of the STNO parameters.

First of all, an accurate identification of the SW modes that can be excited in an STNO nano-pillar is necessary to understand the details of the high frequency STNO dynamics. The proposed identification of the nano-pillar SW modes can be used for the experimental determination of the nano-pillar characteristics, such as radius, static magnetization, gyromagnetic ratio, and dissipation. We note that in traditional STNO experiments, where the magnetization dynamics in a magnetic nano-pillar is excited by a spin-polarized bias current creating a significant Oersted magnetic field with the $\ell = +1$ symmetry, it is easy to mix-up the $\ell = 0$ and the $\ell = +1$ SW eigen-modes. The spectra of these modes are in almost translational correspondence, and the experimentally observed dependence of the mode frequencies on the bias magnetic field can be well described by the traditional Kittel expression (see *e.g.* [11]). Thus, the possibly excited $\ell = +1$ mode can be easily interpreted as a $\ell = 0$ mode, which will lead to the apparent reduction of the "free" layer static magnetization necessary to fit the Kittel expression for the mode frequency. For instance, mislabeling the lowest energy mode of the $\ell = +1$ SW spectrum as the uniform mode $(\ell, n = 0, 0)$ combined with a small misalignment of the applied field would lead to a discrepancy as large as 1 kG in our case.

Second, the fact that in most cases both magnetic layers of a nano-pillar take part in current-induced magnetization dynamics is very important for the correct identification of the excited SW modes. The collective (coupled) character of the SW modes in a nano-pillar can directly influence the magnitude of the spin transfer torque, which is dependent on the relative orientation of the magnetization vectors in the two magnetic layers. One might expect, that the efficiency of the spin transfer torque for a particular SW mode depends not only on which layer ("free" or "fixed") is dominating the mode dynamics, but also on the coupling (in phase or anti-phase) between the magnetization precession in two layers. In our experimental case, the interlayer coupling is in-phase for the SW modes dominated by the dynamics in a "free" (thin) layer. To obtain an interlayer coupling which is anti-phase for the SW modes dominated by the dynamics of the thin layer would require for example to increase its magnetization compared to the "fixed" layer one.

Finally, it is important to note that the MRFM technique has allowed us to study spin transfer effects in the axially symmetric configuration of a perpendicularly magnetized nano-

pillar, where the excitation of magnetization dynamics by ST-FMR vanishes due to the symmetry reasons. This geometry is rather important for applications as the excited SW modes have the maximum non-linear frequency shift coefficient [19]. This creates the maximum agility of the mode frequency with the bias current and, therefore, the maximum width of the synchronization band to the external periodic signal and to the large arrays of other STNOs [19]. Phase synchronization has been identified as a possible mean to dramatically increase the generated microwave power of these nano-oscillators and, at the same time, reduce their linewidth [80–87].

VII. APPENDIX A: THEORETICAL MATERIAL

A. Equation of motion

In this appendix, we detail the derivation of the equations which govern the dynamics of a ferromagnetic layer in the presence of an external periodic excitation and of spin transfer, following the general formalism introduced in section IV A 1. For an isolated layer, the *local* dynamics (within the exchange length) of the magnetization vector is described by the Landau-Lifshitz (LL) equation:

$$\frac{1}{\gamma}\frac{\partial \boldsymbol{M}}{\partial t} = \boldsymbol{H} \times \boldsymbol{M} + \boldsymbol{h}(t) \times \boldsymbol{M} \,, \tag{21}$$

with γ being the modulus of the gyromagnetic ratio. The LL equation is written here in its perturbative form, where the second term on the right-hand-side of Eq. (21) represents the perturbation term. The field $\boldsymbol{H}$ is the effective magnetic field:

$$\boldsymbol{H} = \boldsymbol{H}_0 - 4\pi \widehat{\boldsymbol{G}} * \boldsymbol{M} \ . \tag{22}$$

Here, $\boldsymbol{H}_0$ is the total static external magnetic field (possibly spatially-dependent) and the linear tensor self-adjoint operator $\widehat{\boldsymbol{G}}$ describes the magnetic self-interactions.

Considering only the linear processes, we can represent the time dependent (out-of-equilibrium) part of the magnetization as a series over the SW eigen-modes:

$$\begin{aligned} \boldsymbol{M}(t,\boldsymbol{r}) - M_s \hat{\boldsymbol{u}}(\boldsymbol{r}) &\approx \boldsymbol{m}(t,\boldsymbol{r}) \\ &\approx \sum_{\nu} c_\nu(t) \boldsymbol{m}_\nu(\boldsymbol{r}) + \text{c.c.} \,, \end{aligned} \tag{23}$$

where M_s is the saturation magnetization of the layer. Here, c.c. stands for the complex-conjugated part. The coefficients $c_\nu(t)$ are time-dependent SW amplitudes.

The second term on the left-hand-side of Eq. (21) represents the perturbations from the equilibrium state, including the non-adiabatic contributions. The non-conservative perturbation magnetic field $\boldsymbol{h}(t)$ may depend on time and be a function of the magnetization distribution $\boldsymbol{M}(t)$. It can be approximately represented as:

$$\boldsymbol{h}(t) = \boldsymbol{h}_1(t) + \widehat{\boldsymbol{L}}_1 * \boldsymbol{m}(t)\,, \tag{24}$$

where $\boldsymbol{h}_1(t)$ is the external perturbation field and $\widehat{\boldsymbol{L}}_1$ is a certain linear operator, allowing $\boldsymbol{h}(t)$ to depend on the magnetization distribution. The latter case may describe the influence of the Gilbert damping $-(\alpha/\gamma M_s)\partial\boldsymbol{M}/\partial t$ through:

$$\widehat{\boldsymbol{L}}_1 * \boldsymbol{m} = i\frac{\alpha}{\gamma}\sum_\nu \omega_\nu (c_\nu(t)\boldsymbol{m}_\nu(\boldsymbol{r}) - \text{c.c.})\,, \tag{25}$$

where α is the Gilbert damping constant.

Substituting the series representation Eq. (23) and the representation of the perturbation field Eq. (24) into Eq. (21) and using orthogonality relations Eq. (7), one can obtain the following equations for the SW amplitudes c_ν:

$$\frac{dc_\nu}{dt} = -i\omega_\nu c_\nu + i\gamma\sum_{\nu'}\left(S_{\nu,\nu'}c_{\nu'} + S_{\nu,\overline{\nu'}}\overline{c}_{\nu'}\right) + i\gamma h_\nu\,, \tag{26}$$

where

$$S_{\nu,\nu'} = \frac{\left\langle \overline{\boldsymbol{m}}_\nu \cdot \widehat{\boldsymbol{L}}_1 * \boldsymbol{m}_{\nu'}\right\rangle - \left\langle (\hat{\boldsymbol{u}}\cdot\boldsymbol{h}_1)(\overline{\boldsymbol{m}}_\nu\cdot\boldsymbol{m}_{\nu'})\right\rangle}{\mathcal{N}_\nu}\,, \tag{27a}$$

$$S_{\nu,\overline{\nu'}} = \frac{\left\langle \overline{\boldsymbol{m}}_\nu \cdot \widehat{\boldsymbol{L}}_1 * \overline{\boldsymbol{m}}_{\nu'}\right\rangle - \left\langle (\hat{\boldsymbol{u}}\cdot\boldsymbol{h}_1)(\overline{\boldsymbol{m}}_\nu\cdot\overline{\boldsymbol{m}}_{\nu'})\right\rangle}{\mathcal{N}_\nu}\,, \tag{27b}$$

$$h_\nu = \frac{\langle \overline{\boldsymbol{m}}_\nu \cdot \boldsymbol{h}_1\rangle}{\mathcal{N}_\nu}\,. \tag{27c}$$

In many cases the perturbed equations (26) can be further simplified by retaining only the diagonal term $S_{\nu,\nu} = i\alpha\omega_\nu\langle\overline{\boldsymbol{m}}_\nu\cdot\boldsymbol{m}_\nu\rangle/(\gamma\mathcal{N}_\nu)$ (assuming that there are no degenerate modes). The SW damping rate is then given by

$$\Gamma_\nu = \alpha\omega_\nu\frac{\langle\overline{\boldsymbol{m}}_\nu\cdot\boldsymbol{m}_\nu\rangle}{\mathcal{N}_\nu}\,. \tag{28}$$

The damping rate Γ_ν is responsible for the finite linewidth of the resonance peaks, ΔH (FWHM). If the sample is homogeneously magnetized and the precession is circular, the simple relation $\alpha\Delta H = \omega_\nu/\gamma$ holds.

From the equations above, one recovers for the coefficient c_ν the equation of motion of a damped harmonic oscillator:

$$\frac{dc_\nu}{dt} = -i\omega_\nu c_\nu - \Gamma_\nu c_\nu + i\gamma h_\nu \,. \tag{29}$$

If a second magnetic layer j' is electrically connected to layer j and spin transfer is allowed between them, the equation of motion must be modified. When a charge current I is flowing through the layers, the additional Slonczewski-Berger term [6, 7] adds to the operator $\widehat{\boldsymbol{L}}_1$ of Eq. (24). It is possible to define an effective damping in layer j, which depends on the spin polarized current and on the relative angle between the magnetization in layer j and the direction of the spin polarization $\hat{\boldsymbol{u}}_{j'}$ [19]:

$$\Gamma_\nu^* = \alpha\omega_\nu \frac{\langle \overline{\boldsymbol{m}}_\nu \cdot \boldsymbol{m}_\nu \rangle}{\mathcal{N}_\nu} + \frac{I\epsilon}{2eN_s} \frac{\langle (\overline{\boldsymbol{m}}_\nu \cdot \boldsymbol{m}_\nu)(\hat{\boldsymbol{u}}_j \cdot \hat{\boldsymbol{u}}_{j'}) \rangle}{\mathcal{N}_\nu} \,, \tag{30}$$

where

$$N_s = \frac{M_j V_j}{\gamma\hbar} \tag{31}$$

is the dimensionless total number of magnons that can be excited inside the volume V_j of layer j. Here, $\hbar$ is the reduced Planck constant, e the modulus of the electron charge and ϵ the spin polarization efficiency of the current. The threshold current for auto-oscillations in layer j corresponds to $\Gamma_\nu^* = 0$, *i.e.*, if $\hat{\boldsymbol{u}}_j \parallel \hat{\boldsymbol{u}}'_j$, $I_{\rm th} = -2\alpha\omega_\nu N_s e/\epsilon$. Using $\epsilon = 0.3$ and the parameters of our thin layer, one can estimate $I_{\rm th} \simeq -4.8$ mA for the uniform SW mode at 8.1 GHz, in agreement with the experimental data [88]. This result is also in quantitative agreement with calculations performed for our nano-pillar device with no adjusting parameters in the framework of continuous random matrix theory (CRMT) described in Ref.[89].

We now turn to the periodic external excitation $\boldsymbol{h}_1(t) = \boldsymbol{h}_1 \exp^{i\omega t}$, whose amplitude $\boldsymbol{h}_1$ is composed of three different contributions,

$$\boldsymbol{h}_1 = \boldsymbol{h}_{\rm u} + \boldsymbol{h}_{\rm Oe} + \boldsymbol{h}_{\rm ST} \,, \tag{32}$$

that we shall detail below.

The first type of excitation corresponds to a uniform RF magnetic field applied perpendicularly to the effective field $\boldsymbol{H}$. This configuration corresponds to conventional FMR

spectroscopy. Assuming that the sample is uniformly magnetized along the nano-pillar symmetry axis $\hat{\boldsymbol{z}}$, it reduces to:

$$\boldsymbol{h}_{\mathrm{u}} = h_{\mathrm{rf}}\hat{\boldsymbol{x}}, \tag{33}$$

where $\hat{\boldsymbol{x}}$ is a unit vector in the in-plane direction and h_{rf} the linearly polarized amplitude.

SW spectroscopy can also be performed by injecting a uniform RF charge current i_{rf} through the nano-pillar (*i.e.*, along $\hat{\boldsymbol{z}}$). First, this produces an orthoradial RF Oersted field:

$$\boldsymbol{h}_{\mathrm{Oe}} = \left[\frac{4\pi}{10}\right]\frac{i_{\mathrm{rf}}}{2\pi R}\frac{\rho}{R}\left(-\sin\phi\,\hat{\boldsymbol{x}} + \cos\phi\,\hat{\boldsymbol{y}}\right), \tag{34}$$

where R is the radius of the nano-pillar and (ρ, ϕ) are the polar coordinates. In this formula, the current should be expressed in A and the prefactor between the square brackets converts A/cm into Oe (cgs units). The maximum amplitude of the RF Oersted field is reached at the periphery of the nano-pillar, $\rho = R$, and equals 1.6 Oe for a peak amplitude $i_{\mathrm{rf}} = 100$ μA and the experimental parameters.

Second, the RF current produces a ST-FMR excitation:

$$\boldsymbol{h}_{\mathrm{ST}} = \frac{i_{\mathrm{rf}}}{2\pi\lambda}\left[\hat{\boldsymbol{u}}_j \times \hat{\boldsymbol{u}}_{j'}\right]. \tag{35}$$

where we have rewritten the spin-transfer efficiency of the charge current in Eq. (30) as a function of

$$2\pi\lambda = \gamma\frac{2eN_s}{\epsilon}, \tag{36}$$

which has the dimension of a distance ($\lambda \simeq 200$ nm for our thin layer). If the thin and thick layers are misaligned by an angle β in the plane (y,z), Eq. (35) reduces to $\boldsymbol{h}_{\mathrm{ST}} = i_{\mathrm{rf}}/(2\pi\lambda)\sin\beta\hat{\boldsymbol{x}}$, which demonstrates that the ST-FMR excitation is equivalent to a linearly polarized RF magnetic field, Eq. (33). The ST-FMR excitation vanishes if the magnetic layers are parallel. The amplitude ratio between the ST-FMR and the RF Oersted field excitations, both produced by the RF current flowing through the nano-pillar, is $h_{\mathrm{ST}}/h_{\mathrm{Oe}} \simeq (R/\lambda)\sin\beta$. In our geometry, $\lambda \approx 2\,R$, but due to the small angle β between the layers, the RF Oersted field contribution is much larger than the ST-FMR one. We note that even if $\beta \approx \pi/2$, the contribution of the RF Oersted field cannot be disregarded in general in ST-FMR experiments.

B. Numerical application

In this section, we derive a practical guideline to calculate the eigen-frequencies ω using the analytical formalism developed in section IV A. Let $\boldsymbol{m}_\nu$ be a certain orthogonal basis in the space of the vector functions $\boldsymbol{m}$ satisfying both the local orthogonality to $\hat{\boldsymbol{u}}$ and the total pinning condition at the boundary of the magnetic body. Spin-wave eigen modes can thus be expressed as a series expansion on the $\boldsymbol{m}_\nu$ basis (cf. Eq. (23)). A general expression for the eigen-frequencies can be found from the condition of vanishing determinant:

$$\left\| \mathcal{N}_{\nu',\nu}\omega - \mathcal{N}_{\nu',\nu} \left\{ \widehat{\Omega} \right\}_{\nu',\nu} \right\| = 0 \ , \tag{37}$$

where for the simplicity of the discussion, it is convenient to introduce a curly bracket notation, to indicate that the enclosed quantity is spatially weighted by the spatial pattern of the mode profile and averaged:

$$\left\{ \widehat{\Omega} \right\}_{\nu',\nu} \equiv \frac{\left\langle \overline{\boldsymbol{m}}_{\nu'} \cdot \widehat{\Omega} * \boldsymbol{m}_\nu \right\rangle}{\mathcal{N}_{\nu',\nu}} \ , \tag{38}$$

This echoes the chevron bracket notation introduced in Eq. (1) to indicate the homogeneous spatial average over the volume of the magnetic body. Here $\mathcal{N}$ represents a renormalization quantity, defined by

$$\mathcal{N}_{\nu',\nu} \equiv i \left\langle \overline{\boldsymbol{m}}_{\nu'} \cdot (\hat{\boldsymbol{u}} \times \boldsymbol{m}_\nu) \right\rangle \ , \tag{39}$$

which has in general off-diagonal elements.

In the case of perpendicularly magnetized disks, where the set of Bessel functions $\frac{1}{2}(\hat{\boldsymbol{x}} + i\hat{\boldsymbol{y}})e^{-i\ell\phi}J_\ell(k_{\ell,n}\rho)$ diagonalizes the uncoupled Hamiltonian, the secular Eq. (37) becomes diagonal and we recover Eq. (8):

$$\omega_\nu = \left\{ \widehat{\Omega} \right\}_{\nu,\nu} \tag{40}$$

We shall now perform the numerical application of the eigen-value of the lowest energy mode $(\ell, n = 0, 0)$ using the parameters of our nano-pillar shown in Table I. We will drop the subscript ν to the curly brackets, understanding that the spatial average in Eq. (40) is made over the uniform mode $\boldsymbol{m}_\nu = \frac{1}{2}J_0(k_0\rho)(\hat{\boldsymbol{x}} + i\hat{\boldsymbol{y}})$, where $k_0 = 2.4048/R$ is its wave-vector. In this case the value of the normalization constant is simply $\mathcal{N}_0 = \langle J_0^2 \rangle = J_1^2(k_0 R) = 0.2695$.

The different contributions that enter inside the operator $\left\{ \widehat{\Omega} \right\}$ are detailed in Eq. (4):

$$\left\{ \widehat{\Omega} \right\} = \gamma \left\{ H \right\} + 4\pi\gamma M_j \left\{ \widehat{\boldsymbol{G}} \right\} \ . \tag{41}$$

We start with the calculation of the amplitude of effective magnetic field, the first term on the right hand side of Eq. (41). As shown by Eq. (5), the scalar value H along $\hat{\boldsymbol{z}}$ decomposes itself in two terms:

$$\{H\} = \{\hat{\boldsymbol{z}} \cdot \boldsymbol{H}_0\} - 4\pi M_s \left\{\hat{\boldsymbol{z}} \cdot \widehat{\boldsymbol{G}} * \hat{\boldsymbol{z}}\right\}. \tag{42}$$

The term $\hat{\boldsymbol{z}} \cdot \widehat{\boldsymbol{G}} * \hat{\boldsymbol{z}}$ represents the static magnetic self-interaction. In the case of homogeneously magnetized body, the inhomogeneous exchange contribution to the static self-interaction is strictly null and the second term of Eq. (42) reduces to the magneto-dipolar contribution $\widehat{\boldsymbol{G}}^{(d)}$, which has the following form in the wave-vector representation:

$$\widehat{\boldsymbol{G}}^{(d)}(\boldsymbol{r}) = \int D(\boldsymbol{k}) \frac{\boldsymbol{k} \otimes \boldsymbol{k}}{k^2} \exp^{i\boldsymbol{k}\cdot\boldsymbol{r}} d^3\boldsymbol{k}\,, \tag{43}$$

where $D(\boldsymbol{k})$ is the Fourier transform of the body shape function [90] and the symbol $\otimes$ denotes direct product of vectors. For a disk of radius R and thickness t, an analytical expression for the different position-dependent demagnetization tensor elements of a disk $N_{uv\,[R,t]}(\boldsymbol{r}) \equiv \hat{\boldsymbol{u}}(\boldsymbol{r}) \cdot \widehat{\boldsymbol{G}}^{(d)} * \hat{\boldsymbol{v}}$ valid in the whole space are available in Ref.[91]. For perpendicularly magnetized disks where $\hat{\boldsymbol{u}} = \hat{\boldsymbol{v}} = \hat{\boldsymbol{z}}$, the expression of the self-integral becomes

$$\left\{N_{zz}^{(j,j)}\right\} = \frac{1}{\langle J_0^2 \rangle} \int_{V_j} d^2\rho dz\; J_0^2(k_0\rho) N_{zz\,[R,t_j]}(\rho, z)\,, \tag{44}$$

for both the thin ($j = a$) and thick ($j = b$) layers. Their numerical values are displayed in Table. III.

The term $\{\hat{\boldsymbol{z}} \cdot \boldsymbol{H}_0\}$ of Eq. (42) is the projection on the precession axis of the total applied magnetic field. It comprises the external magnetic field $\{H_{\rm ext}\} = H_{\rm ext}$, the stray field of the mechanical-FMR probe $\{H_{\rm sph}\} = 190$ Oe and the cross-magneto-dipolar static interactions between each layer. The latter can be estimated from the cross tensor elements of the static magneto-dipolar field of the j'-th disk produced over the volume of the j-th disks:

$$\left\{N_{zz}^{(j,j')}\right\} = \frac{1}{\langle J_0^2 \rangle} \int_{V_j} d^2\rho dz\; J_0^2(k_0\rho) N_{zz\,[R,t_{j'}]}(\rho, z + z_0)\,, \tag{45}$$

where z_0 is the distance between the centers of the two axially aligned disks. The numerical values of the cross tensor elements are reported in Table. III. Putting all the above elements together, the total effective field simply writes:

$$\{H\} = H_{\rm ext} + \{H_{\rm sph}\} - 4\pi \left\{N_{zz}^{(j,j)}\right\} M_j - 4\pi \left\{N_{zz}^{(j,j')}\right\} M_{j'}\,. \tag{46}$$

We now turn our attention to the integration $4\pi M_j \left\{\widehat{\boldsymbol{G}}\right\}$, the second term on the right hand side of Eq. (41). We recall that for Py the operator $\widehat{\boldsymbol{G}} = \widehat{\boldsymbol{G}}^{(e)} + \widehat{\boldsymbol{G}}^{(d)}$ is the sum of the inhomogeneous exchange and magneto-dipolar interactions. In the wave-vector representation, $\widehat{\boldsymbol{G}}^{(e)} = \Lambda_{\rm ex}^2 k^2 \widehat{\boldsymbol{I}}$, where the exchange length $\Lambda_{\rm ex} = \sqrt{2J/(4\pi M_j^2)}$ depends on the exchange stiffness constant J, expressed in erg/cm (= 10^{-6} in Py). It produces the exchange field:

$$\{H_{\rm ex}\} = 4\pi M_j \Lambda_{\rm ex}^2 k_0^2 \ , \tag{47}$$

which yields the value $\{H_{\rm ex}\} = 110$ Oe.

The other contribution is the dynamic magneto-dipolar self-interaction, which represents the depolarization field of the SW mode on itself. For the $\ell = 0$ modes, an analytical expression can be derived:

$$\left\{N_{xx}^{(j,j')}\right\} = \frac{1}{\langle J_0^2 \rangle} \int_{V_j} d^2\rho dz \ J_0(k_0\rho) \int_0^R du \frac{\partial N_{xx\,[u,t_{j'}]}(\rho,z)}{\partial u} J_0(k_0 u) \, , \tag{48}$$

where the quantity in the second integral is the magnetic stray field produced at the spatial position $\boldsymbol{r}$ by a cylindrical tube of width du, radius u, and thickness $t_{j'}$, homogeneously magnetized [92] along $\hat{\boldsymbol{x}}$ by $J_0(k_0 u)$. We use the same expression above to write the self- and cross-contribution, understanding implicitly that the spacer value z_0 should be added in the later case, as shown in Eq. (45). The values of the self- and cross-tensor elements are reported in the last line of Table. III. We mention, that an approximate expression of the self-Eq. (48) has been derived by Kalinikos and Slavin [93] for the lowest SW branch of platelet shape bodies with uniform magnetization across the film thickness. This expression reduces to

$$\{N_{xx}\} \simeq \frac{1}{2}\left(1 - G_0^{\perp}\right) \tag{49}$$

where the analytical expression of $G_{\ell,n}^{\perp}$ for Bessel functions is given by Eq. (26) in ref[38].

The cross elements are responsible for the dynamic dipolar coupling detailed in section IV B.

$$h_{j,j'} = 4\pi \left\{N_{xx}^{(j,j')}\right\} M_{j'} \tag{50}$$

The value of the coupling frequency Ω for the lowest energy mode yields:

$$\Omega \simeq \gamma \sqrt{\left\{N_{xx}^{(a,b)}\right\} 4\pi M_b \left\{N_{xx}^{(b,a)}\right\} 4\pi M_a} \, , \tag{51}$$

which leads to $\Omega/2\pi \simeq 0.56$ GHz.

TABLE III. Values of the self- and cross- depolarization tensor elements weighted by the precession profile of the uniform mode for the thin ($j = a$) and thick ($j = b$) disks.

	(a,a)	(a,b)	(b,a)	(b,b)
$\{N_{zz}^{(j,j')}\}$	+0.979	−0.068	−0.017	+0.919
$\{N_{xx}^{(j,j')}\}$	+0.016	+0.042	+0.011	+0.056

Neglecting the dynamical dipolar coupling (the generalization to $\Omega \neq 0$ is Eq. (15)), we derive an expression for the eigen-value of index $\nu = j_{0,0}$:

$$\frac{\omega_\nu}{\gamma} = \{H\} + 4\pi \left\{ N_{xx}^{(j,j)} \right\} M_j + \{H_{\rm ex}\} \ , \tag{52}$$

$j = a, b$ being the layer index and $\{H\}$ being defined in Eq. (46). Eq. (52) is a simplified expression valid for circularly polarized modes ($\ell = 0$ index), where we have taken advantage of the equality $\{N_{xx}\}_0 = \{N_{yy}\}_0$ in our circular disk. This expression can be extended to higher order modes by using $\{N_{xx}\}_{\ell,n} \approx \{N_{xx}\}_0 \sqrt{k_{\ell,n}/k_0}$ inside Eq. (52). This approximation is derived from the ellipticity of $\ell \neq 0$ modes ($\{N_{xx}\} \neq \{N_{yy}\}$). One needs thus two separate equations (52) for the values of ω for each cartesian axis [38]: one proportional to $m_x^2/(m_x m_y)$, the other to $m_y^2/(m_x m_y)$. The product of these two equations is independent of the ellipticity, leading to the general expression for the eigen-value of arbitrary index $\nu = j_{\ell,n}$:

$$\begin{aligned} \frac{\omega_\nu^2}{\gamma^2} = & \left(\{H\}_\nu + 4\pi \left\{ N_{xx}^{(j,j)} \right\}_\nu M_j + \{H_{\rm ex}\}_\nu \right) \times \\ & \left(\{H\}_\nu + 4\pi \left\{ N_{yy}^{(j,j)} \right\}_\nu M_j + \{H_{\rm ex}\}_\nu \right) , \end{aligned} \tag{53}$$

which can be seen as a generalization of the Kittel formula for arbitrary shaped multi-body.

Equating $H_{a00} = H_{③}$ and $H_{b00} = H_{①}$ in Eq. (52), where H_{a00} and H_{b00} are the resonance fields at $f_{\rm fix} = 8.1$ GHz of the uniform modes in the thin and thick disks, respectively, leads to $4\pi M_a = 8.0 \times 10^3$ G and $4\pi M_b = 9.6 \times 10^3$ G.

Finally, the above formalism also enables to determine the angle $\theta_j = (\hat{\boldsymbol{z}}, \hat{\boldsymbol{u}}_j)$ between the equilibrium direction of the magnetization in layer j and the normal axis when the bias field is applied at a polar angle $\theta_H = (\hat{\boldsymbol{z}}, \boldsymbol{H}_{\rm ext})$. From the equality $\hat{\boldsymbol{u}} \times \boldsymbol{H}_{\rm ext} = 4\pi M_j \hat{\boldsymbol{u}} \times \left\langle \widehat{\boldsymbol{G}}^{(d_j)} * \hat{\boldsymbol{u}} \right\rangle$, one extracts the relationship:

$$H_{\rm ext} \sin\left(\theta_j - \theta_H\right) = 2\pi M_j \left(\langle N_{zz}^{(jj)} \rangle - \langle N_{xx}^{(jj)} \rangle \right) \sin 2\theta_j \tag{54}$$

The angle θ_j is useful to estimate the shift to lower field of the FMR spectrum [38], $2\pi M_j(\{N_{zz}^{(j)}\} - \{N_{xx}^{(j)}\})(1 - \cos 2\theta_j) \approx 420$ Oe, when $\theta_b = 13°$ in the thick layer.

VIII. APPENDIX B: METHODS AND CALIBRATION

A. Mechanical vibration amplitude

Here, we detail the experimental protocol used to calibrate the amplitudes of the uniform RF magnetic field and of the mechanical-FMR signal. The procedure uses the non-linear properties of the magnetization dynamics and consists in studying the power dependence of the line shape. In the following, ΔH denotes the FWHM linewidth measured in the linear regime.

We use the onset of foldover as a mean to calibrate the strength of the RF field produced by the microwave antenna. This non-linear effect is responsible for the asymmetric shape of the resonance peaks in FIGS. 2 and 3. In fact, it was pointed out by Anderson and Suhl [51] that the resonance curve at high power should be skewed, due to the static change of the magnetization M_z, which also shifts the resonance frequency. For a normally magnetized sample, this non-linear frequency shift is positive (blue-shift), and the field-sweep line shapes are distorted towards low field. There is a critical strength of the RF magnetic field h_c (linearly polarized amplitude) for which the slope of the resonance curve becomes infinite on the low field side of the resonance [52]:

$$h_c = 2\Delta H \sqrt{\frac{2\Delta H}{3\sqrt{3}\,|\{N_{zz}\} - \{N_{xx}\}|\,4\pi M_s}} \tag{55}$$

where $\{N_{zz}\} - \{N_{xx}\}$ is the difference between the depolarization factors in the longitudinal and transverse directions. Experimentally we find that for the peak at $H_①$, this onset is reached when the output power of the synthesizer at 8.1 GHz is $P_0 = +9$ dBm. Using the magnetic properties of the thick layer (Table I), we infer from Eq. (55) that at the critical onset of foldover, the strength of the RF magnetic field is $h_c = 4.2 \pm 0.8$ Oe. We note, that this value is in agreement with the estimation made by directly evaluating the field produced by the RF current flowing in the antenna at 8.1 GHz for this output power, $h_{\mathrm{rf}} = 5.5 \pm 1$ Oe.

Furthermore, this procedure gives a calibration of the amplitude of the mechanical-FMR signal $\langle \Delta M_z \rangle$. At the onset of foldover, the longitudinal change of the magnetization is

indeed [51]

$$4\pi\langle\Delta M_z\rangle = \frac{4}{3\sqrt{3}}\Delta H. \tag{56}$$

A numerical application of Eq. (56) yields $4\pi\langle\Delta M_z\rangle = 36 \pm 4$ G, which corresponds to the critical angle of precession $\langle\theta_c\rangle = 5°$. We have used this calibration of the cantilever vibration amplitude to evaluate the change of the longitudinal magnetization at the maximum of the peak at $H_①$ in FIG. 2a.

B. Microwave setup

In this appendix, we give some details on the microwave circuit, which was carefully design to minimize the cross-talk between the RF field and RF current excitation parts.

The calibration of the RF magnetic field produced by the microwave antenna has been presented in the previous appendix. In order to calibrate the RF current flowing through the nano-pillar with respect to the synthesizer output power injected into the contact electrodes, we have first used a standard microwave setup. The nano-pillar electrodes are directly connected to the microwave synthesizer through a picoprobe, a bias-T, and a semi-rigid coaxial line, that allow to perform voltage-FMR spectroscopy. In this experiment, the amplitude of $i_{\rm rf}$ flowing through the nano-pillar can be accurately determined, owing to the determination of losses and reflexions in the microwave circuit using a network analyzer. Then, the same experiment is repeated inside the MRFM setup, in which the contact electrodes are wire bounded to a microwave cable and the circuit contains more connections. The comparison with the standard setup yields an estimation of the rms amplitude of the RF current in the mechanical-FMR setup: $i_{\rm rf} = 170 \pm 40$ μA for an output power of -22 dBm injected at 8.1 GHz through the contact electrodes.

It is also possible to estimate experimentally the high frequency coupling between the microwave antenna and the electrodes that contact the nano-pillar. For this, we exploit the fact that in the exact perpendicular configuration, different SW modes are excited by the uniform RF field ($\ell = 0$-index) and by the RF current ($\ell = +1$-index). If the RF magnetic field used to excite the conventional FMR spectrum would induce any relevant RF eddy current through the nano-pillar, $\ell = +1$ modes which are excited in the SW spectrum of FIG. 2b should also be detected in the SW spectrum of FIG. 2a, which is not the case. We deduce from this observation that for an output power of +3 dBm injected in the antenna, the

induced eddy current through the nano-pillar is less than when injecting −38 dBm directly through the contact electrodes, *i.e.*, $i_{\mathrm{rf}} < 30$ μA. So, at $f_{\mathrm{fix}} = 8.1$ GHz, the isolation between the two parts of the microwave circuit is better than 40 dB. However, we note that the latter depends on the frequency, and that for some particular values, it can drop to only 20 dB.

Still, owing to the broadband design of the contact electrodes and to the low microwave power required to excite SW modes with the RF current excitation part, it is possible to acquire FMR spectra at a fixed bias magnetic field H_{fix} by sweeping the frequency of the RF current. We mention that in the frequency-sweep experiments presented in FIG. 4a, the output power of the synthesizer is kept at −22 dBm over the full frequency range (4 to 18 GHz), which results in an amplitude variation of i_{rf}, mainly associated to frequency dependent losses in the circuit. We also note that the same frequency-sweep experiment cannot be performed as cleanly with the RF field excitation due to the high power that has to be injected in the microwave antenna and to the dependence of the isolation on frequency mentioned above.

C. Cavity-FMR characterization of the extended film

Before the nano-fabrication of the nano-pillar devices, a reference film of Cu60 | Py_b15 | Cu10 | Py_a4 | Au25 (thicknesses in nm) is cut out from the Si wafer for characterization purpose. The extraction of the material parameters is obtained independently on this reference film by a reflexion X-band spectrometer (9.6 GHz) operating at room temperature. The experiment consists in measuring the resonance spectra of the multi-layer as a function of the polar angle θ_H between the applied field and the normal to the film. The resonance field of the layer $j = a, b$ as a function of θ_H depends only on the gyromagnetic ratio γ and on the total perpendicular anisotropy field, which here reflects entirely the demagnetizing field $4\pi M_j$ of the layer [94]. The obtained values for the gyromagnetic ratio (identical for both layers) and the magnetizations are collected in Table I. The magnetization of the thick layer (9.6 kOe) corresponds to the expected value for bulk Py with composition $\mathrm{Ni_{80}Fe_{20}}$. The magnetization of the thin layer is 1.4 kG smaller, which reflects the reduction of the magnetization in the interfacial layer (of the order of 1 nm), due to the gradual composition variation of the NiFe alloy from $\mathrm{Ni_{80}Fe_{20}}$ to the normal metal (Cu or Au) [58, 60].

An estimate of the damping parameter and the amount of inhomogeneous broadening

can also be obtained from the angular dependence of the linewidth of the resonant mode associated to each layer. The linewidth is in general the sum of two contributions: an intrinsic relaxation of the magnetization vector (homogeneous width) and an inhomogeneous broadening corresponding to a distribution of resonance fields (whose main sources have been described for a Permalloy polycrystalline layer [94]). The intrinsic damping parameter is deduced from the parallel geometry linewidth. In the Py_b 15 nm thick layer, the linewidths observed in the parallel and perpendicular geometries are respectively: $\Delta H_{\parallel b}$ = 64 Oe and $\Delta H_{\perp b}$ = 73 Oe. The higher value observed in the perpendicular geometry reveals a fair amount of inhomogeneities [94]. The linewidth observed in the parallel geometry corresponds to an intrinsic damping parameter $\alpha_b = (0.9 \pm 0.1) \times 10^{-2}$. For the thin Py_a 4 nm layer, $\Delta H_{\parallel a}$ = 83 Oe and $\Delta H_{\perp a}$ = 171 Oe. From the parallel geometry linewidth, we deduce an intrinsic damping parameter $\alpha_a = (1.5 \pm 0.3) \times 10^{-2}$. This value is higher than for the thick layer because of the larger effect of the diffusion of the microwave magnetization of the conduction electrons in the adjacent normal metal layers [60], associated to the fact that the thin layer thickness (4 nm) is less than the spin-diffusion length in Py. The much larger value $\Delta H_{\perp a}$ is associated to a large contribution of the inhomogeneous broadening arising from a substantial effect of interfacial roughness (and dispersion of heights of the crystallites of the base) on the thin Py layer grown on top of a 85 nm thick metallic base.

---

[1] S. Wolf, D. D. Awschalom, R. A. Buhrman, J. Daughton, S. von Molnar, M. L. Roukes, A. Y. Chtchelkanova, and D. M. Treger, Science **294**, 1488 (2001)

[2] M. N. Baibich, J. M. Broto, A. Fert, F. N. V. Dau, F. Petroff, P. Etienne, G. Creuzet, A. Friederich, and J. Chazelas, Phys. Rev. Lett **61**, 2472 (1988)

[3] G. Binasch, P. Grunberg, F. Saurenbach, and W. Zinn, Phys. Rev. B **39**, 4828 (1989)

[4] B. Dieny, V. Speriosu, B. Gurney, S. Parkin, D. Wilhoit, K. Roche, S. Metin, D. Peterson, and S. Nadimi, J. Magn. Magn. Mater. **93**, 101 (1991)

[5] M. Pannetier, C. Fermon, G. L. Goff, J. Simola, and E. Kerr, Science **304**, 1648 (2004)

[6] J. Slonczewski, J. Magn. Magn. Mater. **159**, L1 (1996)

[7] L. Berger, Phys. Rev. B **54**, 9353 (1996)

[8] M. Tsoi, A. G. M. Jansen, J. Bass, W.-C. Chiang, M. Seck, V. Tsoi, and P. Wyder, Phys.

Rev. Lett. **80**, 4281 (1998)

[9] F. J. Albert, J. A. Katine, R. A. Buhrman, and D. C. Ralph, Appl. Phys. Lett. **77**, 3809 (2000)

[10] J. Grollier, V. Cros, A. Hamzic, J. M. George, H. Jaffres, A. Fert, G. Faini, J. Ben Youssef, and H. Legall, Appl. Phys. Lett. **78**, 3663 (2001)

[11] S. I. Kiselev, J. C. Sankey, I. N. Krivorotov, N. C. Emley, R. J. Schoelkopf, R. A. Buhrman, and D. C. Ralph, Nature **425**, 380 (2003)

[12] W. H. Rippard, M. R. Pufall, S. Kaka, S. E. Russek, and T. J. Silva, Phys. Rev. Lett. **92**, 027201 (2004)

[13] V. E. Demidov, S. O. Demokritov, B. Hillebrands, M. Laufenberg, and P. P. Freitas, Appl. Phys. Lett. **85**, 2866 (2004)

[14] G. Woltersdorf, O. Mosendz, B. Heinrich, and C. H. Back, Phys. Rev. Lett. **99**, 246603 (2007)

[15] G. de Loubens, V. V. Naletov, O. Klein, J. Ben Youssef, F. Boust, and N. Vukadinovic, Phys. Rev. Lett. **98**, 127601 (2007)

[16] G. de Loubens, V. V. Naletov, M. Viret, O. Klein, H. Hurdequint, J. Ben Youssef, F. Boust, and N. Vukadinovic, J. Appl. Phys. **101**, 09F514 (2007)

[17] G. Gubbiotti, M. Madami, S. Tacchi, G. Carlotti, H. Tanigawa, and T. Ono, J. Phys. D: Appl. Phys. **41**, 134023 (2008)

[18] P. S. Keatley, V. V. Kruglyak, A. Neudert, E. A. Galaktionov, R. J. Hicken, J. R. Childress, and J. A. Katine, Phys. Rev. B **78**, 214412 (2008)

[19] A. Slavin and V. Tiberkevich, IEEE Trans. Magn. **45**, 1875 (2009)

[20] A. V. Nazarov, H. S. Cho, J. Nowak, S. Stokes, and N. Tabat, Appl. Phys. Lett. **81**, 4559 (2002)

[21] N. Stutzke, S. L. Burkett, and S. E. Russek, Appl. Phys. Lett. **82**, 91 (2003)

[22] S. Petit, C. Baraduc, C. Thirion, U. Ebels, Y. Liu, M. Li, P. Wang, and B. Dieny, Phys. Rev. Lett. **98**, 077203 (2007)

[23] A. Helmer, S. Cornelissen, T. Devolder, J.-V. Kim, W. van Roy, L. Lagae, and C. Chappert, Phys. Rev. B **81**, 094416 (2010)

[24] A. A. Tulapurkar, Y. Suzuki, A. Fukushima, H. Kubota, H. Maehara, K. Tsunekawa, D. D. Djayaprawira, N. Watanabe, and S. Yuasa, Nature **438**, 339 (2005)

[25] J. C. Sankey, P. M. Braganca, A. G. F. Garcia, I. N. Krivorotov, R. A. Buhrman, and D. C.

Ralph, Phys. Rev. Lett. **96**, 227601 (2006)

[26] W. Chen, J.-M. L. Beaujour, G. de Loubens, A. D. Kent, and J. Z. Sun, Appl. Phys. Lett. **92**, 012507 (2008)

[27] W. Chen, G. de Loubens, J.-M. L. Beaujour, A. D. Kent, and J. Z. Sun, J. Appl. Phys. **103**, 07A502 (2008)

[28] N. Biziere, E. Murè, and J.-P. Ansermet, Phys. Rev. B **79**, 012404 (2009)

[29] C. T. Boone, J. A. Katine, J. R. Childress, V. Tiberkevich, A. Slavin, J. Zhu, X. Cheng, and I. N. Krivorotov, Phys. Rev. Lett. **103**, 167601 (2009)

[30] W. H. Rippard, A. M. Deac, M. R. Pufall, J. M. Shaw, M. W. Keller, S. E. Russek, G. E. W. Bauer, and C. Serpico, Phys. Rev. B **81**, 014426 (2010)

[31] N. Biziere and C. Fermon, Appl. Phys. Lett. **92**, 092503 (2008)

[32] N. Biziere and C. Fermon, Phys. Rev. B **78**, 064408 (2008)

[33] D. Houssameddine, U. Ebels, B. Delaët, B. Rodmacq, I. Firastrau, F. Ponthenier, M. Brunet, C. Thirion, J.-P. Michel, L. Prejbeanu-Buda, M.-C. Cyrille, O. Redon, and B. Dieny, Nature Mater. **6**, 447 (2007)

[34] Z. Zhang, P. C. Hammel, and P. E. Wigen, Appl. Phys. Lett. **68**, 2005 (1996)

[35] K. Wago, D. Botkin, C. S. Yannoni, and D. Rugar, Appl. Phys. Lett. **72**, 2757 (1998)

[36] A. Jander, J. Moreland, and P. Kabos, J. Appl. Phys. **89**, 7086 (2001)

[37] V. Charbois, V. V. Naletov, J. Ben Youssef, and O. Klein, J. Appl. Phys. **91**, 7337 (2002)

[38] O. Klein, G. de Loubens, V. V. Naletov, F. Boust, T. Guillet, H. Hurdequint, A. Leksikov, A. N. Slavin, V. S. Tiberkevich, and N. Vukadinovic, Phys. Rev. B **78**, 144410 (2008)

[39] G. de Loubens, V. V. Naletov, and O. Klein, Phys. Rev. B **71**, 180411 (2005)

[40] V. V. Naletov, G. de Loubens, V. Charbois, O. Klein, V. S. Tiberkevich, and A. N. Slavin, Phys. Rev. B **75**, 140405 (2007)

[41] G. de Loubens, A. Riegler, B. Pigeau, F. Lochner, F. Boust, K. Y. Guslienko, H. Hurdequint, L. W. Molenkamp, G. Schmidt, A. N. Slavin, V. S. Tiberkevich, N. Vukadinovic, and O. Klein, Phys. Rev. Lett. **102**, 177602 (2009)

[42] B. Pigeau, G. de Loubens, O. Klein, A. Riegler, F. Lochner, G. Schmidt, L. W. Molenkamp, V. S. Tiberkevich, and A. N. Slavin, Appl. Phys. Lett. **96**, 132506 (2010)

[43] B. Pigeau, G. de Loubens, O. Klein, A. Riegler, F. Lochner, G. Schmidt, and L. W. Molenkamp, Nature Phys. **7**, 26 (2011)

[44] We mention here that the measured amplitude of the GMR effect in our sample is ΔR_{GMR} = 25 mΩ, in agreement with the value calculated by CRMT for the multi-layer stack composition [89].

[45] O. Klein, V. Charbois, V. V. Naletov, and C. Fermon, Phys. Rev. B **67**, 220407(R) (2003)

[46] O. Klein, V. Charbois, V. V. Naletov, and C. Fermon, J. Magn. Magn. Mater. **272**, E1027 (2004)

[47] I. Lee, Y. Obukhov, G. Xiang, A. Hauser, F. Yang, P. Banerjee, D. Pelekhov, and P. Hammel, Nature **466**, 845 (2010)

[48] V. Charbois, V. V. Naletov, J. Ben Youssef, and O. Klein, Appl. Phys. Lett. **80**, 4795 (2002)

[49] V. V. Naletov, V. Charbois, O. Klein, and C. Fermon, Appl. Phys. Lett. **83**, 3132 (2003)

[50] R. E. Arias and D. L. Mills, Phys. Rev. B **79**, 144404 (2009)

[51] P. W. Anderson and H. Suhl, Phys. Rev. **100**, 1788 (1955)

[52] E. Schlömann, *Ferromagnetic resonance at high power levels*, Tech. Rep. (Technical Report No. R-48, 1959) (unpublished)

[53] W. Chen, G. de Loubens, J.-M. L. Beaujour, J. Z. Sun, and A. D. Kent, Appl. Phys. Lett. **95**, 172513 (2009)

[54] Y. Tserkovnyak, A. Brataas, G. E. W. Bauer, and B. I. Halperin, Rev. Mod. Phys. **77**, 1375 (2005)

[55] M. V. Costache, M. Sladkov, S. M. Watts, C. H. van der Wal, and B. J. van Wees, Phys. Rev. Lett. **97**, 216603 (2006)

[56] J. N. Kupferschmidt, S. Adam, and P. W. Brouwer, Phys. Rev. B **74**, 134416 (2006)

[57] As expected, this value corresponds to the stray field of the magnetic sphere with magnetic moment $m = 2 \times 10^{-10}$emu set at a distance $s = 1.3$ μm from the nano-pillar.

[58] S. Mizukami, Y. Ando, and T. Miyazaki, Jpn J. Appl. Phys. **40**, 580 (2001)

[59] J.-M. L. Beaujour, J. H. Lee, A. D. Kent, K. Krycka, and C.-C. Kao, Phys. Rev. B **74**, 214405 (2006)

[60] H. Hurdequint, J. Magn. Magn. Mater. **310**, 2061 (2007)

[61] A. G. Gurevich and G. A. Melkov, *Magnetization Oscillations and Waves* (CRC Press, 1996)

[62] M. Bailleul, R. Hollinger, and C. Fermon, Phys. Rev. B **73**, 104424 (2006)

[63] K. Y. Guslienko, S. O. Demokritov, B. Hillebrands, and A. N. Slavin, Phys. Rev. B **66**, 132402 (2002)

[64] It will lead to an error of the order of $4\pi\gamma M_s(t/R)^2$ in the frequency, which is much smaller than, *e.g.*, the distance between different modes.

[65] J. F. Dillon, J. Appl. Phys. **31**, 1605 (1960)

[66] R. W. Damon and J. R. Eshbach, J. Phys. Chem. Solids **19**, 308 (1961)

[67] C. Kittel, Phys. Rev. **110**, 1295 (1958)

[68] M. Belmeguenai, T. Martin, G. Woltersdorf, M. Maier, and G. Bayreuther, Phys. Rev. B **76**, 104414 (2007)

[69] G. Gubbiotti, M. Kostylev, N. Sergeeva, M. Conti, G. Carlotti, T. Ono, A. N. Slavin, and A. Stashkevich, Phys. Rev. B **70**, 224422 (2004)

[70] J. Ben Youssef and A. Layadi, J. Appl. Phys. **108**, 053913 (2010)

[71] O. Dmytriiev, T. Meitzler, E. Bankowski, A. Slavin, and V. Tiberkevich, J. Phys.: Condens. Matter **22**, 136001 (2010)

[72] `http://www.insilicio.fr/pdf/Spinflow_3D.pdf`

[73] W. E and X.-P. Wang, SIAM J. Numer. Anal. **38**, 1647 (2001)

[74] M. d'Aquino, C. Serpico, G. Miano, and C. Forestiere, J. Comput. Phys. **228**, 6130 (2009)

[75] R. Lehoucq, D. Sorensen, and C. Yang, *ARPACK Users' Guide: Solution of Large-Scale Eigenvalue Problems with Implicitly Restarted Arnoldi Methods* (SIAM Publications, Philadelphia, 1998)

[76] R. D. McMichael and M. D. Stiles, J . Appl. Phys. **97**, 10J901 (2005)

[77] The two images of FIGS. 11b and 11c are top and bottom view of the nano-pillar, hence one of them should be mirrored for direct comparison of the relative phase between the layers.

[78] M. P. Kostylev, A. A. Stashkevich, N. A. Sergeeva, and Y. Roussigné, J. Magn. Magn. Mater. **278**, 397 (2004)

[79] B. Pigeau et al., in preparation.

[80] S. Kaka, M. R. Pufall, W. H. Rippard, T. J. Silva, S. E. Russek, and J. A. Katine, Nature **437**, 389 (2005)

[81] F. B. Mancoff, N. D. Rizzo, B. N. Engel, and S. Tehrani, Nature **437**, 393 (2005)

[82] A. N. Slavin and V. S. Tiberkevich, Phys. Rev. B **72**, 092407 (2005)

[83] J. Grollier, V. Cros, and A. Fert, Phys. Rev. B **73**, 060409 (2006)

[84] B. Georges, J. Grollier, M. Darques, V. Cros, C. Deranlot, B. Marcilhac, G. Faini, and A. Fert, Phys. Rev. Lett. **101**, 017201 (2008)

[85] A. Ruotolo, V. Cros, B. Georges, A. Dussaux, J. Grollier, C. Deranlot, R. Guillemet, K. Bouzehouane, S. Fusil, and A. Fert, Nature Nanotech. **4**, 528 (2009)

[86] S. Urazhdin, P. Tabor, V. Tiberkevich, and A. Slavin, Phys. Rev. Lett. **105**, 104101 (2010)

[87] A. Dussaux, A. V. Khvalkovskiy, J. Grollier, V. Cros, A. Fukushima, M. Konoto, H. Kubota, K. Yakushiji, S. Yuasa, K. Ando, and A. Fert, Appl. Phys. Lett. **98**, 132506 (2011)

[88] A. Hamadeh et al., in preparation.

[89] V. S. Rychkov, S. Borlenghi, H. Jaffres, A. Fert, and X. Waintal, Phys. Rev. Lett. **103**, 066602 (2009)

[90] M. Beleggia and M. D. Graef, J. Magn. Magn. Mater. **263**, L1 (2003)

[91] S. Tandon, M. Beleggia, Y. Zhu, and M. De Graef, J. Magn. Magn. Mater. **271**, 9 (2004)

[92] M. Beleggia, S. Tandon, Y. Zhu, and M. D. Graef, J. Magn. Magn. Mater. **278**, 270 (2004)

[93] B. A. Kalinikos and A. N. Slavin, J. Phys. C **19**, 7013 (1986)

[94] H. Hurdequint, J. Magn. Magn. Mater. **242-245**, 521 (2002)

Chapter 2.

Noise properties of a resonance-type spin-torque microwave detector

We analyze performance of a resonance-type spin-torque microwave detector (STMD) in the presence of noise and reveal two distinct regimes of STMD operation. In the high-frequency regime the minimum detectable microwave power $P_{\min}$ is limited by the low-frequency Johnson-Nyquist noise and the signal-to-noise ratio (SNR) of STMD is proportional to the input microwave power $P_{\rm RF}$. In the low-frequency regime $P_{\min}$ is limited by the magnetic noise, and the SNR is proportional to $\sqrt{P_{\rm RF}}$. The developed formalism can be used for the optimization of the practical noise-handling parameters of a STMD.

I. INTORDUCTION

It has been shown in [1, 2] that a magnetic tunnel junction (MTJ) subjected to the external microwave current $I_{\rm RF}(t) = I_{\rm RF}\cos(2\pi f t)$ can perform as a resonance-type quadratic detector of microwave radiation generating the DC voltage $U_{\rm DC}$ proportional to the acting microwave power $U_{\rm DC} = \varepsilon P_{\rm RF}$ ($P_{\rm RF} \sim I_{\rm RF}^2$). The detector operation is based on the spin-torque effect [3, 4] and the detector sensitivity ε has a maximum value $\varepsilon = \varepsilon_{\rm res}$ when the frequency of the external microwave signal is close to the eigen-frequency f_0 of the MTJ nanopillar, $f = f_0$.

The resonance sensitivity $\varepsilon_{\rm res}$ of the spin-torque microwave detector (STMD) was calculated in [5]:

$$\varepsilon_{\rm res} = \frac{U_{\rm DC}}{P_{\rm RF}} = \left(\frac{\gamma\hbar}{4e}\right)\frac{P^3}{M_s V \Gamma} Q(\theta_0)\ , \tag{57}$$

where $\gamma \approx 2\pi \cdot 28\,\mathrm{GHz/T}$ is the modulus of the gyromagnetic ratio, $\hbar$ is the reduced Planck constant, e is the modulus of the electron charge, P is the spin-polarization efficiency of the MTJ, M_s is the saturation magnetization of the free layer (FL) of MTJ, $V = \pi r^2 d$ is the volume of the FL (r is its radius and d is its thickness), Γ is the magnetization damping rate in the MTJ FL proportional to the Gilbert damping constant α, and $Q(\theta_0)$ is the geometrical factor that depends on the angle θ_0 between the directions of the equilibrium magnetization in FL and pinned layer (PL) of the MTJ. For an in-plane magnetized MTJ, $Q(\theta_0) = \sin^2\theta_0/(1 + P^2\cos\theta_0)^2$.

Estimations based on Eq. (57) [5] and recent experimental results [2, 6] have demonstrated that the STMD sensitivity can exceed that of passive semiconductor Schottky-diode microwave detectors ($\varepsilon \sim 1000\,\mathrm{V/W}$), which makes STMD very interesting for practical applications in microwave measurement technology.

The operation and the minimum detectable power of all types of microwave detectors are limited by noise (in particular, by the low-frequency Johnson-Nyquist (JN) noise in the case of unbiased Schottky diodes [7]), and, therefore, it is important to understand the noise-handling properties of the STMD based on MTJ.

II. INITIAL EQUATIONS

In this chapter we present theoretical analysis of the noise properties of a passive STMD (no DC bias current) using the STMD model developed in [5] with additional terms describing influence of thermal fluctuations. In our analysis we took into account three sources of noise:

(a) Low-frequency Johnson-Nyquist (JN) noise voltage $U_{\mathrm{N}}(t)$ associated with the MTJ resistance R_0. This type of noise is additive and is independent of the magnetization dynamics.

(b) High-frequency JN noise current $I_{\mathrm{N}}(t)$ which transforms into a non-additive low-frequency noise after mixing with the microwave oscillations caused by the input microwave signal.

(c) Magnetic noise (MN), which is caused by the thermal fluctuations of the magnetization direction in the MTJ FL. This noise, modeled by a random magnetic field $\boldsymbol{B}_{\mathrm{N}}(t)$, leads to the fluctuations of the electrical resistance of the STMD and transforms to low frequencies after mixing with the driving current $I_{\mathrm{RF}}(t)$.

The other noise sources, such as shot noise and flicker noise, might be important for STMDs biased by a DC current.

The dynamics of magnetization $\boldsymbol{M}$ in the MTJ FL under the action of a microwave current containing both deterministic and noise components $I(t) = I_{\mathrm{RF}}(t) + I_{\mathrm{N}}(t)$ and noise

magnetic field $\boldsymbol{B}_{\rm N}(t)$ is described by the Landau-Lifshits-Gilbert-Slonczewski equation:

$$\frac{d\boldsymbol{M}}{dt} = \gamma[\boldsymbol{B}_{\rm eff}(\boldsymbol{M}) \times \boldsymbol{M}] + \frac{\alpha}{M_s}\left[\boldsymbol{M} \times \frac{d\boldsymbol{M}}{dt}\right] + \frac{\sigma I(t)}{M_s}[\boldsymbol{M} \times [\boldsymbol{M} \times \boldsymbol{p}]] + \gamma[\boldsymbol{B}_{\rm N}(t) \times \boldsymbol{M}] \ , \tag{58}$$

where $\boldsymbol{B}_{\rm eff}(\boldsymbol{M})$ is the effective magnetic field, which includes the external bias magnetic field $\boldsymbol{B}_0$ and the demagnetization field, $\boldsymbol{p}$ is the unit vector in the direction of the magnetization of the MTJ PL, $\sigma = (\gamma\hbar/2e)P/[(1 + P^2\cos\theta)M_sV]$ is the current-torque proportionality coefficient, and θ is the angle between vectors $\boldsymbol{M}$ and $\boldsymbol{p}$.

We performed analysis for a "planar" STMD, in which both FL and PL are magnetized in-plane. In this case, the MTJ eigen-frequency is $f_0 = (\gamma/2\pi)\sqrt{B_0(B_0 + \mu_0 M_s)}$ and the damping rate has the form $\Gamma = \alpha\gamma(B_0 + \mu_0 M_s/2)$, where μ_0 is the vacuum susceptibility. We assumed that $f = f_0 \gg \Gamma/(2\pi)$. Using Eq. (58), we found the linear FL magnetization response to current $I(t)$ and field $B_{\rm N}(t)$ in the frequency domain. The output STMD signal was calculated as the low-frequency part of the voltage $[R(\theta)I(t) + U_{\rm N}(t)]$, where $R(\theta) = R_\perp/(1 + P^2\cos\theta)$ is the MTJ magnetoresistance, $R_\perp = {\rm RA}/(\pi r^2)$ is the MTJ resistance in the perpendicular magnetic state ($\theta = \pi/2$), and RA is the resistance-area product of the MTJ. We assumed that all noise sources are independent Gaussian processes with uniform spectral densities $S(U_{\rm N}) = S(I_{\rm N})R_0^2 = 2k_BTR_0$ and $S(B_{\rm N}) = 2\alpha k_BT/(\gamma M_sV)$, where k_B is the Boltzmann constant, T is the noise temperature, and $R_0 = R(\theta_0)$ is the equilibrium resistance of MTJ. The detailed derivation of the noise spectrum of STMD will be presented elsewhere [8].

III. RESULTS AND DISCUSSION

We found that the noise of the output voltage $U_{\rm DC} = \varepsilon_{\rm res}P_{\rm RF}$ has characteristic spectral width of Γ and, for typical frequency bandwidth of measurement $\Delta f \ll \Gamma/(2\pi)$, can be considered as frequency-independent. The root mean square fluctuations $\Delta U_{\rm DC}$ can be written in the simple form

$$\Delta U_{\rm DC} = U_{\rm JN}\sqrt{1 + \frac{U_{\rm DC}}{U_{\rm IM}} + \frac{U_{\rm DC}}{U_{\rm MN}}} \ , \tag{59}$$

where the three terms in the right-hand side part of the equation describe, respectively, the influence of the three above mentioned noise sources and

$$U_{\rm JN} = \sqrt{4k_B T R_0 \Delta f}\ , \tag{60a}$$

$$U_{\rm IM} = \frac{R_0}{4\varepsilon_{\rm res}}\ ,\ U_{\rm MN} = \frac{\gamma\hbar}{2e}\frac{B_0}{P}\ . \tag{60b}$$

Note, that both the high-frequency JN and magnetic noise give *non-additive* contributions to the output low-frequency signal and, therefore, their influence increases with the input power (or the output voltage $U_{\rm DC}$). $U_{\rm IM}$ and $U_{\rm MN}$ are the characteristic output voltages, at which the influence of the corresponding noise source becomes comparable to the influence of the additive low-frequency JN noise. Non-additive noises can be ignored for small output signals $U_{\rm DC} \ll U_{\rm IM}, U_{\rm MN}$.

For typical parameters (see e.g. [5, 9]) of an MTJ nanopillar ($r = 50\,\text{nm}$, $d = 1\,\text{nm}$, $P = 0.7$, $\theta_0 = 45$ deg, $R_0 = 500\,\Omega$ (giving RA $= 5.29\,\Omega\,\mu\text{m}^2$), $\alpha = 0.01$, $\mu_0 M_s = 0.8\,\text{T}$, $B_0 = 38\,\text{mT}$ (giving $f_0 = 5\,\text{GHz}$)) Eq. (57) gives the resonance STMD sensitivity in the passive regime $\varepsilon_{\rm res} \approx 700\,\text{V/W}$, which is comparable to the sensitivity of Schottky diodes [9]. At room temperature $T = 300$ K and for the measurement bandwidth of $\Delta f = 1$ MHz Eqs. (60) give the following estimations for the noise-induced voltages: $U_{\rm JN} = 2.88\,\mu\text{V}$, $U_{\rm IM} = 175.9\,\text{mV}$, $U_{\rm MN} = 3.14\,\mu\text{V}$.

It is clear that the characteristic voltage $U_{\rm IM}$ of the non-additive high frequency JN noise is much larger than the voltages created by the low frequency JN noise $U_{\rm JN}$, magnetic noise $U_{\rm MN}$, and the typical DC voltage output $U_{\rm DC}$ of the STMD. This means that the influence of the high-frequency JN noise in Eq. (59) can be completely ignored. Note, also, that, in contrast with the other characteristic noise voltages, the voltage $U_{\rm MN}$ caused by the magnetic noise is proportional to the bias magnetic field B_0, and, therefore, increases with the increase of the frequency of the input microwave signal.

Now, introducing the microwave powers $P_{\rm RF} = U_{\rm DC}/\varepsilon_{\rm res}$, $P_{\rm JN} = U_{\rm JN}/\varepsilon_{\rm res}$, $P_{\rm MN} = U_{\rm MN}/\varepsilon_{\rm res}$ and using Eq. (59), we can write a simple expression for the signal-to-noise ratio (SNR) of the STMD in terms of these characteristic powers:

$$\text{SNR} = \frac{U_{\rm DC}}{\Delta U_{\rm DC}} = \frac{P_{\rm RF}}{P_{\rm JN}}\sqrt{\frac{P_{\rm MN}}{P_{\rm MN} + P_{\rm RF}}}\ . \tag{61}$$

The simple analysis of Eq. (61) demonstrates that there are two distinct regimes of operation of the resonance STMD in the presence of thermal noise. We shall classify them by the

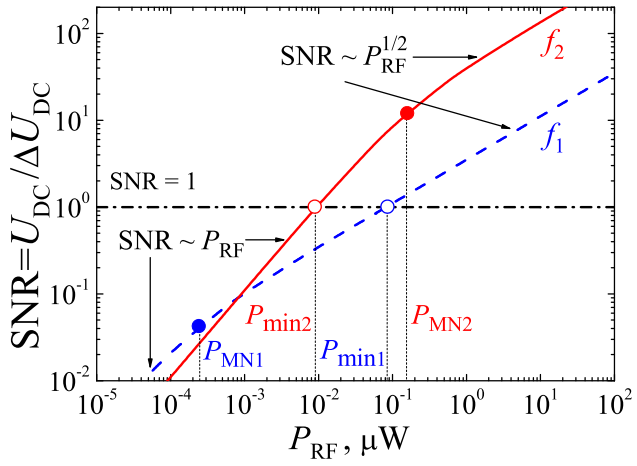

FIG. 14. Dependence of the SNR of STMD on the input microwave power $P_{\rm RF}$ calculated from Eq. (61) for two different frequencies of the input microwave signal: $f_1 = 1\,$GHz (dashed blue line) and $f_2 = 25\,$GHz (solid red line). All other parameters are the same as indicated below Eqs. (60). $P_{\rm min}$ is the minimum detectable power of STMD (at SNR = 1) and $P_{\rm MN}$ is the frequency-dependent characteristic power of magnetic noise.

type of noise that limits the minimum detectable power of STMD $P_{\rm min}$ (power corresponding to SNR = 1).

One regime corresponds to the case of relatively high frequencies of the input microwave signal, when $P_{\rm MN} \gg P_{\rm RF}$ (for $P_{\rm RF} \sim P_{\rm min}$). In this regime, similar to the conventional semiconductor diodes, the minimum detectable power is limited by the low-frequency JN noise, $P_{\rm min} = P_{\rm JN}$, and the SNR of STMD is linearly proportional to the input microwave power $P_{\rm RF}$ (SNR $\simeq P_{\rm RF}/P_{\rm JN}$).

The second regime takes place in the opposite limiting case of relatively low input frequencies, when $P_{\rm MN} \ll P_{\rm RF}$. In this case the SNR of STMD increases with $P_{\rm RF}$ much slower than in conventional diodes, and is proportional to the square root of the input microwave power: SNR $\simeq \sqrt{P_{\rm RF}/P_{\rm min}}$. The minimum detectable power $P_{\rm min} = P_{\rm JN}^2/P_{\rm MN}$ in this regime is limited by the magnetic noise in the FL of the MTJ.

We note, that if at a fixed frequency of the input signal the SNR of an STMD is measured in a wide range of input powers, covering both the above described limiting cases, it is possible to find the characteristic power of the magnetic noise $P_{\rm MN}$ with a good accuracy, and, using expression (60b) for $U_{\rm MN}$, to determine with the same accuracy the MTJ spin-polarization efficiency P.

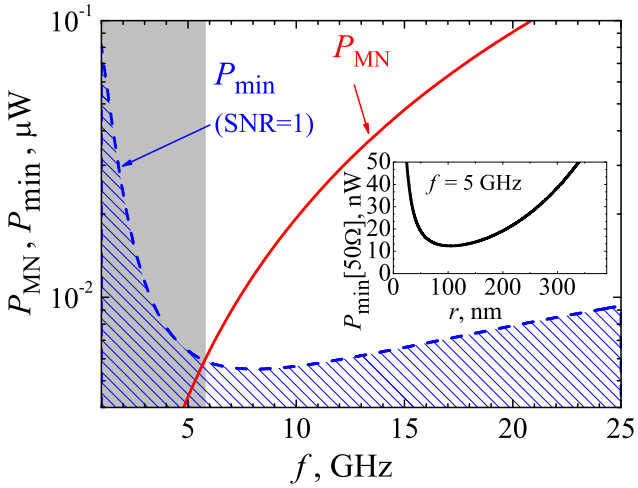

FIG. 15. Characteristic power of magnetic noise $P_{\rm MN}$ (solid red line) and minimum detectable power $P_{\rm min}$ of STMD (dashed blue line) as functions of the input microwave frequency f. The blue dashed area corresponds to undetectable signals $P_{\rm RF} < P_{\rm min}$ and gray shaded area shows the low-frequency STMD regime, where the magnetic noise is dominant in the whole practical region $P_{\rm RF} > P_{\rm min}$. Inset: minimum detectible microwave power delivered to a 50-Ω transmission line $P_{\rm min}[50\,\Omega]$ for $f = 5$ GHz as a function of the radius r of the MTJ nanopillar. STMD parameters are indicated below Eqs. (60).

The existence of two distinct regimes of STMD operation is illustrated in Fig. 14, where two curves calculated from Eq. (61) show the STMD SNR as functions of the input power for signal frequencies $f_1 = 1$ GHz (dashed blue line) and $f_2 = 25$ GHz (red solid curve). It can be seen, that both curves (presented in logarithmic coordinates) demonstrate the clear change of slope from 1 to 1/2 in the region, where the input power $P_{\rm RF}$ is close to the characteristic power of the magnetic noise $P_{\rm MN}$ (which increases with the increase of the input signal frequency). The minimum detectable power $P_{\rm min}$(corresponding to SNR = 1) in the high-frequency case is smaller than $P_{\rm MN}$ and lies in the region of the linear dependence of SNR on $P_{\rm RF}$ (solid red line in Fig. 14). The situation is opposite in the low frequency case (blue dashed curve in Fig. 14), when $P_{\rm min} > P_{\rm MN}$ and lies in the region, where the slope of the SNR curve is equal to 1/2.

The evolution of the characteristic powers $P_{\rm MN}$ and $P_{\rm min}$ with the increase of frequency of the input microwave signal is shown in Fig. 15. The curve $P_{\rm MN}(f)$ separates the plane into the region, where magnetic noise is dominant (above the curve), and the region, where the

STMD operation is limited by the JN noise (below the curve). It is, clear, that the smallest detectable power is achieved near the border of these two regimes.

When an STMD based on an MTJ nanopillar is used as a sensor of microwave radiation, it is typically connected to a standard transmission line with the impedance of $Z_{\rm TL} = 50\,\Omega$. The minimum detectable microwave power *delivered to a 50-Ω transmission line* can be written as [10] $P_{\rm min}[50\,\Omega] = (1/4)(R_0 + Z_{\rm TL})^2 P_{\rm min}/Z_{\rm TL}R_0$. Using this expression and taking into account the size dependence of the STMD resistance ($R_0 \propto 1/r^2$), it is possible to show that $P_{\rm min}[50\,\Omega]$ has a clear minimum as a function of the nanopillar radius r. For instance, the optimum value of the nanopillar radius is $r_{\rm opt} \approx 100\,{\rm nm}$ for the input frequency $f = 5\,{\rm GHz}$ (see the inset in Fig. 15).

IV. CONCLUSIONS

In conclusion, we have demonstrated that STMD in the presence of noise can operate in two distinct regimes, one of which is limited by magnetic noise and is different from the regime of operation of traditional semiconductor detectors. We have, also, suggested that the measurements of STMD SNR in a wide range of input powers can be used to determine the spin-polarization efficiency P of MTJ nanopillars, and have shown that the developed formalism can be used for the optimization of noise-handling parameters of a STMD.

---

[1] A.A. Tulapurkar, Y. Suzuki, A. Fukushima, H. Kubota, H. Maehara, K. Tsunekawa, D.D. Djayaprawira, N. Watanabe, and S. Yuasa, Nature (London) **438**, 339 (2005).

[2] S. Ishibashi, T. Seki, T. Nozaki, H. Kubota, S. Yakata, A. Fukushima, S. Yuasa, H. Maehara, K. Tsunekawa, D.D. Djayaprawira, and Y. Suzuki, Abstracts of the IEEE 7th International Symposium on Metallic Multilayers (MML 2010), I-40, Berkeley, California, September 2010.

[3] J.C. Slonczewski, J. Magn. Magn. Mat. **159**, L1 (1996).

[4] L. Berger, Phys. Rev. B **54**, 9353 (1996).

[5] C. Wang, Y.-T. Cui, J.Z. Sun, J.A. Katine, R.A. Buhrman, and D.C. Ralph, J. Appl. Phys. **106**, 053905 (2009).

[6] X. Cheng, C.T. Boone, J. Zhu, and I.N. Krivorotov, Phys. Rev. Lett. **105**, 047202 (2010).

[7] N.B. Lukyanchikova, *Noise research in semiconductor physics* (CRC Press, Amsterdam, 1996).

[8] O. Prokopenko, V. Tiberkevich, and A. Slavin, in preparation.

[9] S. Ishibashi, T. Seki, T. Nozaki, H. Kubota, S. Yakata, A. Fukushima, S. Yuasa, H. Maehara, K. Tsunekawa, D.D. Djayaprawira, and Y. Suzuki, Appl. Phys. Express **3**, 073001 (2010).

[10] D.M. Pozar, *Microwave Engineering*, 3rd ed. (Wiley, New York, 2005).

Chapter 3.
Spin-torque microwave detector with out-of-plane precessing magnetic moment

Operation of a spin-torque microwave detector (STMD) in a weak perpendicular bias magnetic field has been studied theoretically. It is shown that in this geometry a novel dynamical regime of STMD operation, characterized by large-angle out-of-plane magnetization precession, can be realized. The excitation of the large-angle precession has threshold character and is possible only for input microwave currents exceeding a certain frequency-dependent critical value. The output voltage of an STMD increases with the frequency of the input signal, but is virtually independent of its power. An STMD operating in the out-of-plane regime can be used as a non-resonant threshold detector of low frequency microwave signals and for applications in microwave energy harvesting.

I. INTRODUCTION

The spin-transfer torque (STT) carried by a spin-polarized electric current [1, 2] can give rise to several types of magnetization dynamics (magnetization auto-oscillations and reversal) and, therefore, allows one to manipulate magnetization of a nano-scale magnetic object [3–7]. One of possible applications of the STT is the spin-torque microwave detector (STMD) based on the so-called spin-torque diode effect [8–11]. In an STMD, a microwave current $I_{\rm RF}(t) = I_{\rm RF}\sin(\omega t)$ is supplied to a magnetic tunnel junction (MTJ) structure and excites magnetization precession in the "free" magnetic layer (FL). The resistance oscillations $R(t)$ resulting from this precession mix with the driving current $I_{\rm RF}(t)$ to produce the output DC voltage $U_{\rm DC} = \langle I_{\rm RF}(t)R(t)\rangle$ (here $\langle\ldots\rangle$ denotes averaging over the period of oscillations $2\pi/\omega$ of the external microwave signal).

In the traditional regime of operation of an STMD [8–10] STT excites a *small-angle in-plane* (IP) magnetization precession about the equilibrium direction of magnetization in the FL of an MTJ (see the red dashed curve in Fig. 16). Below we shall refer to this regime of STMD operation as the IP-regime.

In contrast to the well-known IP-regime of STMD operation, in this chapter we consider a *different regime of operation* of an STMD, based on the excitation of *large-angle out-of-plane*

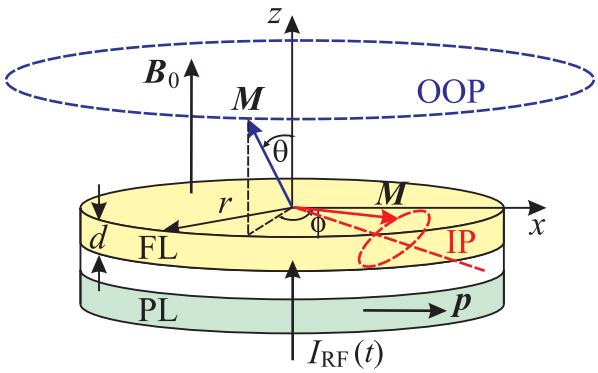

FIG. 16. Model of the considered system: circular nano-pillar of radius r consists of the "free" magnetic layer (FL) of thickness d and the "pinned" magnetic layer (PL). Under the action of microwave current $I_{\rm RF}(t) = I_{\rm RF}\sin(\omega t)$ magnetization vector $\boldsymbol{M}$ (shown by a blue arrow) is precessing along *large-angle out-of-plane* (OOP) trajectory (shown by blue dashed curve) about the direction of the bias magnetic field $\boldsymbol{B}_0 = \hat{\boldsymbol{z}}B_0$ ($B_0 < \mu_0 M_s$), μ_0 is the vacuum permeability, M_s is the saturation magnetization of the FL, $\boldsymbol{p} = \hat{\boldsymbol{x}}$ is the unit vector in the direction of the magnetization of the PL, $\hat{\boldsymbol{x}}$ and $\hat{\boldsymbol{z}}$ are the unit vectors of x- and z-axis, respectively. The red dashed curve is the trajectory of small-angle in-plane (IP) magnetization precession about equilibrium direction of magnetization in the FL (shown by a red dashed line), which exists in the traditional IP-regime of STMD operation.

(OOP) magnetization precession under the action of an input microwave current $I_{\rm RF}(t)$ (see the blue dashed curve in Fig. 16). Using analytical and numerical calculations, we show that all the major STMD characteristics in the OOP-regime qualitatively differ from the ones in the traditional IP-regime. In particular, excitations in the OOP-regime do not have a resonance character and exist in a wide range of driving frequencies. Also, the output DC voltage of an STMD in the OOP regime is almost independent of the input microwave power, provided it exceeds a certain threshold value. We believe that these properties of an STMD in the OOP-regime will be useful for the development of nano-sized threshold detectors with a large output DC voltage and also for the applications in microwave energy harvesting in the low-frequency region of the microwave band.

II. THEORY

A. Model

We consider a simple model of an STMD, formed by a circular MTJ nano-pillar (see Fig. 16). The magnetization of the pinned layer (PL) of the MTJ is assumed to be completely fixed and lie in the plane of the layer. The direction of the PL magnetization $\boldsymbol{p} = \hat{\boldsymbol{x}}$ determines the spin-polarization axis. The radius r of the MTJ nano-pillar is assumed to be sufficiently small, so that the magnetization of the free layer (FL) $\boldsymbol{M} \equiv \boldsymbol{M}(t)$ is spatially-uniform and can be treated in the macrospin approximation.

In contrast with the traditional IP-regime we assume that the STMD is biased by the *perpendicular* magnetic field $\boldsymbol{B}_0 = \hat{\boldsymbol{z}} B_0$, which is *smaller* than the saturation magnetic field of the FL , i.e., $B_0 < \mu_0 M_s$ (μ_0 is the vacuum permeability, $M_s = |\boldsymbol{M}|$ is the saturation magnetization of the FL). For simplicity, we neglect any in-plane anisotropy of the FL.

The dynamics of the unit magnetization vector $\boldsymbol{m}(t) = \boldsymbol{M}(t)/M_s$ in the FL under the action of a microwave current $I_{\rm RF}(t) = I_{\rm RF}\sin(\omega t)$ is governed by the Landau-Lifshits-Gilbert-Slonczewski (LLGS) equation:

$$\frac{d\boldsymbol{m}}{dt} = \gamma\left[\boldsymbol{B}_{\rm eff}\times\boldsymbol{m}\right] + \alpha\left[\boldsymbol{m}\times\frac{d\boldsymbol{m}}{dt}\right] + \sigma I_{\rm RF}(t)\left[\boldsymbol{m}\times\left[\boldsymbol{m}\times\boldsymbol{p}\right]\right] \ , \tag{62}$$

where $\gamma \approx 2\pi\cdot 28$ GHz/T is the modulus of the gyromagnetic ratio, $\boldsymbol{B}_{\rm eff} = (B_0 - \mu_0 M_z)\hat{\boldsymbol{z}}$ is the effective magnetic field, M_z is the z-component of vector $\boldsymbol{M}$, α is the Gilbert damping constant, $\sigma = \sigma_\perp/(1+P^2\cos\beta)$ is the current-torque proportionality coefficient, $\sigma_\perp = (\gamma\hbar/2e)P/(M_s V)$, $\hbar$ is the reduced Planck constant, e is the modulus of the electron charge, P is the spin-polarization of current, β is the angle between the directions of magnetization in the FL and the PL ($\cos\beta = \boldsymbol{m}\cdot\boldsymbol{p}$), $V = \pi r^2 d$ is the volume of the FL (r is its radius and d is its thickness), and $\boldsymbol{p} = \hat{\boldsymbol{x}}$ is the unit vector in the direction of magnetization of the PL.

The angular dependence of the MTJ magnetoresitance can be written as

$$R(\beta) = \frac{R_\perp}{1+P^2\cos\beta} \ , \tag{63}$$

where $R_\perp$ is the junction resistance in the perpendicular magnetic state ($\beta = \pi/2$). The output DC voltage of the STMD is equal to

$$U_{\rm DC} = \langle I_{\rm RF}(t) R(\beta(t))\rangle \ , \tag{64}$$

where the angular brackets denote averaging over the period $2\pi/\omega$ of the microwave current.

Equations (62)-(64) will be used below in analytical and numerical calculations of the STMD performance in the OOP-regime.

B. Analytical description of the OOP-regime

Using the spherical coordinate system for the magnetization vector $\boldsymbol{m} = \hat{\boldsymbol{x}}\sin\theta\cos\phi + \hat{\boldsymbol{y}}\sin\theta\sin\phi + \hat{\boldsymbol{z}}\cos\theta$, one can obtain the equations for the polar θ and azimuthal ϕ angles:

$$\frac{d\theta}{dt} = -\alpha\omega_P \sin\theta - \sigma I_{\mathrm{RF}} \sin(\omega t)\cos\theta\cos\phi \ , \tag{65a}$$

$$\frac{d\phi}{dt} = \omega_P + \sigma I_{\mathrm{RF}} \sin(\omega t)\csc\theta\sin\phi \ . \tag{65b}$$

Here $\omega_P \equiv \omega_P(\theta) = \omega_H - \omega_M\cos\theta$ is the frequency of magnetization precession in the OOP-regime, $\omega_H = \gamma B_0$, $\omega_M = \gamma\mu_0 M_s$. For simplicity, we neglected in Eqs. (65) second-order non-conservative terms ($\propto \alpha^2$ and $\propto \alpha I_{\mathrm{RF}}$), which have a negligible effect on the magnetization dynamics.

In the OOP precessional regime, the magnetization precesses around $\hat{\boldsymbol{z}}$ axis along approximately circular orbit, $\theta \approx$ const, $\phi \approx \omega t + \psi$, where ψ is the phase shift between the magnetization precession and the driving current. To analyze the conditions, under which the OOP regime is possible, one can average Eqs. (65) over the period of precession $2\pi/\omega$ and obtain the following equations for the slow variables θ and ψ:

$$\left\langle \frac{d\theta}{dt} \right\rangle = -\alpha\omega_P \sin\theta + v(a)\frac{\sigma_\perp I_{\mathrm{RF}}}{2}\cos\theta\sin\psi \ , \tag{66a}$$

$$\left\langle \frac{d\psi}{dt} \right\rangle = \omega_P - \omega + u(a)\frac{\sigma_\perp I_{\mathrm{RF}}}{2}\frac{1}{\sin\theta}\cos\psi \ . \tag{66b}$$

Here $a = P^2\sin\theta$ and

$$v(a) = -\frac{2}{\sin\psi}\left\langle \frac{\sin(\omega t)\cos\phi}{1 + P^2\sin\theta\cos\phi} \right\rangle \tag{67a}$$

$$= \frac{1}{\sqrt{1-a^2}}\left[1 + \left(\frac{\sqrt{1-a^2}-1}{a}\right)^2\right]$$

$$u(a) = \frac{2}{\cos\psi}\left\langle \frac{\sin(\omega t)\sin\phi}{1 + P^2\sin\theta\cos\phi} \right\rangle \tag{67b}$$

$$= \frac{1}{\sqrt{1-a^2}}\left[1 - \left(\frac{\sqrt{1-a^2}-1}{a}\right)^2\right] \ .$$

Note, that for typical spin-polarization values $P \lesssim 0.7$ both dimensionless functions $u(a)$ and $v(a)$ are very close to 1 for all angles θ.

The OOP regime of magnetization precession corresponds to a stationary solution of Eqs. (66) $\theta = \theta_s = \text{const}$, $\psi = \psi_s = \text{const}$. Solving Eqs. (66) in this case one can find the stationary value of the phase shift ψ_s:

$$\sin\psi_s = 2\frac{\alpha}{v}\frac{\omega_P}{\sigma_\perp I_{\text{RF}}}\tan\theta_s \ , \tag{68a}$$

$$\cos\psi_s = 2\frac{1}{u}\frac{\omega-\omega_P}{\sigma_\perp I_{\text{RF}}}\sin\theta_s \ . \tag{68b}$$

Eliminating ψ_s from the above equations, one obtains characteristic equation for θ_s:

$$(\omega-\omega_P)^2\sin^2\theta_s + \frac{\alpha^2u^2}{v^2}\omega_P^2\tan^2\theta_s = \frac{u^2}{4}\sigma_\perp^2 I_{\text{RF}}^2 \ . \tag{69}$$

This equation for θ_s is a nonlinear equation, which, in a general case, can be only solved numerically.

One can see that Eq. (69) has solutions only for RF currents I_{RF} larger than a certain critical current I_{th}. At the threshold, $\omega_P(\theta_s) \approx \omega$, which allows one to obtain approximate expression for the threshold precession angle

$$\theta_{\text{th}} \approx \frac{\pi}{2} - \frac{\omega_H-\omega}{\omega_M} \tag{70}$$

and determine the threshold microwave current $I_{\text{th}}(\omega)$ needed for the excitation of the OOP precession:

$$I_{\text{th}}(\omega) = 2\frac{\alpha}{v}\frac{\omega_M}{\sigma_\perp}\frac{\omega}{\omega_H-\omega} \ . \tag{71}$$

In the last expression we used the approximation $\sin(\theta_{\text{th}}) \approx 1$, which is valid for moderate magnetic fields and frequencies ω_H, $\omega \ll \omega_M$.

In order to analyze the stability of the magnetization precession in the OOP-regime we consider small deviations $\delta\theta$, $\delta\psi$ of variables θ, ψ near their stationary values θ_s, ψ_s, respectively. Specifically, one can substitute $\theta = \theta_s + \delta\theta$ and $\psi = \psi_s + \delta\psi$ in Eqs. (66), expand the equations in Taylor series and keep in the newly obtained equations only the terms that are linearly dependent on $\delta\theta$, $\delta\psi$. Taking into account that $\langle d\theta_s/dt\rangle = \langle d\psi_s/dt\rangle = 0$, one can obtain that the magnetization precession in the OOP-regime will be stable if the following approximate conditions are fulfilled:

$$0 < \cos\theta_s < \frac{\omega_H}{\omega_M} \ , \tag{72a}$$

$$\omega < \omega_H \ . \tag{72b}$$

The first condition given by Eq. (72a) means that the precession angle θ_s must be sufficiently large, because $\omega_H \ll \omega_M$ (we consider the case of a weak DC magnetic field) and $\cos\theta_s \ll 1$. The condition Eq. (72b) restricts the region of existence of the OOP-regime to sufficiently low driving frequencies, determined by the bias magnetic field B_0.

The output STMD voltage in the OOP-regime can be found using Eqs. (63) and (64) and noting that $\cos(\beta(t)) = \sin\theta_s \cos\phi(t)$:

$$U_{\rm DC} = \langle I_{\rm RF} R(\beta) \sin(\omega t)\rangle = w(a) I_{\rm RF} R_\perp \sin\psi_s \ , \tag{73}$$

where

$$\begin{aligned} w(a) &= \frac{1}{\sin\psi}\left\langle \frac{\sin(\omega t)}{1 + P^2 \sin\theta\cos\phi}\right\rangle \\ &= \frac{1}{\sqrt{1-a^2}}\left(\frac{1-\sqrt{1-a^2}}{a}\right) \ . \end{aligned} \tag{74}$$

Using Eq. (68a) for $\sin\psi_s$ allows one to get the DC voltage as a function of θ_s only:

$$U_{\rm DC} = 2\alpha \frac{w}{v}\frac{\omega_P}{\sigma_\perp} R_\perp \tan\theta_s \ . \tag{75}$$

This equation for $U_{\rm DC}$ can be simplified further by using the approximation $\sin\theta_s \approx 1$, $\cos\theta_s \approx \cos\theta_{\rm th} \approx (\omega_H - \omega)/\omega_M$, valid for not very large driving currents:

$$U_{\rm DC} \approx 2\alpha \frac{w}{v}\frac{\omega_M}{\sigma_\perp} R_\perp \frac{\omega}{\omega_H - \omega} \ . \tag{76}$$

Comparing Eq. (76) with Eq. (71) for threshold current $I_{\rm th}(\omega)$, one can re-write the output DC voltage of the STMD as the function of threshold current $I_{\rm th}(\omega)$:

$$U_{\rm DC} \approx w I_{\rm th}(\omega) R_\perp \ . \tag{77}$$

It follows from Eqs. (76), (77) that the output DC voltage of the STMD practically does not depend on the amplitude of RF current, provided that it is larger than the threshold current $I_{\rm th}$.

III. PERFORMANCE OF A STMD IN OOP-REGIME

A. Typical parameters of a STMD

Below we shall analyze an analytical solution for the STMD in the OOP-regime of operation, compare this solution with the results of numerical calculations and then also compare the performance of the STMD in IP- and OOP-regimes.

We shall consider the case of the STMD with the following typical parameters (see e.g. [9, 10]): radius of the STMD FL $r = 50\,\text{nm}$, thickness of the STMD FL $d = 1\,\text{nm}$, spin-polarization efficiency of current $P = 0.7$, resistance of STMD in perpendicular magnetic state ($\beta = \pi/2$) $R_\perp = \text{RA}/(\pi r^2) = 1\,\text{k}\Omega$ (giving resistance-area product of MTJ $\text{RA} = 7.854\,\Omega\,\mu\text{m}^2$), Gilbert damping constant $\alpha = 0.01$, saturation magnetization of the FL $\mu_0 M_s = 800\,\text{mT}$.

We choose the magnitude of the external out-of-plane DC magnetic field as $B_0 = 200\,\text{mT}$ for the STMD in OOP-regime, which corresponds to the maximum OOP frequency $\omega_H = 2\pi \times 5.6\,\text{GHz}$.

In the IP-regime of operation, the STMD will be characterized by the equilibrium angle $\beta_0 = \pi/2$ between the equilibrium magnetization of the FL and the magnetization of the PL. Hence the equilibrium resistance of the STMD in the IP-regime is $R_0 = R_\perp = 1\,\text{k}\Omega$. We choose the magnitude of the external DC in-plane magnetic field as $B_0 = 14.1\,\text{mT}$ for the STMD in IP-regime, that in accordance with the expression for FMR frequency $f_0 = \omega_0/2\pi = (\gamma/2\pi)\sqrt{B_0(B_0 + \mu_0 M_s)}$ gives $f_0 = 3\,\text{GHz}$. The resonance STMD sensitivity in the passive regime for such parameters is $\varepsilon_{\text{res}} \approx 2700\,\text{V/W}$ (see e.g.[9]), which is greater or comparable to the sensitivity of a typical unbiased Schottky diode [10].

B. Precession angle and threshold current in the OOP-regime

Numerical solutions of Eq. (69) for the OOP precession angle θ_s as a function of the microwave current I_{RF} for several driving frequencies $f = \omega/2\pi$ are shown in Fig. 17. As one can see, the stable OOP-precession mode exists only for trajectories of magnetization motion with sufficiently large precession angles θ_s (see Eq. (72a)). With the increase of the driving current I_{RF} the precession angle θ_s monotonically increases up to the maximum value $\theta = \pi/2$.

Fig. 17 can also be used for the determination of the threshold current $I_{\text{th}}(\omega)$ needed for excitation of the OOP-precession regime. One can see that with the increase of the microwave frequency ω the threshold current $I_{\text{th}}(\omega)$ also increases. Our calculations show that the difference of $I_{\text{th}}(\omega)$ calculated from Eq. (69) and from approximate Eq. (71) is about several percent and, therefore, one can use analytical Eq. (71) for rather accurate estimation of the threshold current.

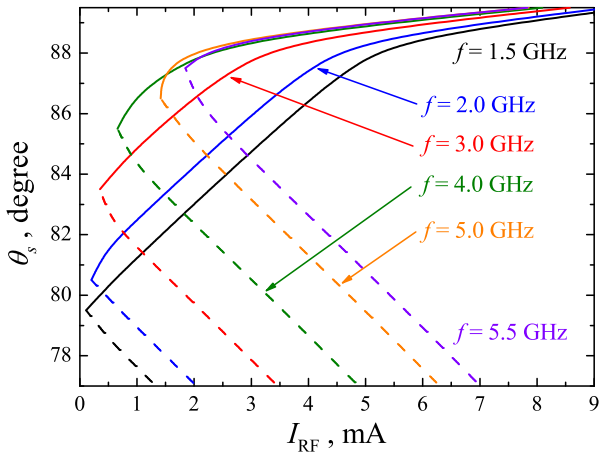

FIG. 17. The dependence of the OOP precession angle θ_s on the magnitude of RF current $I_{\rm RF}$ for different frequencies of RF signal $f = \omega/2\pi$ for an STMD with typical parameters (see Sec. III A). Solid lines correspond to the stable OOP-precession modes, while dashed lines correspond to the unstable trajectories. The minimum value of $I_{\rm RF}$ for any particular curve is the $I_{\rm th}(\omega)$ of the OOP-precession mode.

C. Performance of an STMD in the IP and OOP regimes

The precession motion of magnetization in the IP-regime determines the following typical properties of a traditional STMD [8–10]:

(a) The STMD operates as a frequency-selective microwave detector with a resonance frequency that is close to the frequency of ferromagnetic resonance (FMR) ω_0 of the FL;

(b) The frequency operation range of the detector has an order of the FMR linewidth Γ;

(c) The output DC voltage $U_{\rm DC}$ of the STMD is proportional to the input microwave power $P_{\rm RF} = I_{\rm RF}^2 R_0/2$ (R_0 is the equilibrium MTJ resistance), so the spin-torque diode operates as a resonance-type quadratic microwave detector:

$$U_{\rm DC} = \varepsilon_{\rm res} P_{\rm RF} \frac{\Gamma^2}{\Gamma^2 + (\omega - \omega_0)^2} \,, \tag{78}$$

where $\varepsilon_{\rm res}$ is the resonance (at $\omega = \omega_0$) diode volt-watt sensitivity (see [9]);

(d) the diode resonance sensitivity $\varepsilon_{\rm res}$ strongly depends on the angle β between magnetization directions of the FL and PL. The resonance sensitivity of traditional STMD $\varepsilon_{\rm res} = U_{\rm DC}/P_{\rm RF}$ is predicted to be about $\varepsilon_{\rm res} \sim 10^4\,{\rm V/W}$ (see [9]), while the best achieved to date experimental result is $\varepsilon_{\rm res} \approx 300\,{\rm V/W}$ [10].

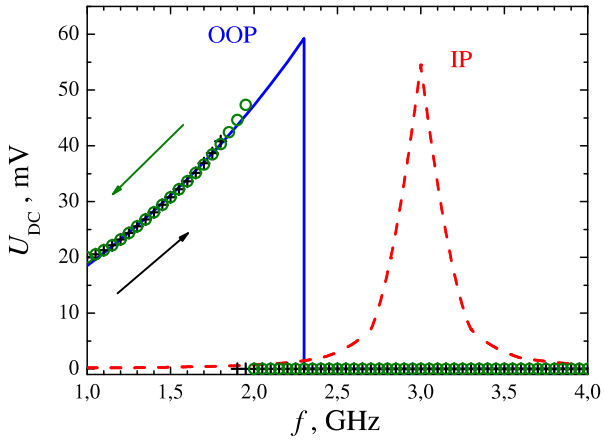

FIG. 18. The dependence of the output DC voltage $U_{\rm DC}$ of a STMD on frequency of input RF signal $f = \omega/2\pi$ in OOP- (solid line and points) and IP-regime (dashed line), respectively. Blue solid line is the analytical dependence given by Eq. (77), red dashed line is the analytical dependence given by Eq. (78). Points are the results of numerical simulations. Black crosses and green circles corresponded to the case when frequency is increased and decreased, respectively. $I_{\rm RF} = 0.2\,{\rm mA}$, all other parameters are the same as indicated in Sec. III A.

We shall use the Eq. (78) for the calculation of the output DC voltage of an STMD in the IP-regime as a function of the input microwave current $I_{\rm RF}$ and current frequency ω. These curves are indicated below in Figs. 19 and 18 by red dashed lines.

In order to verify the conclusions of the analytical theory of an STMD in the OOP-regime we solved numerically the LLGS Eq. (62) and then numerically calculated the output DC voltage of the detector as $U_{\rm DC} = \langle I_{\rm RF}(t) R(\beta) \rangle$. The results of our calculations are presented in Figs. 18, 19. Here solid blue lines and red dashed lines present the analytical dependencies of $U_{\rm DC}$ in the OOP- and IP-regimes (see Eq. (77) and Eq. (78)), respectively. Dots are the results of our numerical calculations. Black crosses and green circles correspond to the cases of increasing and decreasing of the parameter (frequency ω or magnitude $I_{\rm RF}$ of the RF current), respectively. As one can see, the results of analytical theory are in reasonable agreement with the results of our numerical calculations.

As one can see from Fig. 18, in the OOP-regime the STMD works as a broadband low-frequency non-resonant microwave detector in contrast to the traditional resonance IP-regime. The response of the STMD to an input microwave current with magnitude $I_{\rm RF}$ is also substantially different in the cases of OOP- and IP-regimes of operation of an STMD

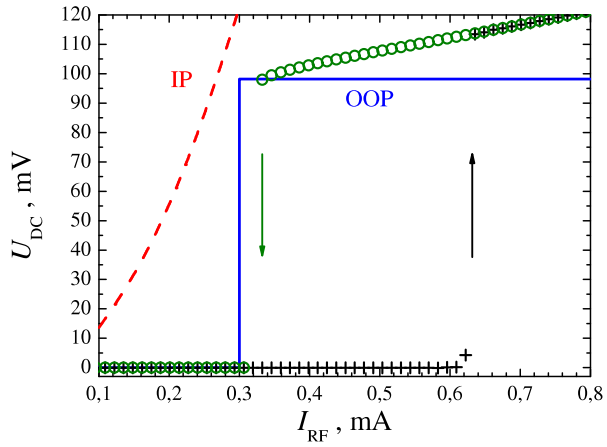

FIG. 19. The dependence of the output DC voltage $U_{\rm DC}$ of a STMD on input microwave current $I_{\rm RF}$ in OOP- (solid line and points) and IP-regime (dashed line), respectively. Blue solid line is the analytical dependence given by Eq. (77), red dashed line is the analytical dependence given by Eq. (78). Points are the results of numerical simulations. Black crosses and green circles corresponded to the case when the current is increased and decreased, respectively. $f = \omega/2\pi = 3\,\text{GHz}$, all other parameters are the same as indicated in Sec. III A.

(see Fig. 19). In the IP-regime, the output DC voltage $U_{\rm DC}$ of the detector is proportional to the input microwave power $P_{\rm RF} = (1/2)I_{\rm RF}^2 R_0$ (red dashed curve in Fig. 19, see also Eq. (78)). In contrast, the output DC voltage $U_{\rm DC}$ of the detector in the OOP-regime has a step-like dependence (blue solid curve and points in Fig. 19): $U_{\rm DC} \approx 0$ for $I_{\rm RF} < I_{\rm th}(\omega)$ and $U_{\rm DC} \approx$ const for $I_{\rm RF} > I_{\rm th}(\omega)$. Thus, in the OOP-regime, the STMD operates as a non-resonant broadband threshold microwave detector of low frequency RF signals.

It is important to note, that the results of our numerical simulations showed the existence of a hysteresis in the curves $U_{\rm DC}(f)$ and $U_{\rm DC}(I_{\rm RF})$ in the OOP-regime (see Figs. 18, 19). The origin of this hysteresis lies in the "hard", or subcritical, scenario of excitation of the OOP precession: the precession angle $\theta_{\rm th}$ that corresponds to the threshold current $I_{\rm th}$ (see Fig. 17) does not coincide with the equilibrium magnetization angle and, therefore, for currents close to the threshold one the OOP regime may or may not be realized, depending on the history of the system. In experiments, the hysteresis may be "blurred" or may not be visible at all due to the influence of thermal fluctuations and other noises existing in real systems.

The results presented above correspond to the case of no DC bias current applied to the MTJ ($I_{\rm DC} = 0$). If this is not the case and $I_{\rm DC} \neq 0$, this current will partly compensate

the damping in the FL MTJ, thus decreasing the threshold current $I_{\rm th}(\omega)$. On the other hand, the in-plane anisotropy and/or the in-plane bias field in the FL may create an energy barrier between the regions of small-angle IP- and large-angle OOP-trajectories, which may result in increase of $I_{\rm RF}$.

We also suggest that the OOP-regime of operation of a STMD might be responsible for an extremely large diode volt-watt sensitivity $\varepsilon \sim 10^5\,{\rm V/W}$ observed in recent experiments with thermally-activated "non-adiabatic stochastic resonance" [11, 12].

D. Energy harvesting applications of an STMD in OOP-regime

The STMD in the OOP-regime could be used as a base element for new energy harvesting devices, inasmuch as it has no resonance frequency, and, therefore, could accumulate energy from all the low-frequency region ($\omega < \omega_H$) of the microwave spectrum.

The energy conversion rate ζ of an STMD in the OOP-regime may be estimated as

$$\zeta = \frac{P_{\rm DC}}{P_{\rm RF}} \approx \frac{1}{2}\left(\frac{I_{\rm th}(\omega)}{I_{\rm RF}}\right)^2 \left(\frac{w}{w_0}\right)^2 , \tag{79}$$

where $P_{\rm DC}$ is the output DC power of an STMD under the action of input microwave power $P_{\rm RF}$, $w_0 \equiv w_0(a_s) = (1-a_s^2)^{-1/2}$, $a_s \approx P^2$. The maximum possible conversion rate $\zeta_{\rm max} \approx 0.5 w^2/w_0^2 \approx 3.5$ % is reached in the case $I_{\rm RF} = I_{\rm th}(\omega)$. We believe that this ratio is sufficiently large for practical applications in microwave energy harvesting.

IV. SUMMARY

In conclusion, it has been demonstrated that there is a novel regime of operation of an STMD, based on the excitation of large-angle out-of-plane (OOP) magnetization precession. In this regime STMD has the following features:

(a) it operates as a *non-resonant* broadband microwave detector for input RF currents $I_{\rm RF}$ larger than the critical current $I_{\rm th}$, $I_{\rm RF} > I_{\rm th}$. Thus, STMD operates as *threshold* detector of RF signals;

(b) a stable OOP-regime exists for low frequency input signals with frequencies $\omega < \omega_H$;

(c) the output DC voltage $U_{\rm DC}$ in the OOP-regime has a step-like form and weakly depends on the magnitude of input RF current $I_{\rm RF}$ for currents $I_{\rm RF} > I_{\rm th}$.

We believe that the OOP regime of STMD operation can be used for the development of novel types of threshold microwave detectors and might be responsible for extremely large diode volt-watt sensitivity observed in recent experiments with "non-adiabatic stochastic resonance" [11, 12]. This regime of operation of an STMD might also be useful for the creation of energy harvesting devices based on STMD, which operate in the low-frequency region of the microwave spectrum.

---

[1] L. Berger, Phys. Rev. B **54**, 9353 (1996).

[2] J.C. Slonczewski, J. Magn. Magn. Mat. **159**, L1 (1996).

[3] G. Bertotti, C. Serpico, I.D. Mayergoyz, R. Bonin, and M. dAquino, Current-induced magnetization dynamics in nanomagnets, J. Magn.Magn. Mater.,**316**, 285 (2007).

[4] D.C. Ralph and M.D. Stiles, J. Magn. Magn. Mater., **320**,1190(2008).

[5] D.V. Berkov and J. Miltat, J. Magn. Magn. Mater.,**320**,1238(2008).

[6] T.J. Silva and W.H. Rippard, J. Magn. Magn. Mater., **320**,1260(2008).

[7] A. Slavin and V. Tiberkevich, IEEE Trans. Magn. **45**, 1875 (2009).

[8] A.A. Tulapurkar, Y. Suzuki, A. Fukushima *et al.*, Nature (London) **438**, 339 (2005).

[9] C. Wang, Y.-T. Cui, J.Z. Sun *et al.*, J. Appl. Phys. **106**, 053905 (2009).

[10] S. Ishibashi, T. Seki, T. Nozaki *et al.*, Appl. Phys. Express **3**, 073001 (2010).

[11] X. Cheng, C.T. Boone, J. Zhu, and I.N. Krivorotov, Phys. Rev. Lett. **105**, 047202 (2010).

[12] X. Cheng, C.T. Boone, J. Zhu, and I.N. Krivorotov, Abstracts of the 55th Annual Conference on Magnetism and Magnetic Materials (MMM 2010), EC-03, Atlanta, Georgia, November 2010.